NASA TECHNICAL NOTE

NASA TN D-7304

NASA TN D-7304

CASE FILE COPY

# DESCRIPTION AND PERFORMANCE OF THE LANGLEY DIFFERENTIAL MANEUVERING SIMULATOR

*by B. R. Ashworth and William M. Kahlbaum, Jr.*

*Langley Research Center*
*Hampton, Va. 23665*

NATIONAL AERONAUTICS AND SPACE ADMINISTRATION • WASHINGTON, D. C. • JUNE 1973

| 1. Report No. | 2. Government Accession No. | 3. Recipient's Catalog No. |
|---|---|---|
| NASA TN D-7304 | | |

| 4. Title and Subtitle | 5. Report Date |
|---|---|
| DESCRIPTION AND PERFORMANCE OF THE LANGLEY DIFFERENTIAL MANEUVERING SIMULATOR | June 1973 |
| | 6. Performing Organization Code |
| 7. Author(s) | 8. Performing Organization Report No. |
| B. R. Ashworth and William M. Kahlbaum, Jr. | L-8827 |
| | 10. Work Unit No. |
| 9. Performing Organization Name and Address | 501-39-11-02 |
| NASA Langley Research Center<br>Hampton, Va. 23665 | 11. Contract or Grant No. |
| | 13. Type of Report and Period Covered |
| 12. Sponsoring Agency Name and Address | Technical Note |
| National Aeronautics and Space Administration<br>Washington, D.C. 20546 | 14. Sponsoring Agency Code |

15. Supplementary Notes

16. Abstract


The Langley differential maneuvering simulator (DMS) provides a realistic means of simulating two aircraft or spacecraft operating in a differential mode. The system consists of two identical fixed-base cockpits and projection systems, each housed in a 12.2-m-diameter (40-ft) spherical projection screen. Each projection system consists of a sky-Earth projector to provide a horizon reference and a system for target-image generation and projection. The projectors and image generators are gimbaled to allow visual simulation with completely unrestricted freedom of motion. The cockpit contains typical instrumentation, a g-suit, a programmable buffet mechanism, and programmable control forces. The system was designed to accommodate simulation of a wide range of aircraft performance.

This report gives a detailed description of the hardware and also describes tests which were performed to verify that the system could provide the required simulated aircraft motions. The mathematical model which converts computed aircraft motions into the required motions of the various projector gimbals is described.


| 17. Key Words (Suggested by Author(s)) | 18. Distribution Statement |
|---|---|
| Simulator performance<br>Visual simulator<br>Servo synchronization<br>Air-combat simulator<br>Docking simulator | Unclassified – Unlimited |

| 19. Security Classif. (of this report) | 20. Security Classif. (of this page) | 21. No. of Pages | 22. Price* |
|---|---|---|---|
| Unclassified | Unclassified | 94 | $3.00 |

*For sale by the National Technical Information Service, Springfield, Virginia 22151

CONTENTS


| | Page |
|---|---|
| SUMMARY | 1 |
| INTRODUCTION | 1 |
| SYMBOLS | 2 |
| SIMULATOR DESCRIPTION | 11 |
| Basic System | 11 |
| External Visual Scene | 12 |
| Sky-Earth projection | 12 |
| Target-image projection | 12 |
| Target-Image Generation | 13 |
| Cockpit Subsystem | 13 |
| Control Console | 15 |
| HARDWARE INTERFACE COMPUTATIONS | 16 |
| PROJECTION GEOMETRY | 17 |
| HARDWARE-SYSTEMS PERFORMANCE | 18 |
| Performance Goals of the Integrated Systems | 18 |
| Servo operating envelope | 19 |
| Servo static performance | 19 |
| Servo dynamic performance | 20 |
| Target-image performance | 20 |
| Performance of the Integrated System | 21 |
| Static accuracy | 21 |
| Dynamic accuracy | 23 |
| Performance assurance | 25 |
| CONCLUDING REMARKS | 26 |
| APPENDIX A – INTERFACE MATH MODEL AND PROJECTION GEOMETRY | 27 |
| Sky-Earth Projector | 27 |
| Sky-Earth gimbals | 27 |
| Sky-Earth lamp drives | 30 |
| Target-Image Projection and Generation | 32 |
| Target-mirror gimbals | 32 |
| Target-model gimbals | 36 |
| Equations for Zoom-Lens Drive | 38 |
| Projection Geometry | 42 |
| Sky-Earth projection geometry | 42 |
| Target-image projection geometry | 45 |

Page

APPENDIX B – COCKPIT ACTIVE INSTRUMENTS . . . . . 47

APPENDIX C – CONTROL-LOADER CHARACTERISTICS . . . . . 50

APPENDIX D – DERIVATION OF THE SERVO TIME LAG . . . . . 51

REFERENCES . . . . . 53

TABLES . . . . . 54

FIGURES . . . . . 61

# DESCRIPTION AND PERFORMANCE OF THE LANGLEY DIFFERENTIAL MANEUVERING SIMULATOR

By B. R. Ashworth and William M. Kahlbaum, Jr.
Langley Research Center

## SUMMARY

The Langley differential maneuvering simulator (DMS) provides a realistic means of simulating two aircraft or spacecraft operating in a differential mode. The system consists of two identical fixed-base cockpits and projection systems, each housed in a 12.2-m-diameter (40-ft) spherical projection screen. Each projection system consists of a sky-Earth projector to provide a horizon reference and a system for target-image generation and projection. The projectors and image generators are gimbaled to allow visual simulation with completely unrestricted freedom of motion. The cockpit contains typical instrumentation, a g-suit, a programmable buffet mechanism, and programmable control forces. The system was designed to accommodate simulation of a wide range of aircraft performance.

This report gives a detailed description of the hardware and also describes tests which were performed to verify that the system could provide the required simulated aircraft motions. The mathematical model which converts computed aircraft motions into the required motions of the various projector gimbals is described.

## INTRODUCTION

The Langley differential maneuvering simulator (DMS) is comprised of two identical, fixed-base, visual flight simulators located in the flight control research laboratory at Langley Research Center.

The DMS facility has been developed as an adjunct to Langley's other research facilities to allow early evaluation of man-in-the-loop performance of new vehicle concepts. The simulator, which became operational in early 1971, provides a realistic cockpit environment and a wide-angle external visual scene for each of the two pilots. The external sky-Earth scene provides reference in all three rotational degrees of freedom in a manner which allows unrestricted rotations. The sky-Earth scene has no translational motion. The external visual scene also provides continuous rotational and bounded translational reference to a second (target) vehicle in six degrees of freedom. In the normal

(differential) mode, the target-vehicle image presented to each pilot represents the craft being flown by the other pilot in this dual simulator. The cockpit provides essential instruments and displays, and kinesthetic cues in the form of a g-suit pressurization system, aircraft buffet, and variable control forces to each pilot.

Potential research applications include combat maneuvering, collision avoidance, and visual rendezvous techniques. In a nondifferential mode, each of the two devices can be used for studies in handling qualities, spin entry and recovery, and trajectory control of an aircraft or spacecraft. Because the emphasis is on vehicle research, a wide range of performance was sought in the simulator equipment providing the visual scene. This paper describes the equipment, its performance goals, and the computing required to convert simulated aircraft motion to hardware servo commands. It also documents the initial performance achieved and describes the methods used to assure hardware performance during operational use.

## SYMBOLS

Values are given both in the SI Units and in the U.S. Customary Units. The measurements and calculations were made in the U.S. Customary Units.

| | |
|---|---|
| $A$ | amplitude of sinusoidal input to servo, rad or m (ft) |
| $\vec{A}$ | vector which defines projected image point in sky-Earth scene relative to corresponding point on transparency, m (ft) |
| $A_x, A_y, A_z$ | x-, y-, and z-components of vector $\vec{A}$, m (ft) |
| $A_1$ | reference point on sky transparency, m (ft) |
| $A_2$ | reference point on Earth transparency, m (ft) |
| $\vec{a}_e$ | vector which defines position command of center of Earth transparency relative to screen center, m (ft) |
| $\vec{a}_o$ | vector which defines center of sky-Earth projector gimbal relative to screen center, m (ft) |
| $\vec{a}_s$ | vector which defines position command of center of sky transparency relative to screen center, m (ft) |

$a_{sx}, a_{sy}, a_{sz}$ x-, y-, and z-components of vector $\vec{a}_s$ in nonrotating $X_A, Y_A, Z_A$ axis system, m (ft)

$\vec{B}$ vector which defines position of target on the screen relative to observer, m (ft)

$\vec{b}_e$ vector which defines position command of Earth projection lamp relative to Earth-transparency center, m (ft)

$\vec{b}_o$ vector which defines position command of center of support arm for sky-Earth lamps relative to sky-Earth gimbal center, m (ft)

$\vec{b}'_o$ vector which defines position of center of support arm for sky-Earth lamps relative to sky-Earth gimbal center as positioned by lamp servos, m (ft)

$b_{ox}, b_{oy}, b_{oz}$ x-, y-, and z-components of vector $\vec{b}_o$ which constitute displacement commands of the sky-Earth lamp servos relative to center of pitch gimbal, m (ft)

$b'_{ox}, b'_{oy}, b'_{oz}$ x-, y-, and z-components of vector $\vec{b}'_o$ which constitute positions of sky-Earth lamp servos relative to gimbal center as measured by linear potentiometers mounted on the servos, m (ft)

$\vec{b}_s$ vector which defines position command of sky projection lamp relative to sky-transparency center, m (ft)

$b_{sx}, b_{sy}, b_{sz}$ x-, y-, and z-components of vector $\vec{b}_s$ in nonrotating $X_A, Y_A, Z_A$ axis system, m (ft)

$C_{AI}$ transformation matrix relating attacker body-axis system to inertial-axis system, dimensionless

$\vec{D}$ vector which defines position of center of azimuth mirror gimbal relative to projection-screen center, m (ft)

$\vec{E}$ vector which defines position of center of target elevation mirror with respect to center of target azimuth mirror, m (ft)

$f_h$ upper frequency limit on buffet-signal generator, Hz

$f_l$ lower frequency limit on buffet-signal generator, Hz

$f_{p_1}, f_{p_2}, f_{p_3}$ structural mode frequencies of buffet-signal generator, Hz

$\hat{i}, \hat{j}, \hat{k}$ unit vectors along X-, Y-, and Z-axes, respectively, of any coordinate-axis systems referred to, dimensionless

K experimentally determined constant of proportionality, dimensionless

$\vec{L}_C$ vector which defines position of sky-Earth lamp relative to center of lamp support arm, m (ft)

$M_c$ absolute magnification of camera lens, dimensionless

$M_c'$ relative magnification of camera lens, dimensionless

$M_e$ electronic magnification of TV system, dimensionless

$M_p$ absolute magnification of projector lens, dimensionless

$M_x$ coordinate of center of azimuth mirror gimbal with respect to center of projection screen as measured along $X_A$-axis, m (ft)

$M_z$ coordinate of center of azimuth mirror gimbal with respect to center of projection screen as measured along $Z_A$-axis, m (ft)

$M_1, M_2, M_3$ peak gain of the three structural modes of buffet-signal generator, dimensionless

$m_{bl}$ transformation matrix which relates attacker line-of-sight axis system to target body-axis system, dimensionless

$\vec{N}$ vector which defines position of a point on sky or Earth transparency relative to observer, m (ft)

$N_x, N_y, N_z$ x-, y-, and z-components of vector $\vec{N}$, m (ft)

$p_A$ instantaneous roll rate of aircraft body axis, rad/sec

$q_A$ instantaneous pitch rate of aircraft body axis, rad/sec

$R$ transformation matrix which defines inner three gimbal rotations of target-model gimbal system, dimensionless

$R_{BA}$ real-world target line-of-sight range, m (ft)

$R_F$ command signal of focus servo, V

$\vec{R}_L$ vector which defines commanded distance from lens to screen for target-image projection, m (ft)

$R_{Lo}$ nominal magnitude of $\vec{R}_L$, m (ft)

$R_1$ radius of projection screen, m (ft)

$R_2$ radius of sky-Earth transparencies, m (ft)

$r_A$ instantaneous yaw rate of aircraft body axis, rad/sec

$\vec{S}$ vector which defines position of center of sky-Earth gimbal relative to center of projection screen, m (ft)

$S_f$ model scale factor, dimensionless

$S_x$ x-component of vector $\vec{S}$, m (ft)

$S_z$ z-component of vector $\vec{S}$, m (ft)

$T$ steady-state time lag (or velocity constant) of a second-order servo, sec

$T_G$ transformation matrix which relates body-axis system to $X_T, Y_T, Z_T$ axis system in terms of actual gimbal angles $\alpha_G$, $\beta_G$, $\phi_G$, $\theta_G$, dimensionless

$t$ time, sec

$U$ transformation matrix which relates body-axis system to $X_T, Y_T, Z_T$ axis system in terms of commanded gimbal angles $\alpha_E$, $\beta_E$, $\phi_E$, $\theta_E$, dimensionless

$U_y, U_z$ horizontal and vertical offsets of surveyor's transit relative to center of sphere as measured along $-Y_A$ and $-Z_A$ axes, respectively, m (ft)

$V$ amplitude of velocity input to a servo, rad/sec or m/sec (ft/sec)

$\vec{V}$ vector which defines commanded position of target image on the screen relative to the azimuth-mirror gimbal center, m (ft)

$\vec{V}_A$ vector which defines position of arbitrarily chosen point on transparency relative to $X_T, Y_T, Z_T$ axis system of sky-Earth projector, m (ft)

$\vec{V}_{em}$ vector which defines position of elevation mirror relative to center of projection sphere, m (ft)

$\vec{V}_L$ vector which defines position of lamp relative to center of projection sphere, m (ft)

$\vec{V}_o$ vector which defines projection on the screen of arbitrarily chosen point in sky-Earth scene relative to observer, m (ft)

$\vec{V}_t$ vector which defines position of target image relative to center of elevation mirror, m (ft)

$\vec{V}_{TCE}$ vector which defines position of center of Earth transparency relative to center of sky-Earth gimbal, m (ft)

$\vec{V}_{TCS}$ vector which defines position of center of sky transparency relative to center of sky-Earth gimbal, m (ft)

$\vec{v}_p$ vector which defines position of arbitrarily chosen point on transparency relative to lamp, m (ft)

$v_{px}, v_{py}, v_{pz}$ x-, y-, and z-components of vector $\vec{v}_p$, m (ft)

$\hat{v}_t$ unit vector coincident with vector $\vec{V}_t$, m (ft)

$v_{tx}, v_{ty}, v_{tz}$ x-, y-, and z-components of vector $\hat{v}_t$, m (ft)

$X', Y', Z'$ axis system parallel to attacker body-axis system with its origin at center of surveyor's transit, dimensionless

$X_A, Y_A, Z_A$ attacker body-axis system, dimensionless

$X'_A, Y'_A, Z'_A$ axis system parallel to attacker body-axis system but with its origin at center of azimuth target-projection mirror, dimensionless

$X_B, Y_B, Z_B$ target body-axis system, dimensionless

$X_c, Y_c, Z_c$ axis system which is fixed to TV camera, dimensionless

$X_{em}, Y_{em}, Z_{em}$ axis system rotating with target elevation mirror, dimensionless

$X_I, Y_I, Z_I$ inertial-axis system which rotates with transparency and defines zero reference point on transparency, dimensionless

$X_{LP}, Y_{LP}, Z_{LP}$ target-projector line-of-sight axis system as projected backward from projection screen through TV system to camera, dimensionless

$X_T, Y_T, Z_T$ axis system fixed to and rotating with sky-Earth pitch gimbal, dimensionless

$X'_T, Y'_T, Z'_T$ axis system fixed to sky or Earth transparency which is yawed by the angle $-\psi_B$ with respect to $X_I, Y_I, Z_I$ axis system, dimensionless

$X_\alpha, Y_\alpha, Z_\alpha$ axis system fixed to and rotating with target-model antilock gimbal, dimensionless

$X_\gamma, Y_\gamma, Z_\gamma$ axis system fixed to base of target-projection system, dimensionless

$X'_\gamma, Y'_\gamma, Z'_\gamma$ axis system rotating with target azimuth mirror having the $Y'_\gamma$-axis coincident with vector $\vec{E}$ and the $X'_\gamma Y'_\gamma$-plane coincident with the $X_\gamma Y_\gamma$-plane, dimensionless

$X''_\gamma, Y''_\gamma, Z''_\gamma$ axis system rotating with target elevation mirror having the $Y''_\gamma$-axis collinear with vector $\vec{E}$ and the $X''_\gamma$-axis separated from final projected line of sight by constant toe-in angle $\delta$, dimensionless

$x_{BA}, y_{BA}, z_{BA}$ coordinates of target in attacker body-axis system, m (ft)

$\dot{x}_{BA}, \dot{y}_{BA}, \dot{z}_{BA}$ velocities of target in attacker body-axis system, m/sec (ft/sec)

$x_l$ projection-lens zoom servo command, V

$x_m$ camera-lens zoom servo command, V

$x_{\gamma A}, y_{\gamma A}, z_{\gamma A}$ target relative coordinates on surface of sphere defined in tilted $X_\gamma, Y_\gamma, Z_\gamma$ axis system, m (ft)

$\dot{x}_{\gamma A}, \dot{y}_{\gamma A}, \dot{z}_{\gamma A}$ target relative velocities on surface of sphere defined in tilted $X_\gamma, Y_\gamma, Z_\gamma$ axis system, m/sec (ft/sec)

$Y_m$ lateral dimension of target model, m (ft)

$Y_1$ lateral dimension of projected target image, m (ft)

$Y_1'$ lateral dimension of projected target image as reduced due to variation of image projection distance, m (ft)

$Y_2$ lateral dimension of target in the real world, m (ft)

$\alpha$ actual azimuth angle from surveyor's transit to target image, deg

$\alpha'$ predicted azimuth angle from surveyor's transit to target image, deg

$\alpha_E$ antilock-gimbal-angle command of sky-Earth projector, rad

$\dot{\alpha}_E$ computed angular-rate command of sky-Earth projector antilock gimbal, rad/sec

$\alpha_G$ antilock gimbal angle of sky-Earth projector, measured from linear potentiometer, rad

$\alpha_m$ antilock-gimbal-angle command of target-model gimbals, rad

$\beta$ actual elevation angle from surveyor's transit to target image, deg

$\beta'$ predicted elevation angle from surveyor's transit to target image, deg

$\beta_E$ offset angle between antilock-gimbal and roll axes of sky-Earth projector system, rad

$\beta_G = \beta_E$

$\beta_m$ offset angle between antilock and yaw axes of target-model gimbals, rad

$\gamma$ elevation angle of entire target image-projection assembly, rad

$\Delta x, \Delta y, \Delta z$ x-, y-, and z-components of error between sky-Earth and target-mirror pointing vectors as measured on the screen, m (ft)

$\delta$ toe-in angle of target elevation mirror, rad

$\epsilon$ servo position error due to steady-state time lag, m (ft)

$\epsilon_{\eta_L}$ position error for elevation servo, m (ft)

$\epsilon_{\xi_L}$ position error for azimuth servo, m (ft)

$\eta_L$ elevation-gimbal-angle command of target-image projector, rad

$\eta'_L$ elevation-mirror gimbal angle of target projector, measured from linear potentiometer, rad

$\dot{\eta}_L$ computed angular-rate command of target elevation mirror, rad/sec

$\theta_E$ pitch-gimbal-angle command of sky-Earth projector, rad

$\dot{\theta}_E$ computed angular-rate command of sky-Earth pitch gimbal, rad/sec

$\theta_G$ pitch gimbal angle of sky-Earth projector, measured from linear potentiometer, rad

$\theta_m$ pitch-gimbal-angle command of target-model gimbals, rad

$\theta_1$ arbitrary value of pitch-gimbal angle used in development of equations for sky-Earth lamp drive, rad

$\theta_2$ arbitrary value of aircraft pitch angle used in development of equations for sky-Earth lamp drive, rad

$\xi_L$ azimuth-gimbal-angle command of target-image projector, rad

$\xi'_L$ azimuth-mirror gimbal angle of target projector, measured from linear potentiometer, rad

$\dot{\xi}_L$ computed angular-rate command of target-azimuth mirror, rad/sec

$\phi_E$ roll-gimbal-angle command of sky-Earth projector, rad

$\dot{\phi}_E$ computed angular-rate command of sky-Earth roll gimbal, rad/sec

$\phi_G$ roll gimbal angle of sky-Earth projector, measured from linear potentiometer, rad

$\phi_m$ roll-gimbal-angle command of target-model gimbals, rad

$\chi$ angle between vectors $\vec{E}$ and $\vec{V}$, rad

$\psi,\theta$ azimuth and elevation angles which define test points used to measure static pointing accuracy of target mirrors, rad

$\psi_B,\theta_B$ azimuth and elevation angles which define location of arbitrarily chosen point of interest on transparency, defined relative to inertial-axis system which is fixed to transparency, rad

$\psi_E$ yaw-gimbal-angle command of sky-Earth projector, rad

$\dot{\psi}_E$ computed angular-rate command of sky-Earth yaw gimbal, rad/sec

$\psi_G$ yaw gimbal angle of sky-Earth projector, measured from linear potentiometer, rad

$\psi_m$ yaw-gimbal-angle command of target-model gimbals, rad

$\omega$ angular velocity, rad/sec

$[\mu]_\lambda$ transformation matrix of a simple rotation through any angle $\mu$ about any axis $\lambda$, dimensionless; that is,

$$[\mu]_X = \begin{bmatrix} 1 & 0 & 0 \\ 0 & \cos\mu & \sin\mu \\ 0 & -\sin\mu & \cos\mu \end{bmatrix}; \quad [\mu]_Y = \begin{bmatrix} \cos\mu & 0 & -\sin\mu \\ 0 & 1 & 0 \\ \sin\mu & 0 & \cos\mu \end{bmatrix}; \quad [\mu]_Z = \begin{bmatrix} \cos\mu & \sin\mu & 0 \\ -\sin\mu & \cos\mu & 0 \\ 0 & 0 & 1 \end{bmatrix}$$

$[\ ]^T$ denotes transpose of a matrix

## SIMULATOR DESCRIPTION

### Basic System

The basic Langley differential maneuvering simulator (DMS) is depicted in figure 1. The simulator consists of identical cockpits, target-image projectors, and sky-Earth projectors located in adjacent 12.2-m-diameter (40-ft) projection spheres. Target-image generators located externally to the sphere provide the correct image of the second aircraft to the target-image projectors via independent closed-circuit television systems. All control of these systems as well as interface with the remote central computer is provided by the system control console located between the two spheres. Figure 2 is a photograph of the pilot and shows the cockpit and external visual scene. All computing associated with the system is performed on a CDC 6600 computer operating in real time at 32 iterations per second.

The assembly of the equipment in each projection sphere is shown in figure 3. The spheres are constructed of 1.27-cm-thick (0.5-in.) steel with a radius tolerance of 0.238 cm (3/32 in.) over any $4^\circ$ segment. The overall radius tolerance is 1.27 cm (0.5 in.). The internal (projection) surface of each sphere is painted with a flat white paint and provides approximately unit optical gain. This finish was chosen over a more directional finish with higher gains in order to provide uniform reflectivity. The unit-gain finish has the added advantages of being less expensive and easier to maintain.

The design goal of the bridge structures which support the cockpits and projectors was to avoid natural frequencies below 50 Hz in order to prevent oscillatory movement of the projectors or cockpits. In addition, the cockpit support structures are separated from the projector support structures to prevent cockpit vibrations (buffet) from affecting the projectors. The projection equipment and its supporting structures were designed to provide a visual field of view of approximately $\pm 170^\circ$ in the horizontal and $+110^\circ$ to $-20^\circ$

in the vertical. The -20° limit is due to the simulator cockpit. The field of view is reduced to the proper level for a particular aircraft by masking the cockpit canopy.

## External Visual Scene

Sky-Earth projection.- The pilot's external visual scene is composed of the sky-Earth and target-image projections superimposed on the sphere surface. The sky-Earth projector provides a visual reference in three degrees of unrestricted rotational freedom over the entire field of view. The sky-Earth projector and its support structure are shown in figure 4. The projector consists of two dye-painted plexiglass hemispheres (one for sky and one for Earth) mounted on a projector head containing the point light sources. The projector head (fig. 5) is mounted in a four-axis, 30°-offset gimbal system. The outer, or antilock, gimbal angle $\alpha_E$ is driven by commands calculated to prevent the three inner gimbal angles $\psi_E$, $\theta_E$, and $\phi_E$ from attaining a gimbal-lock condition. It is offset by 30° rather than being in a fully orthogonal position in order to minimize shadows caused by the gimbal system. A description of the gimbal system and its drive equations is given in reference 1. Both light sources of the projector are mounted on a single shaft with a fixed length and are driven in the three axis directions by orthogonal servos in a manner which guarantees that the two hemispheres will map correctly on the projection screen. The sky-Earth projector has no provision for terrain translations; however, any fixed altitude may be represented by altering the horizon masking of the sky and Earth spheres.

The light sources in the projector have their intensity controlled as a function of time spent at a particular g-level, as will be discussed later. This varies the background brightness from its normal level of approximately 0.14 cd/m$^2$ (0.04 fL) down to 0.

Target-image projection.- The target-image projection subsystem (fig. 6) consists of a cathode-ray tube (CRT) projector and its associated electronics, zoom lens, focus lens, fixed mirror, and two-axis pointing-mirror system, which are all servo driven. The CRT projector is a modified commercial kinescope unit with a resolution of 900 lines, an average long term brightness of 5650 cd/m$^2$ (1650 fL), and a highlight brightness of 34 260 cd/m$^2$ (10 000 fL) on the face of the CRT. Forced-air cooling of the faceplate is provided. The CRT image is projected through a zoom lens having a magnification range of from $\times$ 1.18 to $\times$ 10, a focus lens, and the three mirrors of the pointing-mirror system. The projection zoom lens (in conjunction with one in the target-image generator) provides the target-range information. Range is limited to a variation of from approximately 92 m (300 ft) to 12.2 km (40 000 ft), depending on the actual size of the full-scale aircraft whose image is being projected. The near range limit is a design compromise with the problem of providing adequate target brightness through realizable optics. The focus lens is driven as a function of the image projection distance (i.e., the distance from the

lens to the surface of the sphere), which varies as the mirrors move since they are not located in the center of the sphere. The focus lens then projects onto the fixed, first mirror of the pointing-mirror system. The pointing mirrors provide unrestricted rotational freedom in both elevation and azimuth. The brightness of the projected image varies from 1.7 cd/m$^2$ (0.5 fL) to 3.4 cd/m$^2$ (1.0 fL) for a source brightness of 34 260 cd/m$^2$ (10 000 fL) and is a function of zoom setting, zoom lens aperture and transmission, and mirror reflectance. The mirror drive equations are corrected for the parallax error caused by their displacement from the pilot's eye. (See appendix A for details of these corrections.)

## Target-Image Generation

The target-image generators (TIG) provide the video image to the CRT projectors with correct aspect orientation of the model of the second aircraft. The system (fig. 7) consists of a scale model of the target aircraft mounted in a four-axis, offset-gimbal system; two folding mirrors; a TV camera with a servo-driven zoom lens; and model lighting and cooling equipment. The target model is always sized to give approximately 18 cm (7 in.) of wing span and is painted with a white matte paint to reduce highlights. The model, shown in figure 8, is mounted by four wires attached to both the nose and the tail and is driven in roll (inner gimbal) by a small cable. The four wires on the tail serve as conductors to a slip ring mounted in the tail of the model. This allows future addition of movable control surfaces on the models. The model is mounted in a four-axis gimbal system identical with the one described for the sky-Earth projector except for gimbal order. The model is viewed by the camera through the zoom lens and folding mirrors. The two folding mirrors are 95 percent reflective and serve to reduce the size of the TIG enclosure while maintaining the required distance between camera and model. The fixed distance between the camera and model, 2.03 m (80 in.), is chosen to give correct perspective at approximately 213 m (700 ft), depending on model scale factor. The camera zoom lens is a commercial 20-to-1 unit modified to be servo driven over a range of 16 to 1. It works in conjunction with the projector zoom lens to give a total magnification change of 160 to 1.18.

The model is illuminated by four 250-watt, quartz iodide lamps equipped with air-cooled infrared filters to prevent excessive heating of the model or servo components on the gimbal arms.

## Cockpit Subsystem

The cockpit subsystem (fig. 9) is designed to provide the pilot with a realistic environment representative of current high-performance aircraft. Although the cockpit is fixed base, certain kinesthetic cues are provided in the form of control feel, buffet, and

several effects of g-loads, in an effort to gain realism. The instrument panel shown in figure 10 in its present configuration is designed to facilitate changes in order to represent any aircraft. The instruments shown are dc servo, galvanometer, and synchro types. Appendix B is a listing of the instruments presently used along with pertinent information concerning scaling, range, resolution, and accuracy of each instrument. Each cockpit is equipped with a standard aircraft gunsight. A correction lens has been added to form the virtual image of the sight display at the surface of the projection sphere. This avoids parallax errors between the sight display and the target image. The sight has a range-analog bar, roll tabs, lead-angle computing, and the capability for a heads-up display using a CRT in the sight.

Each cockpit is equipped with programmable, hydraulic, control-loading servos in all three axes. The system can be programed for preset nonlinear spring gradients, damping, friction, breakout, dead band, and electrical stops. These functions and their range of adjustment are given in appendix C. Each axis also has inputs for computer-generated forces which are a function of the aircraft dynamic situation.

Aircraft buffet is provided for each cockpit by means of a hydraulic servo which imparts vertical motion to the cockpit. The buffet linkage constrains the motion of the pilot's head to a vertical arc centered on the sphere directly in front of him. This type of motion serves to eliminate any parallax error due to buffet which might affect tracking tasks. The buffet servo is capable of accelerations of ±1g, at frequencies from 0 to 20 Hz at the pilot. The buffet servo is driven by a buffet-signal generator, which is shown functionally in figure 11. The buffet-signal generator utilizes white noise limited to the bandwidth of interest ($f_l$ through $f_h$) for the particular aircraft. The bandwidth-limited white noise is then applied to three structural mode shapers which are adjusted independently for peak gains $\left(M_1, M_2, \text{and } M_3\right)$ up to 15 dB at the frequencies $f_{p_1}$, $f_{p_2}$, and $f_{p_3}$ of the three primary structural modes of the aircraft being simulated. The summed structural mode signals are then modulated by a buffet command signal from the central computer which determines the intensity of the buffet.

The effects of g-loads are simulated by using a standard aircraft g-suit and control valve. The control valve is driven by a pressure feedback servo with a linear electric actuator replacing the slug on the aircraft valve. The g-suit is normally inflated to a maximum pressure of 34.5 kPa (5 psid) with a pressure of 3.45 kPa (1/2 psid) at 1g. The pressure of 1/2 psid at 1g allows a feeling of negative g as the pressure drops to 0 in the suit. Additional g-cues are provided by controlling the brightness of the sky-Earth scene, all cockpit lights, and the target image as a function of time spent at a particular normal acceleration. The dimming of the target lags the dimming of the sky-Earth scene and instruments in an effort to simulate tunnel vision. The lights and target are completely extinguished at high g-loads and the pilot, although still conscious, has no visual reference.

Each cockpit is equipped with a sound system for added cues. The system includes a preamplifier and power amplifier which drive a set of speakers mounted on each side of the pilot's head. The input to the amplifiers is a balanced mixture of various aircraft sounds. Sounds included are engine noise, wind noise, additional wind noise for speed-brake and flap deployment, afterburner rumble, various modes of weapon firing, and landing-gear deployment.

An angle-of-attack annunciator system which is used for the F-4 fighter airplane has been added to each cockpit to give the pilot a system of index lights and an aural tone in addition to the standard instrument display of angle of attack. The operation of this system is illustrated in figure 12. The bar chart representing the aural tones shows some overlap in each of the three frequencies allowing good resolution of angle of attack between 15.0 and 22.3 units. The range of angle of attack may be varied for different aircraft.

## Control Console

The control console provides operating and monitoring functions for all equipment associated with the simulator. The console contains all equipment required for interface with the central computer and provides all controls and indicators necessary for local operation of the systems. An array of test and monitoring equipment, sufficient to evaluate system performance and assist in systems maintenance, is included in the console. The control console is divided into five sections, as shown in figure 13.

Section I of the console contains the sound system, all video interface equipment, the brightness and cooling controls for the sky-Earth and target lighting, and the intercom system. The video system includes monitors for each model, a scope to monitor the voltage levels, test equipment for setting up the video, and a switching matrix which allows control of all the video inputs and outputs. The intercom system also contains a switch matrix which allows control of the talk and receive buses of each of 11 stations.

Console section II contains the controls and indicators necessary for control, operation, and monitoring of the system. A view of section II is shown in figure 14. For monitoring purposes, all discrete inputs and outputs are displayed on lights and all servo positions and drive voltages are displayed on meters. The primary monitoring tool, however, is a voltage-monitor control panel (fig. 15) which allows selection of all computer trunks, patchboard inputs, and all primary signals of all the subsystems. The voltages selected are displayed on a digital voltmeter (DVM), oscilloscope, and strip-chart recorder. For example, each servo has its position, velocity, error, drive signal, commands, and feedback signals selectable by the voltage monitor.

For safety purposes, servo power for each subsystem is sequenced through a 30-second delay when switching from the partial-power condition to full power. Servo

input control allows each servo to be driven from a local potentiometer or from a patchboard which may have either local or computer inputs. The servo operation, as well as the power, is controlled by a comprehensive set of logic equations which sense specified malfunctions, lockouts, switch positions, or computer mode changes. The logic module then controls servo power or inputs as dictated by the logic equations and provides extensive diagnostic indications on an annunciator lamp panel.

Section III of the console contains additional monitoring equipment including the oscilloscope and strip-chart recorder mentioned previously and analog patchboards for interface with the central computer. It also contains all servo electronics chassis which generate the drive signals for the servo power amplifiers or control valves.

Console section IV contains the control-loader electronics, the buffet-signal generator, a discrete-signal patchboard, and a test-signal generator. The test-signal generator can be used in conjunction with the controls in section II to conduct static and dynamic tests of each servo and cockpit instrument.

Section V contains the system power supplies, the solid-state dc power amplifiers for all servo torque motors, the 400-Hz power control, and solid-state instrument drivers for the synchro-type cockpit instruments.

## HARDWARE INTERFACE COMPUTATIONS

The interface math model (fig. 16) converts the simulated attitudes and relative coordinates of the two aircraft into gimbal commands for the sky-Earth and target-image systems. This figure and the following description refer to system A as an example, with an identical math model applicable to system B. Gimbal position commands for all continuous servos (i.e., sky-Earth gimbals, target pointing-mirror gimbals, and target model gimbals) are generated in the form of the sine and cosine of the particular gimbal angle. The servo systems then perform polar conversion to the desired shaft angles. Dynamic compensation of only the sky-Earth gimbal and target-mirror gimbal servos is accomplished by inputting a computed rate-command signal to each servo. The reason for this is that lack of synchronization between the horizon and target positions on the screen is most easily discernible by the pilot. Position commands for all noncontinuous servos (i.e., sky-Earth lamps, camera and projector zoom and focus, and buffet) are directly proportional to the desired positions. There is no rate compensation for the target-model or noncontinuous servos since dynamic synchronization of these servos is not as critical as it is for the sky-Earth and target mirrors.

The computation of the position and rate commands for the sky-Earth four-axis gimbal system requires two types of inputs. The first is the transformation matrix $C_{AI}$ relating the aircraft body-axis system $X_A,Y_A,Z_A$ to the inertial-axis system $X_I,Y_I,Z_I$,

and the second is the aircraft body rates $p_A$, $q_A$, $r_A$ for system A. The outer-gimbal angle $\alpha_E$ is controlled by a logic equation which moves it in such a manner as to prevent the occurrence of gimbal lock in the inner three gimbals (refs. 1 and 2).

The sky-Earth projection lamps must be translated with respect to the transparency in order that the information contained on the transparency be mapped correctly onto the projection screen. The computations of the lamp positions require as input the position commands for the sky-Earth gimbals and the geometrical constants of the gimbal system.

The computations of the position commands $\xi_L$ and $\eta_L$ and rate commands $\dot{\xi}_L$ and $\dot{\eta}_L$ for the target-mirror gimbal system require the relative translational coordinates $x_{BA}$, $y_{BA}$, $z_{BA}$ and relative translational rates $\dot{x}_{BA}$, $\dot{y}_{BA}$, $\dot{z}_{BA}$ of the target as inputs. These computations also generate the image projection distance $|\vec{R}_L|$ which is used as input to the focus and zoom servos. The target coordinates are first scaled to the radius of the projection screen and then transformed to the axis system coincident with the outer base of the mirror gimbals $X_\gamma, Y_\gamma, Z_\gamma$. This transformation includes a translation from the center of the screen to the center of the azimuth-mirror gimbal followed by an elevation rotation of $\gamma = 25^\circ$. The reason for tilting the projection system by $25^\circ$ is to remove the occurrence of the mirror gimbal discontinuity from the pilot's normal field of view.

The target model gimbals require two types of inputs. First is the transformation matrix $m_{bl}$ which defines the transformation from the attacker line-of-sight axis system to the target body-axis system. The second is the sum of the target-mirror gimbal angles $\xi_L + \eta_L$ which decouples the apparent roll of the target image induced whenever the target mirrors move in azimuth or elevation. The roll coupling results from the manner in which the target mirrors are gimbaled. The outer-gimbal angle $\alpha_m$ performs the same function as does the sky-Earth outer-gimbal angle $\alpha_E$.

The camera and projector zoom-lens servos are driven simultaneously to preclude any transients which might occur in midrange if they were driven sequentially. The computation of each of the simultaneous zoom commands requires two inputs. The first is target range $x_{BA}$, $y_{BA}$, $z_{BA}$ in the attacker body-axis system. The second is the lens-to-screen distance variations which would result in a change in image size as the target moves if no correction were made. Correction is accomplished by including the image projection distance $|\vec{R}_L|$ in the zoom-lens calculations.

The equations used to develop these servo commands are outlined in appendix A.

## PROJECTION GEOMETRY

Dynamic analysis of the positional synchronization of the target and sky-Earth images as observed by the pilot could be accomplished only by developing and programing

a math model of the geometrical relationships between the projector gimbals, the screen, and the pilot's eye. Gimbal- and lamp-position inputs to this model were generated by the linear-position-output potentiometers mounted on each servo. The sky-Earth gimbal and lamp positions were used to determine the position vector $\vec{V}_0$ (relative to the pilot) of an arbitrarily chosen point in the scene. The mirror gimbal positions were used to determine the position vector $\vec{B}$ (relative to the pilot) of the target. The comparison of the sky-Earth image point and the target image was made by forming the differences $\Delta x$, $\Delta y$, and $\Delta z$ between the components of $\vec{V}_0$ and $\vec{B}$. Time histories of these differences provided a means for analyzing the dynamic synchronization of the two separately generated images. A complete description of the projection geometry is contained in appendix A.

## HARDWARE-SYSTEMS PERFORMANCE

### Performance Goals of the Integrated Systems

The ultimate goal of the total system is to give each pilot an accurate visual representation of the air-to-air environment with limited kinesthetic cues provided for added realism. Of primary importance in achieving an accurate representation of the external visual scene is synchronization of the servos involved in projecting the scene. This requires that the servos have the same dynamic response (transient and steady state) as well as a high degree of smoothness of movement within the servo operating envelope. The servos must also be capable of providing the highest rates to be encountered in any simulation.

The dynamic response chosen for all servos is a second-order system with a damping ratio of 0.707 and a natural frequency of 25 rad/sec. The response of this second-order system to a step velocity command is shown in figure 17. The steady-state time lag $T$ associated with the figure is derived in appendix D.

The results of this derivation show that the steady-state response of the 0.707 damped, 25 rad/sec, second-order servo to a constant velocity always lags the input by 56.6 msec, while the value of the steady-state position error $\epsilon$ is dependent on the amplitude of the velocity command. Since all servos have the same time lag, synchronization of the various servos is maintained even though the actual velocity, and therefore the position error, may be different for each servo. For high-frequency sinusoidal responses in which a servo may not reach a steady-state velocity, the time lag $T$ increases by approximately 10 percent at 20 rad/sec for the 0.707 damped system. Twenty radians per second is considered to be the upper limit for synchronization in the DMS since it would be nearly impossible for the pilot to detect a lack of synchronization at this rate.

Servo operating envelope.- The requirement for smoothness at low velocities versus the requirement for high rates requires a large dynamic range of the servos. The DMS servos have a dynamic range of 1000 to 1; however, the projection servos require rate commands in addition to the position command to achieve the desired low-velocity smoothness.

The maximum required rates and accelerations to be encountered by each servo are dependent on several variables: gimbal orientations, aircraft body rates, and range and range rate to the target aircraft. Rates and accelerations for the servos were first determined analytically by using extreme cases for each servo. For example, the maximum mirror rates would occur with the two aircraft passing at a close range with a large closure rate. If the two aircraft are assumed to pass at 92 m (300 ft) (selected as minimum usable range because of zoom-lens magnification limits mentioned previously) in the plane of either mirror axis, one servo will be required to provide all of the motion. Assuming a closure rate of 457 m/sec (1500 ft/sec) (approximately 450 knots for each aircraft), the maximum mirror rate is calculated to be 5 rad/sec and the maximum acceleration is 16 rad/sec$^2$.

After the maximum required rates and accelerations have been calculated, the stall torque and no-load velocity can then be specified for each servo. The method used for selecting servo stall torque and no-load velocity assumes the worst-case condition of a simultaneous requirement for maximum torque (for acceleration) and maximum velocity. Therefore, the servo stall torque and no-load velocity are specified as twice the peak values calculated. In addition to the analytical calculations for peak rates and velocities, a computer simulation of the projection servos was developed. The simulated system was driven with various values of aircraft body rates (some representing high performance maneuvers at twice normal rates) to check for any servo rates or accelerations which might exceed the analytical design. (See ref. 1 for details.) A compilation of the final velocities and accelerations of each servo is shown in table I.

Servo static performance.- Static accuracy and repeatability requirements for the projection servos (i.e., sky-Earth, pointing mirror, and zoom servos) are typically twice as severe as the target-model servos. This reflects the view that errors are more critical in the relative position and size of the horizon and the target than in the attitude of the target. The projection servos are required to be accurate to within 0.05 percent of their maximum travel, while the target-model servos are allowed a maximum error of 0.1 percent. All servos meet the accuracy required at any position within the pilot's field of view. In addition to the static accuracy, the servos are required to repeat their output when approached from either direction within 0.02 percent for the projection servos and 0.05 percent for the target-model servos. Again, all servos were well within the tolerance specified. Each servo is also required to have a low static compliance

(high stiffness) in order to reject the effect of load disturbances. The static compliance is specified in terms of a 5-Hz linear spring-inertia system, where the inertia is the final inertia of the servo. A compilation of desired and actual static compliances is shown in table II, which shows that all are well within allowable tolerances.

Servo dynamic performance.- As mentioned earlier, the servo dynamic performance is important to dynamic accuracy and synchronization of the overall scene. The servos were specified to match a 0.707 damped, 25 rad/sec, second-order system over the range from 0 to 3 Hz (0 to 19 rad/sec). The dynamic performance tests consisted of measuring the low-velocity smoothness, the steady-state time lags, the transient response, and the frequency response. The low-velocity smoothness of each servo is shown in table III for the servos moving at 1/200 of their no-load velocity. In most cases not even the rates are discernible to the eye, much less any lack of smoothness.

The servo time lags were determined by measuring the position error $\epsilon$ at a constant velocity. The final steady-state time lags are shown in table IV. The final values are all within ±15 percent of the ideal value (56.6 msec) with the exception of the camera zoom servos $x_m$. The low lag of the camera zoom causes that portion of the magnification due to camera zoom to be slightly greater than desired in a dynamic case. However, the small error in size is not discernible since it is dependent on the velocity of the servo (i.e., the error is largest at maximum velocity), but at maximum velocity the size is changing so rapidly that any error could not be discerned.

The transient response of each servo is measured by comparing the servo to a calibrated second-order model with a damping of 0.707 and a natural frequency of 25 rad/sec. The transient error between the servo output and the second-order model, when both are subjected to step velocity inputs of 1 percent and 20 percent of the servo maximum velocity, is shown in table V. The errors are all within ±20 percent (±25 percent for target-image-generation servos) of the commanded velocity for the 20-percent velocity step. The low-amplitude, 1-percent velocity step exhibits higher percentage errors due to dead bands; however, the absolute transient error is still very small.

Frequency-response measurements were taken on each servo at 1/2, 1, and 3 Hz, and each exhibited the required second-order characteristics over the range of use.

Target-image performance.- The combination of camera zoom lens, TV camera, projection CRT, projection zoom lens, focus lens, and pointing mirrors was tested to determine an end-to-end performance for the target-image system. The projected target image was tested for brightness, resolution, magnification, and optical-axis shift.

The image brightness is greater than 1.7 cd/m$^2$ (0.5 fL) at maximum magnification, while the corner brightness is at least 65 percent of the center brightness. The image resolution was tested both on axis and off axis for the various magnifications.

On-axis resolution is at least 400 TV lines, while off-axis resolution is at least 325 TV lines. Resolution at maximum magnification is 550 TV lines minimum on axis and 325 TV lines minimum off axis. The total magnification of the two zoom lenses is a function of image projection distance as well as range. Target-image size was checked at various ranges and found to be accurate within ±5 percent. The shift in the optical axis from minimum to maximum magnification was found to be less than 3 arc min.

## Performance of the Integrated System

After the completed DMS system was assembled, installed in the projection spheres, and connected to the central computer program, tests were made to determine the performance of the integrated system. The integrated system was checked for static accuracy of the pointing mirrors and sky-Earth projector and for dynamic synchronization of the projection systems. The absolute static accuracy of the pointing mirrors in positioning the target image is generally considered more critical than the position of the horizon since the horizon normally has a haze band associated with it. This is especially true in the forward section of the sphere where the image is located during a tracking task.

Static accuracy.- The static accuracy of the pointing-mirror system is subject to errors in the static accuracy of the servos, the orthogonality of the two mirror axes, the location and alinement of the gimbals within the sphere, and the accuracy of the program which computes the mirror commands. The procedure used to check the mirror accuracy was to position a surveyor's transit near the sphere center and use the transit to sight the target for different input commands to the mirrors. The transit angles, termed $\alpha$ and $\beta$, are shown in figure 18. A separate computer program was used to calculate exact transit angles with only mirror input data and geometrical constants. These exact angles are termed $\alpha'$ and $\beta'$ and the differences $\alpha - \alpha'$ and $\beta - \beta'$ give the absolute errors in the mirror pointing accuracy. The errors at each test point are shown in table VI for sphere A and sphere B. A necessarily limited number of test points was taken, with the majority being in the frontal region. The errors in the frontal region ($\pm 20^{\circ}$ in azimuth and elevation) are less than 9 arc min, while for the remainder of the sphere they are less than 30 arc min. In comparison, the pilot's interpupillary eye distance represents a parallax error of approximately 30 arc min, and the center dot of the gunsight subtends 4.5 arc min.

The static accuracy of the sky-Earth scene is subject to two types of error: those in the location of the sky-Earth transparencies in the sphere and those in the location of the light source with respect to the transparency. The location of the transparencies within the sphere is subject to errors in the four-axis gimbal drives, the alinement and location of the entire gimbal assembly within the sphere, the orthogonality of the gimbal

axes, and the accuracy of computation of the servo drives. The location of the lamps within the transparency is subject to errors in the accuracy of the lamp-servo drives, the mechanical alinement and location of the lamp servos with respect to the transparency, the orthogonality of the lamp-servo drive axes, the conformity of the transparency, and the computational accuracy of the lamp-servo commands.

The accuracy of the sky-Earth mapping is much more sensitive to errors in the location of the lamps with respect to the transparencies than to errors in the location of the transparencies within the spheres. This can be seen by considering two examples. First, consider that the transparency center is 1.27 cm (0.5 in.) higher than it should be, but with the lamp positioned correctly within the transparency. This would reflect to the sphere directly as an error of 1.27 cm (0.5 in.) in the location of the horizon line. Now, consider the lamp position to be in error by 1.27 cm (0.5 in.) within the transparency, but with the transparency location correct (fig. 19). This angular error reflected to the surface of the sphere approximately 686 cm (270 in.) away is magnified by the ratio $R_1/R_2$, or 30 times.

A measure of the error in location of the transparency with respect to the sphere center was made with the same transit setup which had previously been used to check the target-mirror pointing accuracy. However, there is no fixed reference point at the transparency center on which to sight in order to map its location as the gimbals rotate. Therefore, the only way to make the measurement was to sight on the lamp as the gimbals rotated while keeping the lamp servos fixed with respect to the pitch gimbal. After removal of biases which represent translational errors between the transit and gimbal center, the maximum error in lamp position was found to be approximately 1.52 cm (0.6 in.). This was an extreme value and most values were found to be within 0.76 cm (0.3 in.). This error in the position of the transparency center with respect to the sphere center projects onto the sphere with a magnification of 1 or less.

Because of the sensitivity of projected scene accuracy to errors in lamp position within the transparency, care was taken during assembly to insure the orthogonality of $b'_{ox}$, $b'_{oy}$, $b'_{oz}$ axes and precise alinement of the axes with respect to the transparency. The buildup of tolerances of these alinements coupled with known servo accuracy and transparency accuracy leads to a maximum error of 0.076 cm (0.03 in.) in lamp location. This error reflected to the sphere results in a maximum error of the order of 2.54 cm (1.0 in.) in the location of the horizon line. This corresponds to an angular error of approximately 15 arc min.

The resolution of the scene is important in a discussion of accuracy of the presentation. In the DMS, care has been taken to avoid distinct lines near the horizon and sharp detail anywhere in the projected scene. This is accomplished primarily by painting the Earth transparency to show no detail near the horizon, increasing to moderate detail

straight down, and painting the sky a solid blue. The masking near the base of each transparency allows for small irregularity (±2.54 cm (1 in.) on the screen) in each horizon line; however, the horizon lines overlap by approximately 10 cm (4 in.). This tends to make the exact horizon line (from the Earth transparency) somewhat hazy; however, it is still definable. Finally, the incandescent lamps used have a filament approximately 0.51 cm (0.2 in.) long which does not project extremely sharp images because of the size of the light source (i.e., not a perfect point light source). In view of this kind of scene resolution, the previously discussed sky-Earth projector errors would not be discernible unless they were much larger than actually measured.

Dynamic accuracy.- The dynamic accuracy of each servo has already been discussed; however, the synchronization of the projected scene is dependent on the interaction of all the projection servos. Dynamic errors in the system come from the differences in the servo dynamic characteristics – primarily differences in steady-state time lags.

The dynamic errors are difficult to predict because they depend on the projection geometry and the resulting rate of each servo involved in projecting the scene. In order to see the effect of dynamic synchronization errors, a simplified case of pure yaw motion was chosen. In this case any observed vertical error between target and horizon comes only from the mismatch of the two mirror servos since the sky-Earth projector remains fixed with the exception of the yaw motion. The geometry of this situation is shown in figure 20 with the azimuth plane of motion of $\xi_L$ at the angle of $25^o$ with respect to the horizontal (sphere equator) and the elevation $(\eta_L)$ axis of rotation orthogonal to the azimuth axis of rotation. For a sinusoidal input ($A \sin \omega t$), where $A$ is 3.0 rad and $\omega$ is 1.57 rad/sec, the image starts in front and moves approximately $170^o$ (either right or left) along the equator of the sphere toward the rear. For this case, each servo $(\eta_L$ and $\xi_L)$ reaches its maximum rate at approximately the point at which the plane of rotation of the azimuth mirror crosses the horizontal (an azimuth of $-90^o$). This commanded position is on the sphere surface directly to the left of center. The mirror rates for this case (taken from computer runs) are 2.00 rad/sec for $\xi_L$ and 0.897 rad/sec for $\eta_L$. The amount by which each axis of the display lags the commanded position can now be computed as

$$\epsilon = \omega T R_1$$

where

$\epsilon$ position error at the sphere surface, m (in.)

$\omega$ angular velocity, rad/sec

$T$ predicted servo steady-state time lag, 56.6 msec

$R_1$ radius of the projection sphere, 6.096 m (240 in.)

Thus, the errors are

$$\epsilon_{\xi_L} = 0.68 \text{ m } (26.8 \text{ in.})$$

$$\epsilon_{\eta_L} = 0.31 \text{ m } (12.2 \text{ in.})$$

The predicted position for the ideal case of identical time lags as shown in figure 20 is 56.6 msec behind the commanded position, but the target image is moving along the sphere equator as commanded and synchronization is maintained. Now by taking the actual servo time lags (table IV), the magnitude of errors due to mismatch in servo dynamics can be calculated as before. Time lags are used for sphere B since they show the largest mismatch and consequently the largest errors. These errors are

$$\epsilon_{\xi_L} = 0.756 \text{ m } (29.8 \text{ in.})$$

$$\epsilon_{\eta_L} = 0.241 \text{ m } (9.48 \text{ in.})$$

The actual image position due to these errors is shown in figure 21 and has error components of 0.089 m (3.5 in.) in $Z_A$ and 0.0445 m (1.75 in.) in $X_A$, but no error in $Y_A$ since the point chosen is on the $Y_A$-axis.

As previously mentioned, prediction of errors for other maneuvers in which all the projection servos are moving would be extremely difficult; therefore, a program was set up to evaluate the errors. The cases chosen for analysis were pure pitch, roll, and yaw of the primary aircraft with the target fixed in space. For the pitch and yaw maneuvers the image started straight ahead, while the roll maneuver was done with the image at $90^{\circ}$ (right or left) with respect to the primary aircraft. The digital computer program computed line-of-sight vectors $\left(\vec{B} \text{ and } \vec{V}_0\right)$ for the target and for the sky-Earth scene on the basis of the projection geometry and the actual servo positions. (See appendix A for details.) For matched servo responses the two vectors should always be coincident on the sphere surface. The components of the difference between the two vectors $\Delta x$, $\Delta y$, and $\Delta z$, as shown in figure 22, were computed and recorded on strip-chart recorders for each case (i.e., pitch, roll, and yaw). The summary of the maximum corresponding angular errors for sinusoidal inputs ($A \sin \omega t$) is shown in table VII. The large-amplitude ($A = 170^{\circ}$, $\omega = 1.57$ rad/sec) inputs represent peak aircraft rates of 4.75 rad/sec, while the smaller inputs ($A = 40^{\circ}$, $\omega = 1.57$ rad/sec) represent peak rates of 1.1 rad/sec. The

errors listed in table VII are the peak errors which occur at the peak rates. It should be noted that these include all static positioning errors as well as dynamic effects. Comparison of the calculated errors for the large-amplitude yaw case with the strip-chart recordings yields identical results for $\Delta x$, $\Delta y$, and $\Delta z$ at the maximum mirror rates. The recordings corresponding to this case are shown in figure 23. It can be seen from the recordings that maximum $\Delta z$ occurs at maximum mirror rates and that $\Delta y$ equals zero at this point.

The maximum error for all cases shown in table VII is $1.5^{\circ}$; however, this occurs at a roll rate of 270 deg/sec, a condition which makes visual detection of synchronization error practically impossible. The same approximate percentage holds (i.e., the maximum error is less than 1 percent of the rate) for the lower rates.

Performance assurance.- In order to assure that the system maintains its initial accuracy, periodic tests are conducted on the servo and video performance. The servos are checked for both static and dynamic performance, while the video system undergoes a standard setup procedure to assure its performance.

Tests are performed weekly to see that all servos meet their original static performance. Static checks are performed at 0 and $\pm 135^{\circ}$ for continuous servos and at 0 and $\pm$ maximum displacement for noncontinuous servos. The $\pm 135^{\circ}$ test points are chosen for the continuous servos since they represent points of maximum error due to worst-case linearity of the sine-cosine feedback potentiometers at these points.

At the conclusion of initial performance tests, a "standard of performance" test is run on all servos. This test consists of running each servo sinusoidally for 6 to 8 seconds at frequencies of 0.5, 1.0, and 3.0 Hz. Signals are recorded on the eight-channel strip-chart recorder representing servo position, velocity, error, drive, and command signals (sine and cosine) for continuous servos, and velocity for the rate-augmented projection servos. For control-loading-buffet and g-suit servos, signals representing force or pressure feedback are recorded. This "standard of performance" test is performed daily for each servo (approximately 15 min is required for each system) and compared with the original tests. Conditions due to changes in friction or backlash, resonances, dirty tachometer brushes or potentiometer wipers, and changes in power-amplifier limits or motor sensitivities, as well as any failures, can be detected from these comparisons.

The daily procedure for setting up the video involves verification of video voltage levels for the cameras and projectors on the oscilloscope and checking for proper beam current, unblanking threshold, CRT bias, and focus of the projector. In addition, the size and centering of the image are checked daily on a permanent reference mark located on the projection surface. The completion of the static and dynamic tests and the setup procedures (including verification of simulator outputs) requires approximately $1\frac{1}{2}$ hours,

after which the DMS is ready for research use with the assurance that the hardware will provide accurate data.

## CONCLUDING REMARKS

The Langley differential maneuvering simulator provides an accurate and realistic (with the exception of some kinesthetic cues) means of simulating aircraft or spacecraft operating in a differential mode. The principal limitations of the simulator are the absence of primary motion cues and the limit on minimum range which would probably prohibit docking maneuvers. The absence of terrain translational cues might have some effect on low-altitude maneuvering. However, methods for incorporating terrain translations including altitude cues (terrain growth) are being pursued.

The system is designed to represent accurately all aircraft motions (as determined by the math model) and relative translations (between the two aircraft) within a large operational range, which covers the operational envelope of most aircraft. The accuracy of the visual presentation (including scene synchronizations) has been documented and subjectively evaluated for 1 year with no discernible visual cue errors.

The control systems, indicators, buffet generator, g-suit, and sound system provide the pilot with adequate cues to perform his task. Experience has shown that 5 to 10 hours of training time may be required for each new pilot to adapt to the simulator, depending on the task to be performed.

Langley Research Center,
National Aeronautics and Space Administration,
Hampton, Va., May 14, 1973.

## APPENDIX A

## INTERFACE MATH MODEL AND PROJECTION GEOMETRY

The interface mathematical model serves to transform the orientations, in inertial space, of the two aircraft into the gimbal positions of the projection servos. The projection geometry is an analytical tool for studying the synchronization of the separately gimbaled projection systems. The math módel for controlling the major subsystems (sky-Earth projector, target pointing mirror, target model, target zoom and focus) and the projection geometry are outlined in the following sections.

### Sky-Earth Projector

The sky-Earth projector consists of the four-axis gimbal system, which positions the sky-Earth transparencies, and the translational system, which positions the lamps with respect to the transparencies. The positioning of the lamp as a function of gimbal positions provides correct mapping of information from the transparencies to the projection screens. Since this correct mapping is maintained for all gimbal orientations, it is possible in the following derivation to treat the sky-Earth projector as if both the inertial-axis system $X_I, Y_I, Z_I$ and attacker body-axis system $X_A, Y_A, Z_A$ have their origins located at the common center of rotation of the gimbals and that the inertial-axis system is rotating with the sky-Earth transparencies while the body-axis system is fixed. Also, the pilot is assumed to be at the aircraft center of gravity and the body-axis system is at the pilot's eye.

Sky-Earth gimbals.- Figure 24 illustrates the geometrical arrangement of the sky-Earth four-axis gimbal system. The transformation from inertial- to body-axis system may be defined in terms of the matrix $C_{AI}$ as

$$\begin{bmatrix} X_A \\ Y_A \\ Z_A \end{bmatrix} = C_{AI} \begin{bmatrix} X_I \\ Y_I \\ Z_I \end{bmatrix} \tag{A1}$$

where

$$C_{AI} = \left[c_{ij}\right] \qquad (i,j = 1, 2, 3)$$

The matrix $C_{AI}$ is derived from the aircraft body rates $p_A$, $q_A$, $r_A$ by means of the quaternion rate equations. (See refs. 3 and 4.) The axis transformation may also be defined in terms of the gimbal angles of the sky-Earth projector as

$$\begin{bmatrix} X_A \\ Y_A \\ Z_A \end{bmatrix} = \left[\alpha_E\right]_X \left[\beta_E\right]_Y \left[\phi_E\right]_X \left[\theta_E\right]_Y \left[\psi_E\right]_Z \begin{bmatrix} X_I \\ Y_I \\ Z_I \end{bmatrix} \tag{A2}$$

The gimbal-position commands in equation (A2) are defined as positive when the scene moves in the direction defined as positive vehicle motions by the pilot. Equating equations (A1) and (A2) results in

$$\left[\alpha_E\right]_X \left[\beta_E\right]_Y \left[\phi_E\right]_X \left[\theta_E\right]_Y \left[\psi_E\right]_Z = C_{AI} \tag{A3}$$

The angle $\beta_E$ is a constant and the redundant-outer-gimbal angle $\alpha_E$ is defined by

$$\dot{\alpha}_E = H\left[\operatorname{sgn}\left(-\sin\theta_E \sin\phi_E\right)\left(\left|\theta_E\right| - 60^\circ\right)\right]$$

where $\operatorname{sgn}\left(-\sin\theta_E \sin\phi_E\right)$ is equal to the sign of the product of $-\sin\theta_E$ and $\sin\phi_E$, and

$$H = 0 \qquad \left(\theta_E < 60^\circ\right)$$

$$H = 1 \qquad \left(\theta_E > 60^\circ\right)$$

References 1 and 2 contain further descriptions of the outer-gimbal drive logic.

Now that $\alpha_E$ and $\beta_E$ have been defined, equation (A3) may be solved for the remaining three inner-gimbal angles by operating with the transpose matrices:

$$\left[\phi_E\right]_X \left[\theta_E\right]_Y \left[\psi_E\right]_Z = \left[\beta_E\right]_Y^T \left[\alpha_E\right]_X^T C_{AI} \tag{A4}$$

where $\left[\ \right]^T$ denotes the transpose of a matrix. Equation (A4) may be expanded to give the gimbal-angle commands:

$$\sin \theta_E = -\left(C_{13} \cos \beta_E + C_{23} \sin \alpha_E \sin \beta_E + C_{33} \cos \alpha_E \sin \beta_E\right) \tag{A5}$$

$$\cos \theta_E = \left(1 - \sin^2\theta_E\right)^{1/2} \tag{A6}$$

$$\sin \psi_E = \frac{C_{12} \cos \beta_E + C_{22} \sin \alpha_E \sin \beta_E + C_{32} \cos \alpha_E \sin \beta_E}{\cos \theta_E} \tag{A7}$$

$$\cos \psi_E = \frac{C_{11} \cos \beta_E + C_{21} \sin \alpha_E \sin \beta_E + C_{31} \cos \alpha_E \sin \beta_E}{\cos \theta_E} \tag{A8}$$

$$\sin \phi_E = \frac{C_{23} \cos \alpha_E - C_{33} \sin \alpha_E}{\cos \theta_E} \tag{A9}$$

$$\cos \phi_E = \frac{-C_{13} \sin \beta_E + C_{23} \sin \alpha_E \cos \beta_E + C_{33} \cos \alpha_E \cos \beta_E}{\cos \theta_E} \tag{A10}$$

The rate-command signals for the inner three gimbals may be derived in a fashion similar to the rate equations for a normal three-axis system (refs. 1, 2, and 5) and result in the following expressions:

$$\begin{aligned}\dot{\phi}_E = {} & \left(p_A - \dot{\alpha}_E\right)\left(-\sin \beta_E \cos \phi_E \tan \theta_E + \cos \beta_E\right) + q_A\left(\cos \alpha_E \sin \phi_E \tan \theta_E\right. \\ & \left. + \sin \alpha_E \cos \beta_E \cos \phi_E \tan \theta_E + \sin \alpha_E \sin \beta_E\right) + r_A\left(-\sin \alpha_E \sin \phi_E \tan \theta_E\right. \\ & \left. + \cos \alpha_E \cos \beta_E \cos \phi_E \tan \theta_E + \cos \alpha_E \sin \beta_E\right)\end{aligned} \tag{A11}$$

$$\begin{aligned}\dot{\theta}_E = {} & \left(p_A - \dot{\alpha}_E\right)\sin \beta_E \sin \phi_E + q_A\left(-\sin \alpha_E \cos \beta_E \sin \phi_E + \cos \alpha_E \cos \phi_E\right) \\ & + r_A\left(-\cos \alpha_E \cos \beta_E \sin \phi_E - \sin \alpha_E \cos \phi_E\right)\end{aligned} \tag{A12}$$

$$\dot{\psi}_E = -\left(p_A - \dot{\alpha}_E\right)\sec\theta_E \sin\beta_E \cos\phi_E + q_A \sec\theta_E\left(\sin\alpha_E \cos\beta_E \cos\phi_E\right.$$

$$\left. + \cos\alpha_E \sin\phi_E\right) + r_A \sec\theta_E\left(\cos\alpha_E \cos\beta_E \cos\phi_E - \sin\alpha_E \sin\phi_E\right) \tag{A13}$$

The same sign convention for positive directions that was used for gimbal-position commands applies to the rate commands.

Sky-Earth lamp drives.- In order to project accurately the sky-Earth scene which is painted on the transparencies, certain geometrical constraints must be satisfied. Figure 25 illustrates these constraints for the following sky-Earth scene orientation: The projector is tilted back at a pitch angle equal to $\theta_1$. The points $A_1$ and $A_2$ on the transparency represent the (0,0) point of the horizon, with $A_1$ being projected to the screen by sky lamp $L_1$ and $A_2$ projected by the Earth lamp $L_2$. Since $A_1$ and $A_2$ represent the same point in the projected scene, both must project to the same point $H_R$ on the screen. Point $H_R$ is defined by the angle $\theta_2$ relative to the $X_A$ body axis. The required condition for correct mapping is that $\theta_1 = \theta_2$, and the following constraints must be satisfied to accomplish this:

(1) Each lamp $\left(L_1 \text{ or } L_2\right)$, its transparency center $\left(T_1 \text{ or } T_2\right)$, and the center of the screen C must be collinear.

(2) The lamp-position constraint of $L_1$ with respect to $T_1$ is defined by the proportionality of triangles $A_1T_1L_1$ and $H_RCL_1$.

The following discussion will describe the derivation for the sky lamp $L_1$. A similar derivation could be applied to the Earth lamp $L_2$ with identical results. Constraint (2) for lamp $L_1$ may be expressed as

$$\frac{L_1T_1}{L_1T_1 + T_1C} = \frac{\left|\vec{b}_s\right|}{\left|\vec{b}_s\right| + \left|\vec{a}_s\right|} = \frac{R_2}{R_1} \tag{A14}$$

Equation (A14) may be written as the lamp-constraint equation:

$$\left|\vec{b}_s\right| = \frac{R_2}{R_1 - R_2}\left|\vec{a}_s\right| \tag{A15}$$

where

$$\left|\vec{b}_s\right| = b_{sx}^2 + b_{sy}^2 + b_{sz}^2$$

$$\left|\vec{a}_s\right| = a_{sx}^2 + a_{sy}^2 + a_{sz}^2$$

The lamp-constraint equation (A15) must now be converted into the displacement coordinates of the lamp servo $L_o$ relative to the gimbal center G. This is accomplished by referring again to figure 25 and writing the following expression based on the similarity of triangles $CGT_1$ and $CL_oL_1$:

$$\frac{\left|\vec{a}_o\right|}{\left|\vec{a}_o\right| + \left|\vec{b}_o\right|} = \frac{\left|\vec{a}_s\right|}{\left|\vec{a}_s\right| + \left|\vec{b}_s\right|} \tag{A16}$$

Substituting equation (A15) into (A16) results in

$$\frac{\left|\vec{a}_o\right|}{\left|\vec{a}_o\right| + \left|\vec{b}_o\right|} = \frac{\left|\vec{a}_s\right|}{\left|\vec{a}_s\right| + \frac{R_2}{R_1 - R_2}\left|\vec{a}_s\right|} = \frac{R_1 - R_2}{R_1}$$

or

$$\left|\vec{b}_o\right| = \left|\vec{a}_o\right| \frac{R_2}{R_1 - R_2} \tag{A17}$$

Equation (A17) defines the position of the lamp servo $L_o$ relative to the gimbal center G. Note that in the nonrotating-axis system, $\left|\vec{b}_o\right|$ is a constant since $\left|\vec{a}_o\right|$, $R_1$, and $R_2$ are constants. Since the lamp servos are physically positioned with respect to the rotating pitch gimbal, equation (A17) must be transformed to the rotating $X_T, Y_T, Z_T$ axis system. Performing this transformation gives

$$\left(\vec{b}_o\right)_{rot} = U\left(\vec{b}_o\right)_{fixed} = \frac{R_2}{R_1 - R_2} U\left(\vec{a}_o\right)_{fixed} \tag{A18}$$

where

$$U = \left[\theta_E\right]_Y \left[\phi_E\right]_X \left[\beta_E\right]_Y \left[\alpha_E\right]_X$$

Equation (A18) may then be expressed in component form as a column vector:

$$\begin{bmatrix} b_{ox} \\ b_{oy} \\ b_{oz} \end{bmatrix}_{rot} = \frac{R_2}{R_1 - R_2} U \begin{bmatrix} S_x \\ 0 \\ S_z \end{bmatrix} \tag{A19}$$

where

$$\left(\vec{b_o}\right)_{rot} = \begin{bmatrix} b_{ox} \\ b_{oy} \\ b_{oz} \end{bmatrix} \qquad \left(\vec{a_o}\right)_{fixed} = \begin{bmatrix} S_x \\ 0 \\ S_z \end{bmatrix}$$

Equation (A19) is the final equation for the lamp servo drives and it illustrates the parametric dependence of the lamp position on the gimbal-offset coordinates $S_x$ and $S_z$ and the variable dependence of the lamp position on the gimbal angles $\alpha_E$, $\beta_E$, $\phi_E$, and $\theta_E$.

Derivation of equation (A19) on the basis of the Earth lamp $L_2$ yields identical results based on the similarity of triangle $L_2A_2T_2$ to triangle $L_2H_RC$ and triangle $CGT_2$ to triangle $CL_oL_2$.

## Target-Image Projection and Generation

Target-mirror gimbals.- The relative location of the target with respect to the attacker body-axis system is dependent on the attitude of the attacker with respect to the inertial-axis system and on the relative translational coordinates (in the inertial system) between the two aircraft. This information is provided to the interface math model in the form of the coordinates $x_{BA}$, $y_{BA}$, $z_{BA}$ and velocities $\dot{x}_{BA}$, $\dot{y}_{BA}$, $\dot{z}_{BA}$ of the target in the attacker body-axis system. If the target pointing mirrors could be placed coincident with the observer's eye location, then the generation of the line-of-sight (LOS) angles would be a simple trigonometric vector resolution.

The actual mechanical configuration of the mirrors is illustrated in figure 26 where the following mechanical displacements and rotations are shown for the condition of $\xi_L = \eta_L = 0$:

(1) The center of rotation of the azimuth mirror is displaced longitudinally and vertically with respect to the center of the sphere by $M_x$, 0, $M_z$.

(2) The entire mirror assembly is tilted up at an angle of $\gamma = 25^o$ to place the effect of the mirror-gimbal discontinuity outside the pilot's normal field of view.

(3) Note that azimuth motion is generated by rotating both the azimuth and elevation mirrors about the $Z_\gamma$-axis through the angle $\xi_L$. Elevation motion is generated by rotating the elevation mirror only about the $Y''_\gamma$-axis through the angle $\eta_L$. As a result of this gimbal configuration there is always a constant angle between each mirror and the projector line of sight as the line of sight traverses between the mirrors. This provides an undiminishing projected field of view for any location of the target and requires that the two mirrors be separated by the distance $|\vec{E}|$ to provide for mechanical clearance.

(4) The elevation mirror has a constant "toe-in" angle of rotation defined as $\delta$ about the $Z''_\gamma$-axis; that is, the angle between vector $\vec{E}$ and the final projector line of sight $\vec{R}_L$ is not $90^o$. This last rotation was added in an effort to correct, in the mirror-gimbal calculations, for the effect of the displacement between mirror centers.

The constant displacement $M_x$, 0, $M_z$ and the tilt angle $\gamma$ are accounted for by simply transforming the target coordinates from the attacker body-axis system $X_A, Y_A, Z_A$ to the $X_\gamma, Y_\gamma, Z_\gamma$ axis system. This transformation consists of a translation $M_x$, 0, $M_z$ followed by a rotation $\gamma$ as defined in the equation

$$\vec{V} = \begin{bmatrix} x_{\gamma A} \\ y_{\gamma A} \\ z_{\gamma A} \end{bmatrix} = \begin{bmatrix} \cos\gamma & 0 & -\sin\gamma \\ 0 & 1 & 0 \\ \sin\gamma & 0 & \cos\gamma \end{bmatrix} \begin{bmatrix} \frac{x_{BA}}{R_{BA}} R_1 - M_x \\ \frac{y_{BA}}{R_{BA}} R_1 + 0 \\ \frac{z_{BA}}{R_{BA}} R_1 - M_z \end{bmatrix} \tag{A20}$$

The terms $\frac{x_{BA}}{R_{BA}} R_1$, $\frac{y_{BA}}{R_{BA}} R_1$, and so forth simply scale the real-world target coordinates to the surface of the screen.

A solution for $\xi_L$ and $\eta_L$ which eliminates the need to solve nonlinear algebraic equations may be found by considering the geometry in figure 27. Since the toe-in angle $\delta$ is a constant, any motion of the elevation mirror about $Y'_\gamma$ through an angle $\eta_L$ will move the projector line of sight $\vec{R}_L$ along the surface of a cone. The axis of the cone is the vector $\vec{E}$ and the semiapex angle is $\frac{\pi}{2} - \delta$. Elements of the cone surface are the line segments OA, OB, and $\vec{R}_L$. From the figure, the correct value of $\xi_L$ will position the cone so that it intersects the target coordinates $x_{\gamma A}$, $y_{\gamma A}$, $z_{\gamma A}$ on the surface of the screen. Considering the triangle formed by the vectors $\vec{V}$, $\vec{R}_L$, and $\vec{E}$, the law of cosines and the quadratic formula may be used to determine $\left|\vec{R}_L\right|$ as

$$\left|\vec{R}_L\right| = \left|\vec{E}\right|\cos\left(\frac{\pi}{2} - \delta\right) + \sqrt{\left|\vec{V}\right|^2 - \left|\vec{E}\right|^2\left[1 - \cos^2\left(\frac{\pi}{2} - \delta\right)\right]} \tag{A21}$$

where

$$\left|\vec{E}\right| = 0.393 \text{ m } (15.5 \text{ in.})$$

$$\delta = 3.32^\circ$$

$$\left|\vec{V}\right| = \sqrt{x_{\gamma A}^2 + y_{\gamma A}^2 + z_{\gamma A}^2}$$

The angle $\chi$ may be determined by again applying the law of cosines to the same triangle, which results in

$$\cos\chi = \frac{\left|\vec{V}\right|^2 + \left|\vec{E}\right|^2 - \left|\vec{R}_L\right|^2}{2\left|\vec{V}\right|\left|\vec{E}\right|} \tag{A22}$$

From the definition of the dot product of two vectors, the following expressions may be written:

$$\vec{V} \cdot \vec{E} = \left(\hat{i}x_{\gamma A} + \hat{j}y_{\gamma A} + \hat{k}z_{\gamma A}\right)\left(-\hat{i}\left|\vec{E}\right|\sin\xi_L + \hat{j}\left|\vec{E}\right|\cos\xi_L\right) \tag{A23}$$

$$\vec{V} \cdot \vec{E} = \left|\vec{V}\right|\left|\vec{E}\right|\cos\chi \tag{A24}$$

Expanding the right side of equation (A23) and setting it equal to equation (A24) gives

$$-x_{\gamma A} \sin \xi_L + y_{\gamma A} \cos \xi_L = |\vec{V}| \cos \chi \tag{A25}$$

To solve for $\sin \xi_L$, equation (A25) is first solved for $y_{\gamma A} \cos \xi_L$ and the resulting equation is squared. After substituting $\cos^2 \xi_L = 1 - \sin^2 \xi_L$, the equation may be solved directly for $\sin \xi_L$:

$$\sin \xi_L = \frac{-x_{\gamma A}|\vec{V}|\cos \chi + y_{\gamma A}\sqrt{x_{\gamma A}^2 + y_{\gamma A}^2 - |\vec{V}|^2 \cos^2 \chi}}{x_{\gamma A}^2 + y_{\gamma A}^2} \tag{A26}$$

By similar reasoning based on equation (A25), $\cos \xi_L$ may be expressed as

$$\cos \xi_L = \frac{y_{\gamma A}|\vec{V}|\cos \chi + x_{\gamma A}\sqrt{x_{\gamma A}^2 + y_{\gamma A}^2 - |\vec{V}|^2 \cos^2 \chi}}{x_{\gamma A}^2 + y_{\gamma A}^2} \tag{A27}$$

The equation for $\dot{\xi}_L$ may be found by differentiating equation (A25) with respect to time. With the proper substitutions for $d|\vec{V}|/dt$ and $\dot{\chi}$, the final result is

$$\dot{\xi}_L = \frac{\left\{\dot{y}_{\gamma A} \cos \xi_L - \dot{x}_{\gamma A} \sin \xi_L + \dfrac{\left(x_{\gamma A}\dot{x}_{\gamma A} + y_{\gamma A}\dot{y}_{\gamma A} + z_{\gamma A}\dot{z}_{\gamma A}\right)\cos\left(\frac{\pi}{2} - \delta\right)}{\sqrt{|\vec{V}|^2 - |\vec{E}|^2\left[1 - \cos^2\left(\frac{\pi}{2} - \delta\right)\right]}}\right\}}{x_{\gamma A} \cos \xi_L + y_{\gamma A} \sin \xi_L} \tag{A28}$$

The elevation mirror command $\eta_L$ is determined as follows. The target coordinates in the $X_\gamma, Y_\gamma, Z_\gamma$ axis system may be transformed to the $X_{em}, Y_{em}, Z_{em}$ axis system (rotating with the elevation mirror) as shown in equation (A29) (see fig. 26):

$$\begin{bmatrix} \left|\vec{R}_L\right| \\ 0 \\ 0 \end{bmatrix} = \begin{bmatrix} \left\{\begin{matrix}\cos\delta\left[\left(x_{\gamma A}\cos\xi_L + y_{\gamma A}\sin\xi_L\right)\cos\eta_L - z_{\gamma A}\sin\eta_L\right] \\ + \sin\delta\left[y_{\gamma A}\cos\xi_L - x_{\gamma A}\sin\xi_L - \left|\vec{E}\right|\right]\end{matrix}\right\} \\ \left\{\begin{matrix}-\sin\delta\left[\left(x_{\gamma A}\cos\xi_L + y_{\gamma A}\sin\xi_L\right)\cos\eta_L - z_{\gamma A}\sin\eta_L\right] \\ + \cos\delta\left[y_{\gamma A}\cos\xi_L - x_{\gamma A}\sin\xi_L - \left|\vec{E}\right|\right]\end{matrix}\right\} \\ \left\{\left(x_{\gamma A}\cos\xi_L + y_{\gamma A}\sin\xi_L\right)\sin\eta_L + z_{\gamma A}\cos\eta_L\right\} \end{bmatrix} \tag{A29}$$

Note that the $X_{em}$-axis is defined as coincident with the projector line of sight $\vec{R}_L$, so that the target position has no coordinates along the $Y_{em}$- or $Z_{em}$-axes. The transformation of equation (A29) is defined by the azimuth rotation $\xi_L$ about the $Z_\gamma$-axis followed by a translation $\left|\vec{E}\right|$ along the $Y'_\gamma$-axis followed by the elevation rotation $\eta_L$ about the $Y'_\gamma$-axis and finally the rotation $\delta$ about the $Z''_\gamma$-axis. Since $\xi_L$ is known from equations (A26) and (A27), $\eta_L$ may be found by solving either the second or third component equation of (A29). The third component is used because of its simplicity and results in

$$\eta_L = \tan^{-1}\left(\frac{-z_{\gamma A}}{x_{\gamma A}\cos\xi_L + y_{\gamma A}\sin\xi_L}\right) \tag{A30}$$

The pitch rate command $\dot{\eta}_L$ is found by differentiating equation (A30) with respect to time:

$$\dot{\eta}_L = \frac{-\dot{z}_{\gamma A}\left(x'_{\gamma A}\cos\xi_L + y_{\gamma A}\sin\xi_L\right) + z_{\gamma A}\left(\dot{x}_{\gamma A}\cos\xi_L + \dot{y}_{\gamma A}\sin\xi_L\right) + z_{\gamma A}\dot{\xi}_L\left(y_{\gamma A}\cos\xi_L - x_{\gamma A}\sin\xi_L\right)}{\left(1 - \cos^2\chi\right)\left(x_{\gamma A}^2 + y_{\gamma A}^2 + z_{\gamma A}^2\right)} \tag{A31}$$

The variable $\left|\vec{R}_L\right|$ from equation (A21) is also used as the input to the servo for the projection zoom-lens focus.

Target-model gimbals.- The relative geometry between the camera and the target model is shown in figure 28. The model is mounted in a four-axis gimbal system and the camera is mounted in the particular position with respect to the model as shown to eliminate occlusion of the model by the pitch gimbal yoke.

The camera is represented by the camera-axis system $X_c, Y_c, Z_c$. This is separated from the projector line-of-sight (LOS) axis system $X_{LP}, Y_{LP}, Z_{LP}$ (as projected back through the TV system from the projection screen) by the angle $\xi_L + \eta_L$. The reason for this is that the target image on the screen rolls about the line of sight when-

ever the target mirrors move in azimuth or elevation. Physically, the roll motion occurs because each mirror rotates about an axis which is not parallel to the reflecting surface. By defining the axis transformation from the LOS axis system to the target body-axis system, the roll coupling is accounted for in the model gimbal motions.

The transformation from line-of-sight axis system to target body-axis system is generated from aircraft dynamics and relative geometry and may be expressed in terms of the transformation matrix $m_{bl}$ as

$$\begin{bmatrix} X_B \\ Y_B \\ Z_B \end{bmatrix} = m_{bl} \begin{bmatrix} X_{LP} \\ Y_{LP} \\ Z_{LP} \end{bmatrix} \tag{A32}$$

In figure 28 the transformation from projector line-of-sight axis system to target body-axis system may be defined in terms of the target-model gimbal angles, the roll decoupling angle $\xi_L + \eta_L$, and the fixed offset angles of the figure as

$$\begin{bmatrix} X_B \\ Y_B \\ Z_B \end{bmatrix} = \left[\phi_m\right]_X \left[\theta_m\right]_Y \left[\psi_m\right]_Z \left[\beta_m\right]_Y \left[\alpha_m\right]_Z \left[60^\circ\right]_Y \left[\xi_L + \eta_L\right]_X \begin{bmatrix} X_{LP} \\ Y_{LP} \\ Z_{LP} \end{bmatrix} \tag{A33}$$

The three inner-gimbal angles $\psi_m$, $\theta_m$, $\phi_m$ may be found by setting equation (A32) equal to equation (A33) and operating with the transpose matrices:

$$\left[\phi_m\right]_X \left[\theta_m\right]_Y \left[\psi_m\right]_Z = m_{bl} \left[\xi_L + \eta_L\right]_X^T \left[60^\circ\right]_Y^T \left[\alpha_m\right]_Z^T \left[\beta_m\right]_Y^T = R \tag{A34}$$

where

$$R = \left[r_{ij}\right] \qquad (i,j = 1, 2, 3)$$

and $\left[\ \right]^T$ denotes the transpose of a matrix.

The logic used to define $\alpha_m$ is the same as that used in the sky-Earth equations:

$$\dot{\alpha}_m = H\left[\operatorname{sgn}\left(-\sin\theta_m \sin\psi_m\right)\left(\left|\theta_m\right| - 60^\circ\right)\right]$$

where $\operatorname{sgn}\left(-\sin\theta_m \sin\psi_m\right)$ is the sign of the product of $-\sin\theta_m$ and $\sin\psi_m$, and

$$H = 0 \qquad \left(\theta_m < 60^\circ\right)$$

$$H = 1 \qquad \left(\theta_m \geqq 60^\circ\right)$$

When the left side of equation (A34) is expanded, the gimbal angles may be defined as

$$\sin\theta_m = -r_{13}$$

$$\cos\theta_m = \sqrt{1 - \sin^2\theta_m}$$

$$\sin\phi_m = \frac{r_{23}}{\cos\theta_m}$$

$$\cos\phi_m = \frac{r_{33}}{\cos\theta_m}$$

$$\sin\psi_m = \frac{r_{12}}{\cos\theta_m}$$

$$\cos\psi_m = \frac{r_{11}}{\cos\theta_m}$$

## Equations for Zoom-Lens Drive

Changes in apparent target range are accomplished by varying the size of the target image on the projection screen in accordance with the computed real-world target range. The math model to accomplish this is based on the following four steps:

(1) The projected image size must be defined in terms of the target model size.

(2) Since the target positioning mirrors are not located at the center of the sphere, the lens-to-screen projection distance $\left|\vec{R}_L\right|$ varies as a function of image position. The resulting variation in image size must be compensated for in the zoom-lens calculations.

(3) After steps (1) and (2) above are complete, the image size must be related to the real-world object size.

(4) Since the camera and projector zoom lenses are driven simultaneously over equal proportional parts of their unequal zoom ranges, then a suitable mixing function between the two zoom drives must be provided.

Definition of the image size in terms of model size is given by the following expression (see fig. 29):

$$Y_1 = M_c M_e M_p Y_m \tag{A35}$$

where

$M_c$ absolute magnification of the camera lens

$M_p$ absolute magnification of the projector lens

$M_e$ electronic magnification which consists of the constant ratio of raster sizes on the projection kinescope and the pickup tube

The variation of image size with varying projection distance is illustrated in figure 30. The reduced image size $Y_1'$ is related to the change in image distance $\left|\vec{R}_L\right|$ as

$$Y_1' = \frac{\left|\vec{R}_L\right|}{R_{Lo}} Y_1 \tag{A36}$$

where $Y_1$ is the image size for the nominal projection distance of $R_{Lo}$.

The projected image size $Y_1'$ may now be related to the real-world target range $R_{BA}$ and target dimension $Y_2$, as shown in figure 31, as

$$Y_1' = R_1 \frac{Y_2}{R_{BA}} \tag{A37}$$

Combining equations (A37) and (A36) results in

$$\frac{\left|\vec{R}_L\right|}{R_{Lo}} Y_1 = \frac{Y_2 R_1}{R_{BA}} \tag{A38}$$

Substituting equation (A35) in equation (A38) gives

$$\frac{\left|\vec{R}_L\right|}{R_{Lo}} M_c M_e M_p = \frac{Y_2}{Y_m} \frac{R_1}{R_{BA}} \tag{A39}$$

Equation (A39) expresses the overall system magnification in terms of two variables: real-world range $R_{BA}$ and varying projection distance $\left|\vec{R}_L\right|$. Variations in the left side of equation (A39) due to changes in $\left|\vec{R}_L\right|$ are compensated for by changes in $M_c M_e M_p$, so that for a given value of $R_{BA}$, the ratio $\frac{\left|\vec{R}_L\right|}{R_{Lo}} M_c M_e M_p$ remains constant.

The changes in $M_c M_e M_p$ are accomplished by simultaneously driving the camera and projection zoom lenses over their respective unequal displacements. This is controlled by a mixing function which will be described later in more detail. Equation (A39) can now be solved for $M_c M_e M_p$ as

$$M_c M_e M_p = \frac{Y_2}{Y_m} \frac{R_1}{R_{BA}} \frac{R_{Lo}}{\left|\vec{R}_L\right|} \tag{A40}$$

The ratio $Y_2/Y_m$ is the model scale factor and will be defined as $S_f$. Therefore, equation (A40) becomes:

$$M_c M_p = \frac{S_f R_1 R_{Lo}}{M_e} \frac{1}{R_{BA}\left|\vec{R}_L\right|} \tag{A41}$$

Equation (A41) is written in terms of absolute magnifications $M_c$, $M_p$, and $M_e$. The absolute magnification of the projector zoom lens was established during initial (subcontract) acceptance tests at the vendor's plant with a measured maximum value for the two lenses of $\times$ 10. Absolute magnification of the camera lenses was never documented, since calibration was performed with the TV camera and monitor and resulting data were expressed in terms of relative magnification $M_c'$, which varies from approximately $\times$ 1 to $\times$ 16. Electronic magnification $M_e$ is the ratio of the projection-tube raster size to the camera raster size, and its absolute value is approximately 4.0. This is the only adjustable component of $M_c M_e M_p$ and is normally adjusted on a daily basis to maintain proper total magnification.

Since the original camera-lens data were given in terms of $M_c'$, the equation actually employed for the interface computations in the central computer is of the form

$$M_c' M_p = \frac{S_f R_1}{K M_e} \frac{R_{Lo}}{\left|\vec{R}_L\right|} \frac{1}{R_{BA}} \tag{A42}$$

where

$$M_c = K M_c'$$

and $K$ is a constant of proportionality.

The numerical coefficient $S_f R_1 / K M_e$ can be derived from equation (A42) by substituting the following consistent set of conditions:

$$\left|\vec{R}_L\right| = R_{Lo}$$

$$R_{BA} = 92 \text{ m } (300 \text{ ft})$$

$$M_c' = \left(M_c'\right)_{max} = 16$$

$$M_p = \left(M_p\right)_{max} = 10$$

Substitution of these values in equation (A42) gives

$$\frac{S_f R_1}{K M_e} = 14.63 \text{ km } (48\ 000 \text{ ft})$$

It should be noted that

(a) Small changes in model scale factor can be accommodated by a proportionate change in $M_e$ (i.e., maintaining the same ratio $S_f / M_e$ without changing the numerical value of the coefficient in the computer program). The amount of change is limited for large models by the maximum field angle of the camera lens, and for small models by video-optical resolution limits. (That is, large values of $M_e$ can be obtained by using a very small vidicon raster, but this is not advisable.)

(b) Changes in $S_f$, accomplished by a proportionate change in $M_e$ with no change in the computer program, result in the same minimum range (i.e., zoom-lens magnifications $M_c' M_p = 160$, or maximum, at 92 m (300 ft)).

(c) A change in model scale factor $S_f$ with no changes in nominal raster sizes $M_e$ can result in a different minimum range, but the coefficient in the com-

puter program must be changed accordingly. For example, use of a larger model (for instance $S_f = 96:1$ versus 120:1) and a change in the computer program coefficient

$$M_c' M_p = \frac{96}{120}(14.63)\frac{R_{Lo}}{\left|\vec{R}_L\right|}\frac{1}{R_{BA}}$$

yield the desired maximum value of relative magnification $\left(M_c' M_p = 160\right)$ when $R_{BA} = R_{min} = \frac{96}{120} \times 92 = 73.6$ m (240 ft).

The mixing function which was previously mentioned is an experimentally derived function which causes both lenses to be driven through equal proportional parts of their unequal zoom ranges for a given change in target range or image throw distance. The function is given by

$$M_p = 0.18 + \left(M_c'\right)^{0.82389} \tag{A43}$$

Equation (A43) is based on a range of × 1.18 to × 10 in $M_p$ and × 1 to × 16 in $M_c'$. Definition of $M_c$ on an absolute basis rather than relative (as stated above) would require a modification of the mixing function. Substitution of equation (A42) in equation (A43) results in

$$0.18M_c' + \left(M_c'\right)^{1.82389} = \frac{S_f R_1 R_{Lo}}{KM_e}\frac{1}{R_{BA}\left|\vec{R}_L\right|} \tag{A44}$$

Equations (A43) and (A44) are programed on the computer. The input voltages for the zoom servo positions are not linear functions of $M_c'$ and $M_p$. Therefore, experimentally determined nonlinear functions are programed to provide the correct servo position commands $x_l$ and $x_m$ as a function of $M_c'$ and $M_p$.

## Projection Geometry

The projection geometry described in the body of this report provides quantitative means to study the observed motion of any point in the sky-Earth display and/or the target display. This was done by developing an exact geometrical model relating the observer's line of sight to the projected image points of the sky-Earth and target displays.

Sky-Earth projection geometry.- The sky-scene projection geometry is illustrated in figure 32. (A similar figure and analysis would be applicable to the Earth transpar-

ency.) The location of the projected image point on the sphere is defined by the vector $\vec{V}_O$ which is defined in the $X_A, Y_A, Z_A$ axis system as

$$\vec{V}_O = \vec{N} + \vec{A} \tag{A45}$$

The first term on the right side of equation (A45) is defined as

$$\vec{N} = \vec{S} + \vec{V}_{TCS} + \vec{V}_A \tag{A46}$$

where

$\vec{S}$ constant vector between the sky-Earth gimbal center and the center of the projection screen

$\vec{V}_{TCS}$ vector defining the position of the moving transparency center relative to the fixed gimbal center

$\vec{V}_A$ vector defining the position of a point on the transparency relative to the transparency center

In the axis system $X_T, Y_T, Z_T$ rotating with the pitch gimbal and with its origin at the gimbal center, the second and third terms on the right side of equation (A46) are defined as

$$\vec{V}_{TCS} + \vec{V}_A = \begin{bmatrix} 0 \\ 0 \\ \left|\vec{V}_{TCS}\right| \end{bmatrix} + R_2 \begin{bmatrix} \cos\theta_B \cos\left[-\left(\psi_B + \psi_G\right)\right] \\ \cos\theta_B \sin\left[-\left(\psi_B + \psi_G\right)\right] \\ \sin\left(-\theta_B\right) \end{bmatrix} \tag{A47}$$

After transforming equation (A47) to the nonrotating axis system, equation (A46), which is also in the nonrotating axis system, becomes

$$\vec{N} = \begin{bmatrix} N_x \\ N_y \\ N_z \end{bmatrix} = \begin{bmatrix} S_x \\ 0 \\ S_z \end{bmatrix} + T_G^T \begin{bmatrix} R_2 \cos\theta_B \cos\left(\psi_B + \psi_G\right) \\ -R_2 \cos\theta_B \sin\left(\psi_B + \psi_G\right) \\ -R_2 \sin\theta_B - \left|\vec{V}_{TCS}\right| \end{bmatrix} \tag{A48}$$

where $T_G$, which is the transformation from the $X_A, Y_A, Z_A$ axis system to the $X_T, Y_T, Z_T$ axis system, is given by

$$T_G = [\theta_G]_Y [\phi_G]_X [\beta_G]_Y [\alpha_G]_X \tag{A49}$$

The angles $\alpha_G$, $\phi_G$, and $\theta_G$ are the gimbal angles as read from the linear potentiometers mounted on the gimbals.

The vector $\vec{A}$ may be defined as follows:

$$\vec{A} = \begin{bmatrix} A_x \\ A_y \\ A_z \end{bmatrix} = |\vec{A}| \frac{\vec{v}_p}{|\vec{v}_p|} = \frac{|\vec{A}|}{|\vec{v}_p|} \begin{bmatrix} v_{px} \\ v_{py} \\ v_{pz} \end{bmatrix} \tag{A50}$$

where $|\vec{A}|$ may be determined by applying the law of cosines to the triangle defined by vectors $\vec{N}$, $\vec{A}$, and $\vec{V}_o$, which results in

$$|\vec{A}| = -\frac{\vec{N} \cdot \vec{v}_p}{|\vec{v}_p|} + \sqrt{\left(\frac{\vec{N} \cdot \vec{v}_p}{|\vec{v}_p|}\right)^2 - |\vec{N}|^2 + |\vec{V}_o|^2} \tag{A51}$$

The vector $\vec{v}_p$ in equations (A50) and (A51) is defined as follows:

$$\vec{v}_p = \vec{N} - \vec{V}_L \tag{A52}$$

Upon substitution for $\vec{N}$ from equation (A46) and $\vec{V}_L$ where $\vec{V}_L = \vec{S} + \vec{b}_o' + \vec{L}_C$, equation (A52) becomes

$$\vec{v}_p = \vec{V}_A - \vec{b}_o' + \vec{V}_{TCS} - \vec{L}_C \tag{A53}$$

The vector sum $\vec{V}_A + \vec{V}_{TCS}$ was defined in the rotating axis system by equation (A47). In the rotating system $\vec{L}_C$ is a constant given by

$$\vec{L}_C = \begin{bmatrix} 0 \\ 0 \\ \left|\vec{V}_{TCS}\right| + 1.47 \end{bmatrix} \tag{A54}$$

where $\left|\vec{V}_{TCS}\right| + 1.47$ cm (0.58 in.) is the distance from the lamp to the center of the lamp support arm. Substituting $b'_{ox}$, $b'_{oy}$, $b'_{oz}$, which are the components of $\vec{b}'_o$, and equations (A54) and (A47) into equation (A53) and transforming the result to the nonrotating axis system results in the following expression for $\vec{v}_p$:

$$\vec{v}_p = T_G^T \begin{bmatrix} R_2 \cos\theta_B \cos\left[-\left(\psi_B + \psi_G\right)\right] - b'_{ox} \\ R_2 \cos\theta_B \sin\left[-\left(\psi_B + \psi_G\right)\right] - b'_{ox} \\ R_2 \sin\left(-\theta_B\right) - b'_{oz} + 1.47 \end{bmatrix} \tag{A55}$$

Substitution of equations (A55) and (A51) into (A50) gives the value for $\vec{A}$. Now that $\vec{N}$ and $\vec{A}$ have been determined, the value of $\vec{V}_o$ may be found by equation (A45) which is repeated here for reference:

$$\vec{V}_o = \vec{N} + \vec{A}$$

Target-image projection geometry.- The target-image projection geometry is illustrated in figure 33. The location of the projected target image is defined by the vector $\vec{B}$ in the $X_A, Y_A, Z_A$ nonrotating axis system:

$$\vec{B} = \vec{D} + \vec{E} + \vec{V}_t \tag{A56}$$

where $\vec{D}$ is a constant vector between the center of the azimuth mirror and the center of the projection screen.

The vector $\vec{E}$ defines the position of the center of the elevation mirror with respect to the center of the azimuth mirror gimbal and is defined in the $X'_A, Y'_A, Z'_A$ axis system as

$$\vec{E} = \left|\vec{E}\right| \begin{bmatrix} -\sin\xi'_L \cos\gamma \\ \cos\xi'_L \\ \sin\xi'_L \sin\gamma \end{bmatrix} \tag{A57}$$

where $\xi'_L$ is the actual azimuth gimbal position as read from the linear potentiometer and $\gamma$ is the constant tilt angle of the entire target projection system with respect to the horizontal plane of the projection sphere.

The vector $\vec{V}_t$ is defined as

$$\vec{V}_t = \left|\vec{V}_t\right| \begin{bmatrix} v_{tx} \\ v_{ty} \\ v_{tz} \end{bmatrix} \tag{A58}$$

where $\hat{v}_t$ is a unit vector along the projected line of sight:

$$\hat{v}_t = \begin{bmatrix} v_{tx} \\ v_{ty} \\ v_{tz} \end{bmatrix} = \begin{bmatrix} \cos\gamma \cos\xi'_L \cos\eta'_L - \sin\gamma \sin\eta'_L \\ \sin\xi'_L \cos\eta'_L \\ -\sin\gamma \cos\xi'_L \cos\eta'_L - \cos\gamma \sin\eta'_L \end{bmatrix} \tag{A59}$$

The quantity $\left|\vec{V}_t\right|$ is found by applying the law of cosines to the triangle formed by the vectors $\vec{V}_{em}$, $\vec{B}$, and $\vec{V}_t$

$$\left|\vec{V}_t\right| = -\left(\vec{V}_{em} \cdot \hat{v}_t\right) + \sqrt{\left(\vec{V}_{em} \cdot \hat{v}_t\right)^2 + \left|\vec{B}\right|^2 - \left|\vec{V}_{em}\right|^2} \tag{A60}$$

where

$$\vec{V}_{em} = \vec{D} + \vec{E}$$

Now that $\vec{E}$ and $\vec{V}_t$ have been determined, the value of $\vec{B}$ may be found from equation (A56).

## APPENDIX B

## COCKPIT ACTIVE INSTRUMENTS

Airspeed/Mach indicator:

The needle indicates airspeed and the inner dial indicates Mach number as follows:

Range of scales:

Airspeed – 50 knots to 1600 knots for $300^{\circ}$ of needle rotation

Mach number – 0.5 M to 3.5 M

Scale resolution:

Airspeed –

50 to 300 knots: 5 knots/div and 50 div/$100^{\circ}$ of needle rotation

300 to 600 knots: 20 knots/div and 15 div/$75^{\circ}$ of needle rotation

600 to 1600 knots: 50 knots/div and 20 div/$125^{\circ}$ of needle rotation

Mach number –

0.05 Mach/div: 60 div/$300^{\circ}$ of dial rotation

Total accuracy:

Airspeed –

5 knots over the range of 50 to 300 knots

10 knots over the range of 300 to 600 knots

25 knots over the range of 600 to 1600 knots

Mach number – 0.04 Mach

Three-axis 8 ball attitude indicator with the following auxiliary indicators:

Horizontal and vertical needles, displacement pointer (vertical), rate-of-turn indicator, warning flags, and inclinometer

Range: Continuous in/out view

Scale resolution: Standard per MIL-I-27619D

Total accuracy: 1%

Electrical resolution: 0.5%

Altimeter (3-needle):

Range: 0 to 100 000 ft

Scale resolution:

Long needle – 1000 ft/rev, 20 ft/div

Med needle – 10 000 ft/rev, 200 ft/div

Short needle – 100 000 ft/rev, 2000 ft/div

Total accuracy: 0.2% of altitude or 50 ft, whichever is greater

Vertical velocity (2-needle):

Range: 0 to ±30 000 ft/min

Scale resolution:

Outer scale – 0 to 6000 ft/min (nonlinear through ±165°)

Inner scale – 0 to 30 000 ft/min, 5000 ft/div, 6 div/165° of rotation

Control position trim:

Total accuracy: 2%

Fuel flow pointer:

Range: 500 to 15 000 lb/hr for 240° rotation

Scale resolution: 400 to 15 000 lb/hr, 500 lb/hr/div, 30 div/240° of rotation

Total accuracy: 150 lb/hr

Fuel quantity:

Range: 0 to 24 000 lb

Scale resolution: 500 lb/div and 48 div/250° of rotation

Total accuracy: 300 lb

Flap position (2-needle):

Range: 0 to 100° of rotation

Scale resolution: 15° flap/div and 8 div/110° of rotation

Total accuracy: 5°

Speed brake (2-needle):

Range: 0 to 100° of rotation

Scale resolution: 1/3 brake/div and 3 div/110° of rotation

Total accuracy: 1/12 of brake (9°12')

Accelerometer:

Range: -5 to +10g

Scale resolution: 0.5g/div, 30 div/250° of rotation, 0° equals -0.5g

Total accuracy: 0.2g

Angle of attack:

Range: 0 to ±45°

Scale resolution: 1°/div and ±45 div/125° of rotation

Total accuracy: 1°

Tachometer (2-needle):

Range: 0 to 120% rpm

Scale resolution:

Coarse needle – 5% rpm/div and 24 div/280° of rotation

Fine needle – 1% rpm/div and 10 div/360° of rotation

Total accuracy: 2%

Exhaust pressure ratio:

Range: 1.2 to 3.4

Scale resolution: 0.1 EPR/div and 22 div/250° of rotation

Total accuracy: 0.10 EPR

Exhaust gas temperature:

Range: 0 to 1500° C

Scale resolution: 30° C/div and 50 div/250° of rotation

Total accuracy: 30° C

Oil pressure:

Range: 0 to 100 psi

Scale resolution: 5 psi/div and 20 div/250° of rotation

Total accuracy: 2 psi

True airspeed counter:

Range: 0 to 2000 knots

Scale resolution: 2 knots/Count

Total accuracy: 25 knots

Exhaust nozzle position:

Range: 0 to 15°

Scale resolution: 5°/div and 3 div/110° of rotation

Total accuracy: 2°

Dual throttle quadrant with flap and speed brake controls:

Range: Flaps – Leading edge/trailing edge brakes – front, rear

## APPENDIX C

## CONTROL-LOADER CHARACTERISTICS

(1) Maximum travel (hard stops) – maximum provided is adjustable within maximum range below:

(a) Pitch – 0.3048 m (12 in.) (can be set up asymmetrically)

(b) Roll – from 0 to ±0.1778 m (7 in.)

(c) Yaw – from 0 to ±0.08255 m (3.25 in.)

(2) Force versus displacement gradients – two gradient cards per axis are available, each has four slope segments in each direction for nonlinear gradient generation (excludes any nonlinear gradients due to aerodynamics.

(3) Static friction – adjustable range of 0 to 44.5 N (10 lb) provided.

(4) Viscous frictions – related to damping ratio – a range of 0.2 to over critical damped is provided.

(5) Breakout force – a range of 0 to 111 N (25 lb) breakout is provided.

(6) Deadband ("slop") – a range of 0 to 70% of maximum travel is provided.

(7) Trim rate – a range of 0 to 0.0508 m/sec (2 in./sec) is provided in pitch and roll axes. No trim is provided for yaw.

(8) External forces – stick or pedal force changes due to aerodynamic effects, bob weights, and so forth have to be programed in central computing and drive the loader systems as a separate command.

## APPENDIX D

## DERIVATION OF THE SERVO TIME LAG

The closed-loop transfer function of the servo is defined as

$$G_S = \frac{(25)^2 G_i}{S^2 + 2(0.707)(25)S + (25)^2}$$

where $G_i$ is the generalized servo input, $G_S$ is the generalized servo output, and $S$ is the Laplace operator. The transfer function of a velocity input is

$$G_i = \frac{V}{S^2}$$

where $V$ is the amplitude of the velocity input (a constant). The position error $\epsilon$ between the velocity command and the second-order servo subjected to the velocity command may be written as

$$G_i - G_S = \epsilon = \frac{V}{S^2} - \frac{(25)^2(V/S^2)}{S^2 + 2(0.707)(25)S + (25)^2}$$

or

$$\frac{\epsilon}{V} = \frac{1}{S^2} - \frac{(25)^2}{S^2\left[S^2 + (35.35)S + (25)^2\right]}$$

By referring to figure 17 it can be seen that the error $\epsilon$ in radians divided by the constant velocity $V$ in rad/sec yields the time lag $T$:

$$T = \frac{\epsilon}{V} = \frac{S^2 + (35.35)S + (25)^2 - (25)^2}{S^2\left[S^2 + (35.35)S + (25)^2\right]}$$

Now the final-value theorem is applied to get the steady-state time lag:

$$T = \lim_{t \to \infty} \frac{\epsilon}{V}(t) = \lim_{S \to 0} S \frac{\epsilon}{V}(S)$$

$$T = \lim_{S \to 0} S \frac{S^2 + (35.35)S}{S^2\left[S^2 + (35.35)S + (25)^2\right]}$$

$$T = \lim_{S \to 0} \frac{S + 35.35}{S^2 + (35.35)S + (25)^2} = \frac{35.35}{(25)^2} = 56.6 \text{ msec}$$

## REFERENCES


1. Copeland, J. L.; Kahlbaum, W. M., Jr.; Barker, L. E., Jr.; Steinmetz, G. G.; and Grove, R. D.: Design of a Dual Wide-Angle Visual Cue Simulator. J. Aircraft, vol. 8, no. 5, May 1971, pp. 374-380.

2. Wilson, John W.: Analysis and Mechanization of Three- and Four-Gimbal Systems. NASA TN D-4689, 1968.

3. Mitchell, E. E. L.; and Rogers, A. E.: Quaternion Parameters in the Simulation of a Spinning Rigid Body. Simulation, vol. 4, no. 6, June 1965, pp. 390-396.

4. Robinson, Alfred C.: On the Use of Quaternions in Simulation of Rigid-Body Motion. WADC Tech. Rep. 58-17, U.S. Air Force, Dec. 1958. (Available from DDC as AD 234 422.)

5. Goldstein, Herbert: Classical Mechanics. Addison-Wesley Pub. Co., Inc., c.1950.

TABLE I.- NO-LOAD VELOCITIES AND STALL ACCELERATIONS

| Servo driven by | No-load velocity | | | | | | Stall acceleration | | | | | |
|---|---|---|---|---|---|---|---|---|---|---|---|---|
| | Desired | | Actual system A | | Actual system B | | Desired | | Actual system A | | Actual system B | |
| | rad/sec | | rad/sec | | rad/sec | | rad/sec$^2$ | | rad/sec$^2$ | | rad/sec$^2$ | |
| $\theta_E$ | 3.0 | | 3.60 | | 3.40 | | 42.5 | | 73.0 | | 45.9 | |
| $\alpha_E$ | 10.0 | | 9.10 | | 9.60 | | 63.5 | | 70.0 | | 64.0 | |
| $\phi_E$ | 10.0 | | 9.05 | | 9.75 | | 108.0 | | 195.0 | | 146.0 | |
| $\psi_E$ | 10.0 | | 11.30 | | 11.60 | | 100.0 | | 119.0 | | 102.5 | |
| $\eta_L$ | 10.0 | | 10.80 | | 11.85 | | 33.8 | | 43.0 | | 44.8 | |
| $\xi_L$ | 10.0 | | 9.60 | | 9.65 | | 30.9 | | 29.2 | | 27.4 | |
| $\alpha_m$ | 10.0 | | 11.80 | | 11.80 | | 79.5 | | 71.0 | | 70.0 | |
| $\psi_m$ | 10.0 | | 9.20 | | 9.25 | | 108.0 | | 111.5 | | 107.5 | |
| $\phi_m$ | 10.0 | | 11.80 | | 11.65 | | 100.0 | | 175.0 | | 171.0 | |
| $\theta_m$ | 6.0 | | 9.30 | | 9.30 | | 100.0 | | 127.0 | | 130.0 | |
| | m/sec | in./sec | m/sec | in./sec | m/sec | in./sec | m/sec$^2$ | in./sec$^2$ | m/sec$^2$ | in./sec$^2$ | m/sec$^2$ | in./sec$^2$ |
| $b_{ox}$ | 0.889 | 35.0 | 0.958 | 37.7 | 0.975 | 38.35 | 9.60 | 378.0 | 12.7 | 495.0 | 13.6 | 535.0 |
| $b_{oy}$ | .889 | 35.0 | .930 | 36.6 | .914 | 36.0 | 11.2 | 439.0 | 12.3 | 484.0 | 12.1 | 475.0 |
| $b_{oz}$ | .889 | 35.0 | .945 | 37.2 | .937 | 36.9 | 8.74 | 344.0 | 11.2 | 439.0 | 12.3 | 486.0 |
| $x_l$ | .100 | 3.94 | .130 | 5.1 | .133 | 5.25 | 1.00 | 39.4 | 2.07 | 81.5 | 2.14 | 84.2 |
| | deg/sec | | deg/sec | | deg/sec | | deg/sec$^2$ | | deg/sec$^2$ | | deg/sec$^2$ | |
| $x_m$ | 82.5 | | 128.0 | | 136.0 | | 1860.0 | | 3100.0 | | 4995.0 | |
| $R_F$ | (a) | | 153.0 | | 225.0 | | 2430.0 | | 3250.0 | | 4440.0 | |

[a]Servo was required to track at 31 deg/sec with less than 0.5° error, which was achieved.

TABLE II.- SERVO COMPLIANCES

| Servo driven by | Static compliance | | | | | | Dynamic compliance | | | | | |
|---|---|---|---|---|---|---|---|---|---|---|---|---|
| | Desired | | Actual system A | | Actual system B | | Desired | | Actual system A | | Actual system B | |
| | rad/m-N | rad/in-lb | rad/m-N | rad/in-lb | rad/m-N | rad/in-lb | rad/m-N | rad/in-lb | rad/m-N | rad/in-lb | rad/m-N | rad/in-lb |
| $\theta_E$ | $2.8 \times 10^{-4}$ | $3.2 \times 10^{-5}$ | $1.02 \times 10^{-5}$ | $1.15 \times 10^{-6}$ | $6.68 \times 10^{-5}$ | $7.55 \times 10^{-6}$ | $5.66 \times 10^{-4}$ | $6.4 \times 10^{-5}$ | $8.85 \times 10^{-5}$ | $1.0 \times 10^{-5}$ | $1.02 \times 10^{-4}$ | $1.15 \times 10^{-5}$ |
| $\alpha_E$ | $7.88 \times 10^{-5}$ | $8.9 \times 10^{-6}$ | $7.81 \times 10^{-8}$ | $8.82 \times 10^{-9}$ | $1.56 \times 10^{-7}$ | $1.76 \times 10^{-8}$ | $1.58 \times 10^{-4}$ | $1.78 \times 10^{-5}$ | $1.09 \times 10^{-4}$ | $1.23 \times 10^{-5}$ | $1.68 \times 10^{-5}$ | $1.9 \times 10^{-6}$ |
| $\phi_E$ | $1.42 \times 10^{-5}$ | $1.6 \times 10^{-6}$ | 0 | 0 | $3.89 \times 10^{-8}$ | $4.4 \times 10^{-9}$ | $2.83 \times 10^{-5}$ | $3.2 \times 10^{-6}$ | $2.11 \times 10^{-5}$ | $2.38 \times 10^{-6}$ | $2.18 \times 10^{-5}$ | $2.46 \times 10^{-6}$ |
| $\psi_E$ | $1.86 \times 10^{-6}$ | $2.1 \times 10^{-4}$ | $4.82 \times 10^{-5}$ | $5.45 \times 10^{-6}$ | $3.20 \times 10^{-4}$ | $3.62 \times 10^{-5}$ | $3.72 \times 10^{-3}$ | $4.2 \times 10^{-4}$ | $5.48 \times 10^{-4}$ | $6.2 \times 10^{-5}$ | $5.66 \times 10^{-4}$ | $6.4 \times 10^{-5}$ |
| $\eta_L$ | $2.48 \times 10^{-2}$ | $2.8 \times 10^{-3}$ | $6.73 \times 10^{-4}$ | $7.61 \times 10^{-5}$ | $3.03 \times 10^{-3}$ | $3.42 \times 10^{-4}$ | $4.95 \times 10^{-2}$ | $5.6 \times 10^{-3}$ | $2.42 \times 10^{-4}$ | $2.74 \times 10^{-4}$ | $4.43 \times 10^{-3}$ | $5.0 \times 10^{-4}$ |
| $\xi_L$ | $1.06 \times 10^{-3}$ | $1.2 \times 10^{-4}$ | $4.21 \times 10^{-4}$ | $4.76 \times 10^{-5}$ | $3.63 \times 10^{-5}$ | $4.1 \times 10^{-6}$ | $2.12 \times 10^{-3}$ | $2.4 \times 10^{-4}$ | $8.14 \times 10^{-4}$ | $9.2 \times 10^{-5}$ | $6.99 \times 10^{-4}$ | $7.9 \times 10^{-5}$ |
| $\alpha_m$ | $1.59 \times 10^{-3}$ | $1.8 \times 10^{-4}$ | $2.00 \times 10^{-4}$ | $2.26 \times 10^{-5}$ | $1.51 \times 10^{-5}$ | $1.71 \times 10^{-6}$ | $3.19 \times 10^{-3}$ | $3.6 \times 10^{-4}$ | $7.0 \times 10^{-4}$ | $7.9 \times 10^{-5}$ | $6.63 \times 10^{-4}$ | $7.5 \times 10^{-5}$ |
| $\psi_m$ | $1.85 \times 10^{-3}$ | $2.1 \times 10^{-4}$ | $1.44 \times 10^{-4}$ | $1.63 \times 10^{-5}$ | 0 | 0 | $3.72 \times 10^{-3}$ | $4.2 \times 10^{-4}$ | $8.85 \times 10^{-4}$ | $1.0 \times 10^{-4}$ | $7.7 \times 10^{-4}$ | $8.7 \times 10^{-5}$ |
| $\phi_m$ | $2.6 \times 10^{-1}$ | $3.0 \times 10^{-2}$ | $1.73 \times 10^{-3}$ | $1.95 \times 10^{-4}$ | $8.44 \times 10^{-3}$ | $9.54 \times 10^{-4}$ | $5.3 \times 10^{-1}$ | $6.0 \times 10^{-2}$ | $1.59 \times 10^{-3}$ | $1.8 \times 10^{-4}$ | $1.62 \times 10^{-2}$ | $1.83 \times 10^{-3}$ |
| $\theta_m$ | $1.24 \times 10^{-1}$ | $1.4 \times 10^{-2}$ | $1.78 \times 10^{-3}$ | $2.0 \times 10^{-4}$ | $4.27 \times 10^{-3}$ | $4.83 \times 10^{-4}$ | $2.48 \times 10^{-1}$ | $2.8 \times 10^{-2}$ | $6.02 \times 10^{-5}$ | $6.8 \times 10^{-6}$ | $1.48 \times 10^{-3}$ | $1.67 \times 10^{-4}$ |
| $x_m$ | $1.24 \times 10^{-2}$ | $1.4 \times 10^{-3}$ | 0 | 0 | 0 | 0 | $2.48 \times 10^{-2}$ | $2.8 \times 10^{-3}$ | $3.36 \times 10^{-3}$ | $3.8 \times 10^{-4}$ | $8.85 \times 10^{-4}$ | $1.0 \times 10^{-4}$ |
| | m/N | in./lb | m/N | in./lb | m/N | in./lb | m/N | in./lb | m/N | in./lb | m/N | in./lb |
| $b_{ox}$ | $5.14 \times 10^{-5}$ | $9.0 \times 10^{-3}$ | 0 | 0 | 0 | 0 | $1.03 \times 10^{-4}$ | $1.8 \times 10^{-2}$ | $5.48 \times 10^{-6}$ | $9.6 \times 10^{-4}$ | $6.0 \times 10^{-6}$ | $1.05 \times 10^{-3}$ |
| $b_{oy}$ | $6.28 \times 10^{-5}$ | $1.1 \times 10^{-2}$ | 0 | 0 | 0 | 0 | $1.26 \times 10^{-4}$ | $2.2 \times 10^{-2}$ | $6.85 \times 10^{-6}$ | $1.2 \times 10^{-3}$ | $5.88 \times 10^{-6}$ | $1.03 \times 10^{-3}$ |
| $b_{oz}$ | $1.31 \times 10^{-4}$ | $2.3 \times 10^{-2}$ | 0 | 0 | $1.42 \times 10^{-6}$ | $2.48 \times 10^{-4}$ | $2.63 \times 10^{-4}$ | $4.6 \times 10^{-2}$ | $1.48 \times 10^{-5}$ | $2.6 \times 10^{-3}$ | $1.63 \times 10^{-5}$ | $2.86 \times 10^{-3}$ |
| $x_l$ | $1.94 \times 10^{-6}$ | $3.4 \times 10^{-4}$ | 0 | 0 | 0 | 0 | $3.88 \times 10^{-6}$ | $6.8 \times 10^{-4}$ | $2.91 \times 10^{-7}$ | $5.1 \times 10^{-5}$ | $1.02 \times 10^{-6}$ | $1.79 \times 10^{-4}$ |

TABLE III.- SERVO LOW-VELOCITY SMOOTHNESS

| Servo driven by | Output velocity | | Deviation, system A | | Deviation, system B | |
|---|---|---|---|---|---|---|
| | rad/sec | | rad/sec | | rad/sec | |
| $\theta_E$ | ±0.015 | | ±0.0024 | | ±0.0024 | |
| $\alpha_E$ | ±.05 | | ±.0042 | | ±.0050 | |
| $\phi_E$ | ±.05 | | ±.0072 | | ±.0028 | |
| $\psi_E$ | ±.05 | | ±.0017 | | ±.0016 | |
| $\eta_L$ | ±.05 | | ±.0026 | | ±.0038 | |
| $\xi_L$ | ±.05 | | ±.0049 | | ±.0012 | |
| $\alpha_m$ | ±.05 | | ±.0047 | | ±.0047 | |
| $\psi_m$ | ±.05 | | ±.0056 | | ±.0076 | |
| $\phi_m$ | ±.05 | | ±.0219 | | ±.0062 | |
| $\theta_m$ | ±.03 | | ±.0125 | | ±.0087 | |
| $x_m$ | ±.0175 | | ±.0032 | | ±.0043 | |
| | m/sec | in./sec | m/sec | in./sec | m/sec | in./sec |
| $b_{ox}$ | ±0.00445 | ±0.175 | ±0.000869 | ±0.0342 | ±0.000904 | ±0.0356 |
| $b_{oy}$ | ±.00445 | ±.175 | ±.000445 | ±.0175 | ±.000444 | ±.0175 |
| $b_{oz}$ | ±.00445 | ±.175 | ±.000853 | ±.0336 | ±.000361 | ±.0142 |
| $x_l$ | ±.0005 | ±.02 | ±.000163 | ±.0064 | ±.000097 | ±.0038 |

TABLE IV.- STEADY-STATE TIME LAGS

| Servo driven by | Time lag, msec, for – | |
|---|---|---|
| | System A | System B |
| $\theta_E$ | 53 | 53 |
| $\alpha_E$ | 58 | 65 |
| $\phi_E$ | 64 | 58 |
| $\psi_E$ | 60 | 62 |
| $\eta_L$ | 62 | 44 |
| $\xi_L$ | 56 | 62 |
| $\alpha_m$ | 52 | 50 |
| $\psi_m$ | 52 | 56 |
| $\phi_m$ | 60 | 60 |
| $\theta_m$ | 50 | 47 |
| $b_{ox}$ | 54 | 52 |
| $b_{oy}$ | 51 | 50 |
| $b_{oz}$ | 52 | 54 |
| $x_l$ | 47 | 43 |
| $x_m$ | 10 | 10 |

TABLE V.- SERVO TRANSIENT RESPONSE

| Servo driven by | Velocity amplitude for – | | | | Deviation, system A, for – | | | | Deviation, system B, for – | | | |
|---|---|---|---|---|---|---|---|---|---|---|---|---|
| | 20% step | | 1% step | | 20% step | | 1% step | | 20% step | | 1% step | |
| | rad/sec | | rad/sec | | rad/sec | | rad/sec | | rad/sec | | rad/sec | |
| $\theta_E$ | 0.6 | | 0.03 | | ±0.05 | | ±0.004 | | ±0.08 | | ±0.008 | |
| $\alpha_E$ | 2.0 | | .10 | | ±.28 | | ±.037 | | ±.37 | | ±.022 | |
| $\phi_E$ | 2.0 | | .10 | | ±.36 | | ±.022 | | ±.16 | | ±.048 | |
| $\psi_E$ | 2.0 | | .10 | | ±.12 | | ±.010 | | ±.08 | | ±.015 | |
| $\eta_L$ | 2.0 | | .10 | | ±.10 | | ±.016 | | ±.07 | | ±.019 | |
| $\xi_L$ | 2.0 | | .10 | | ±.29 | | ±.022 | | ±.30 | | ±.011 | |
| $\alpha_m$ | 2.0 | | .10 | | ±.12 | | ±.017 | | ±.12 | | ±.012 | |
| $\psi_m$ | 2.0 | | .10 | | ±.21 | | ±.022 | | ±.15 | | ±.018 | |
| $\phi_m$ | 2.0 | | .10 | | ±.50 | | ±.15 | | ±.37 | | ±.120 | |
| $\theta_m$ | 1.2 | | .06 | | ±.20 | | ±.021 | | ±.13 | | ±.025 | |
| $x_m$ | .7 | | .035 | | ±.07 | | ±.032 | | ±.05 | | ±.015 | |
| | m/sec | in./sec | m/sec | in./sec | m/sec | in./sec | m/sec | in./sec | m/sec | in./sec | m/sec | in./sec |
| $b_{ox}$ | 0.18 | 7.0 | 0.0089 | 0.35 | ±0.010 | ±0.39 | ±0.0022 | ±0.086 | ±0.011 | ±0.42 | ±0.0019 | ±0.073 |
| $b_{oy}$ | .18 | 7.0 | .0089 | .35 | ±.017 | ±.66 | ±.0010 | ±.040 | ±.018 | ±.70 | ±.0011 | ±.042 |
| $b_{oz}$ | .18 | 7.0 | .0089 | .35 | ±.014 | ±.56 | ±.00028 | ±.011 | ±.013 | ±.50 | ±.0012 | ±.048 |
| $x_l$ | .02 | .8 | .0010 | .04 | ±.0023 | ±.09 | ±.000 | ±.000 | ±.00076 | ±.03 | ±.00030 | ±.012 |

TABLE VI.- MIRROR POINTING ERRORS

| Elevation angle, $\theta$, deg | Errors, $\alpha - \alpha'$, $\beta - \beta'$, arc min, at azimuth angle, $\psi$, of – | | | | | | | | | | | | | |
|---|---|---|---|---|---|---|---|---|---|---|---|---|---|---|
| | $-160^{\circ}$ | $-120^{\circ}$ | $-80^{\circ}$ | $-40^{\circ}$ | $-30^{\circ}$ | $-20^{\circ}$ | $-10^{\circ}$ | $0^{\circ}$ | $10^{\circ}$ | $20^{\circ}$ | $30^{\circ}$ | $40^{\circ}$ | $60^{\circ}$ | $100^{\circ}$ |
| Sphere A | | | | | | | | | | | | | | |
| 40 | (a) | -4, 4 | 1, 5 | 12, 2 | 16, -2 | 9, -2 | 17, -4 | 8, -5 | 4, -6 | 2, -6 | 3, -9 | 1, -7 | -2, -6 | -3, -1 |
| 20 | -11, 14 | 10, 7 | -4, 6 | 2, 7 | 4, 4 | 5, 3 | 5, -2 | 3, -2 | 3, -2 | 3, -5 | 1, -4 | 2, -4 | -6, -8 | -6, -2 |
| 0 | -16, 6 | -10, 6 | -14, 5 | -5, 1 | -10, -1 | 1, 0 | 6, -3 | 0, -2 | 1, -3 | 3, -4 | (a) | (a) | -5, -6 | -4, -6 |
| -20 | -23, 6 | -20, 5 | -21, -1 | -5, 2 | -2, 31 | 2, -1 | (b) | -1, 0 | 0, -4 | (a) | (a) | (a) | -8, -9 | -6, -5 |
| Sphere B | | | | | | | | | | | | | | |
| 40 | (a) | 1, 10 | 8, 6 | 5, -2 | 7, -6 | 13, -8 | 15, -3 | 5, -4 | 3, -1 | 2, -2 | 2, -3 | 1, 0 | 1, 3 | -5, 9 |
| 20 | 1, 17 | 4, 14 | 8, 3 | 1, 9 | 7, 9 | 7, 11 | 9, 6 | 5, 7 | 6, 7 | 7, 8 | 5, 8 | 6, -10 | 12, 4 | -1, 10 |
| 0 | 5, 14 | 10, 13 | 3, 15 | -2, 6 | 1, 6 | 6, 6 | 11, 7 | 5, 5 | 5, 4 | 5, 4 | (a) | (a) | 2, 8 | 3, 7 |
| -20 | 7, 20 | 1, 0 | 1, 13 | -1, 2 | -2, 2 | 4, 4 | (b) | 1, 2 | 3, 5 | (a) | (a) | (a) | 3, 7 | 2, 14 |

[a]Transit view of target blocked by cockpit.

[b]Target occluded by cockpit.

TABLE VII.- MAXIMUM DYNAMIC ERRORS FOR PROJECTION SERVOS

| Maneuver | A, deg | Vertical error, $\Delta z$, deg | Lateral error, $\Delta y$, deg | Longitudinal error, $\Delta x$, deg |
|---|---|---|---|---|
| Sphere A | | | | |
| $\psi = A \sin \omega t$ | 170 | ±0.60 | ±1.25 | ±0.75 |
| $\psi = A \sin \omega t$ | 40 | ±.20 | ±.42 | ±.40 |
| $\theta = A \sin \omega t$ | 40 | ±.40 | ±.12 | ±.25 |
| $\phi = A \sin \omega t$ | 40 | ±.20 | ±.50 | ±.25 |
| $\phi = A \sin \omega t$ | 170 | ±1.20 | ±.75 | ±1.10 |
| Sphere B | | | | |
| $\psi = A \sin \omega t$ | 170 | ±0.95 | ±0.90 | ±0.45 |
| $\psi = A \sin \omega t$ | 40 | ±.25 | ±.25 | ±.11 |
| $\theta = A \sin \omega t$ | 40 | ±.60 | ±.20 | ±.40 |
| $\phi = A \sin \omega t$ | 40 | ±.20 | ±1.10 | ±.40 |
| $\phi = A \sin \omega t$ | 170 | ±.60 | ±1.50 | ±.90 |

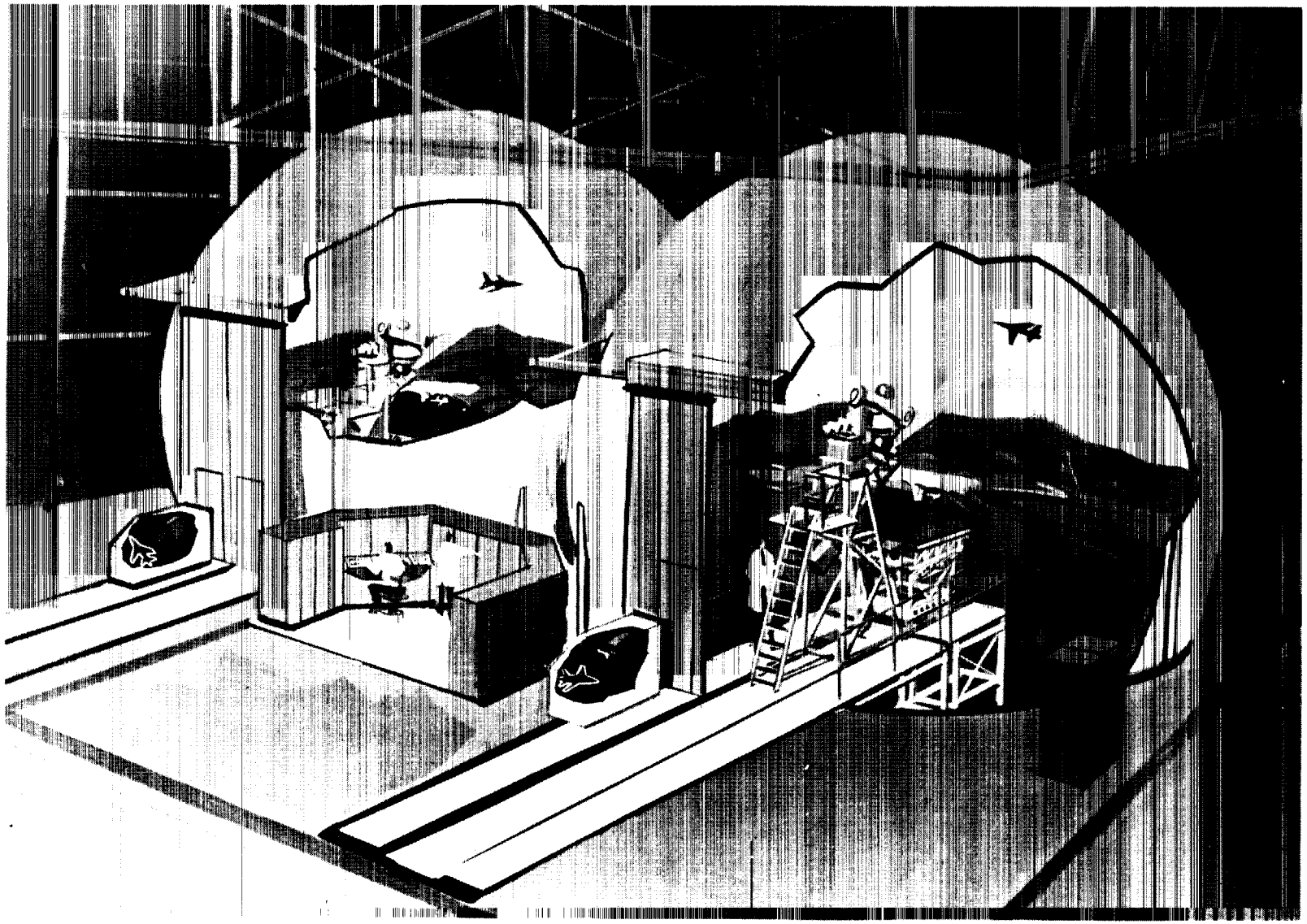

L-71-8700

Figure 1.- Langley differential maneuvering simulator.

L-72-1361

Figure 2.- DMS visual scene.

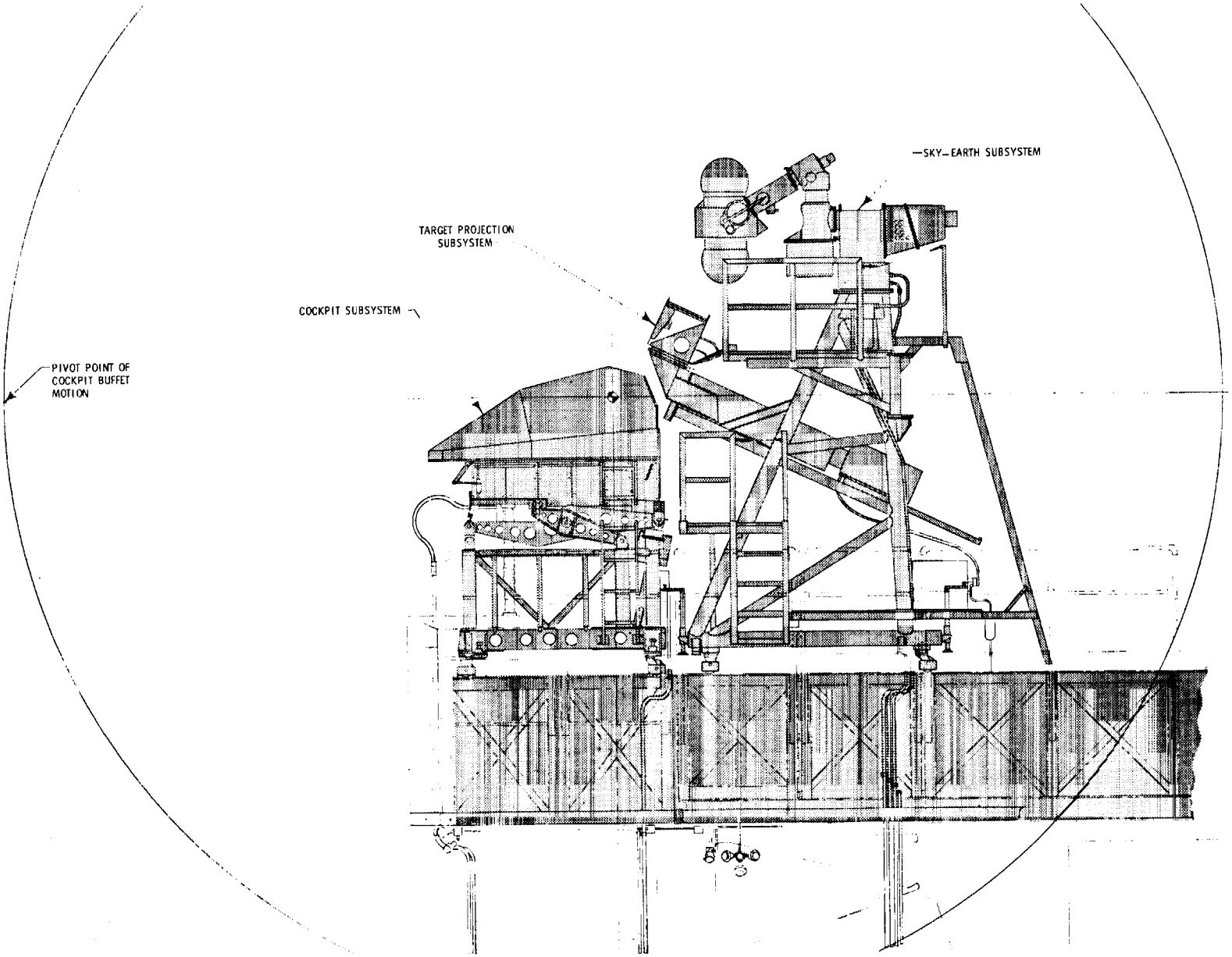


Figure 3.- Cockpit and projection hardware.

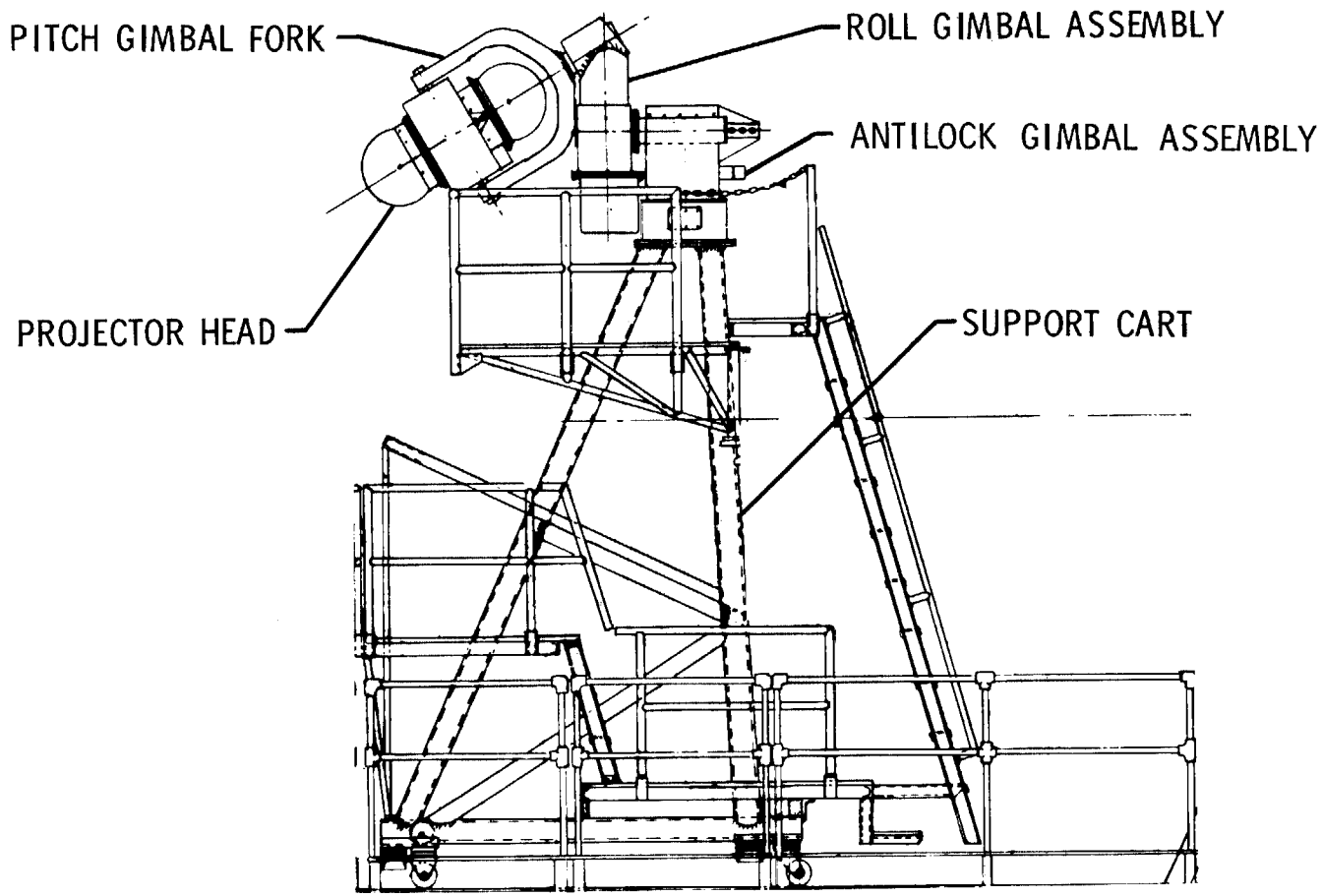


Figure 4.- Sky-Earth projection subsystem.

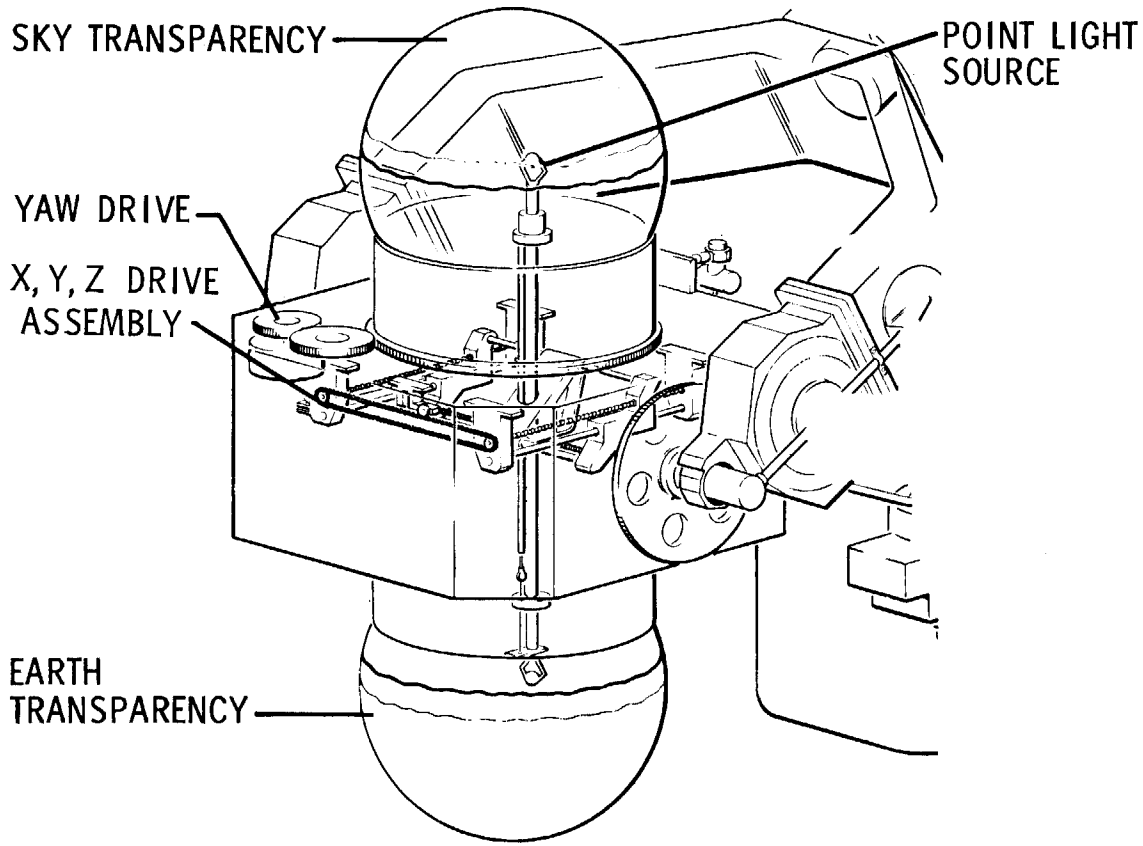


Figure 5.- Sky-Earth projector head.

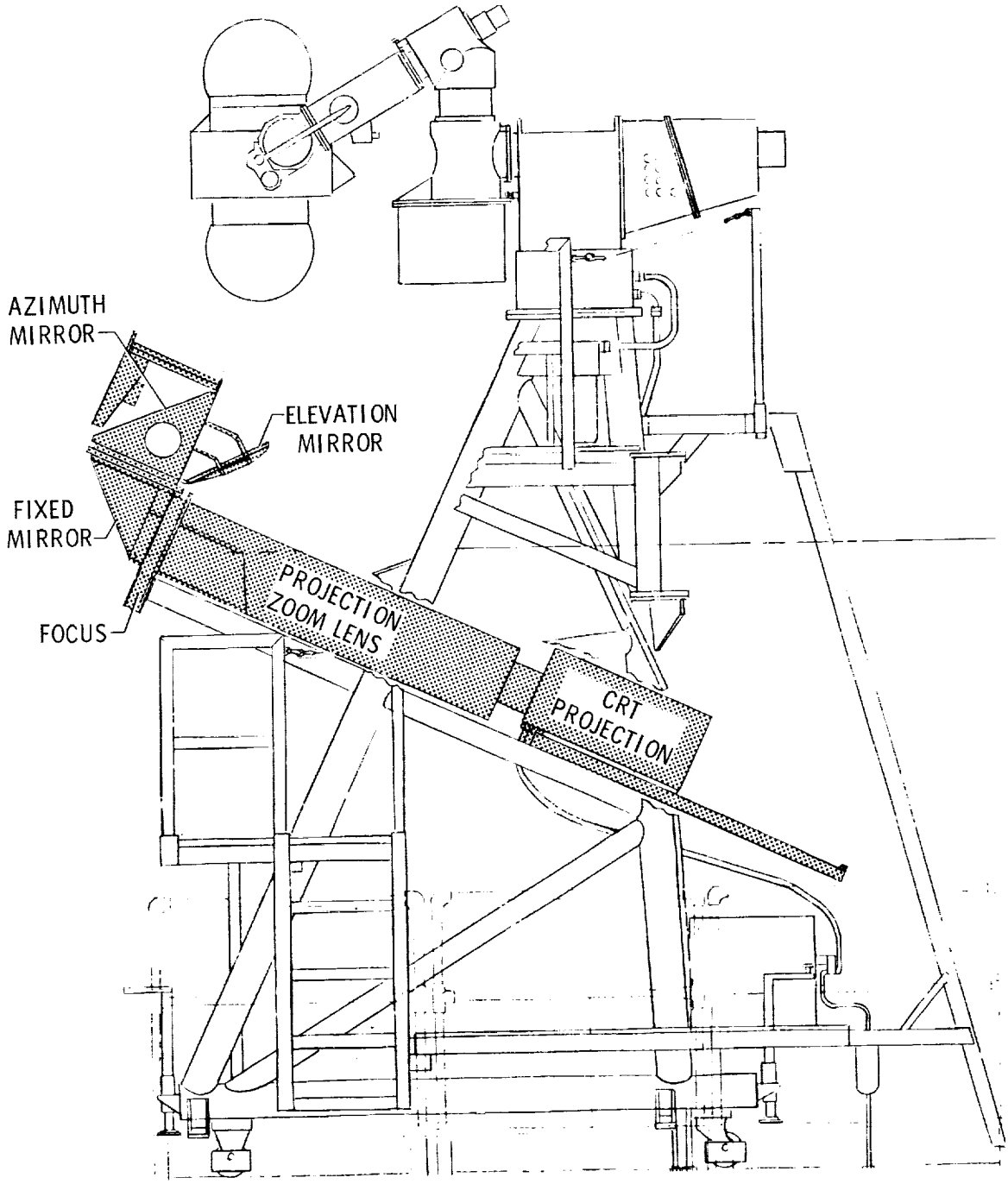


Figure 6.- Target-image projection subsystem.

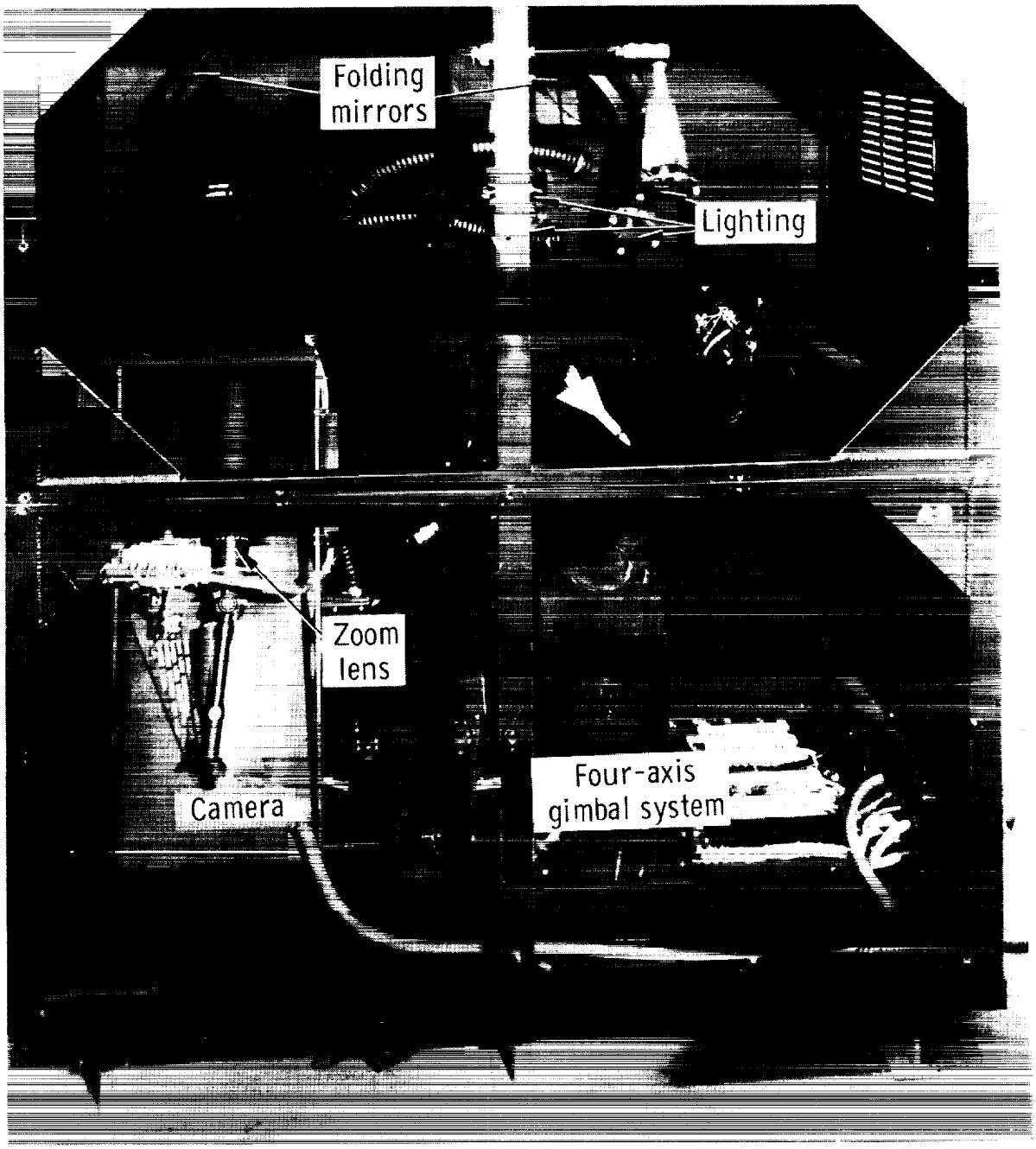


L-71-3054.1

Figure 7.- Target-image generation subsystem.

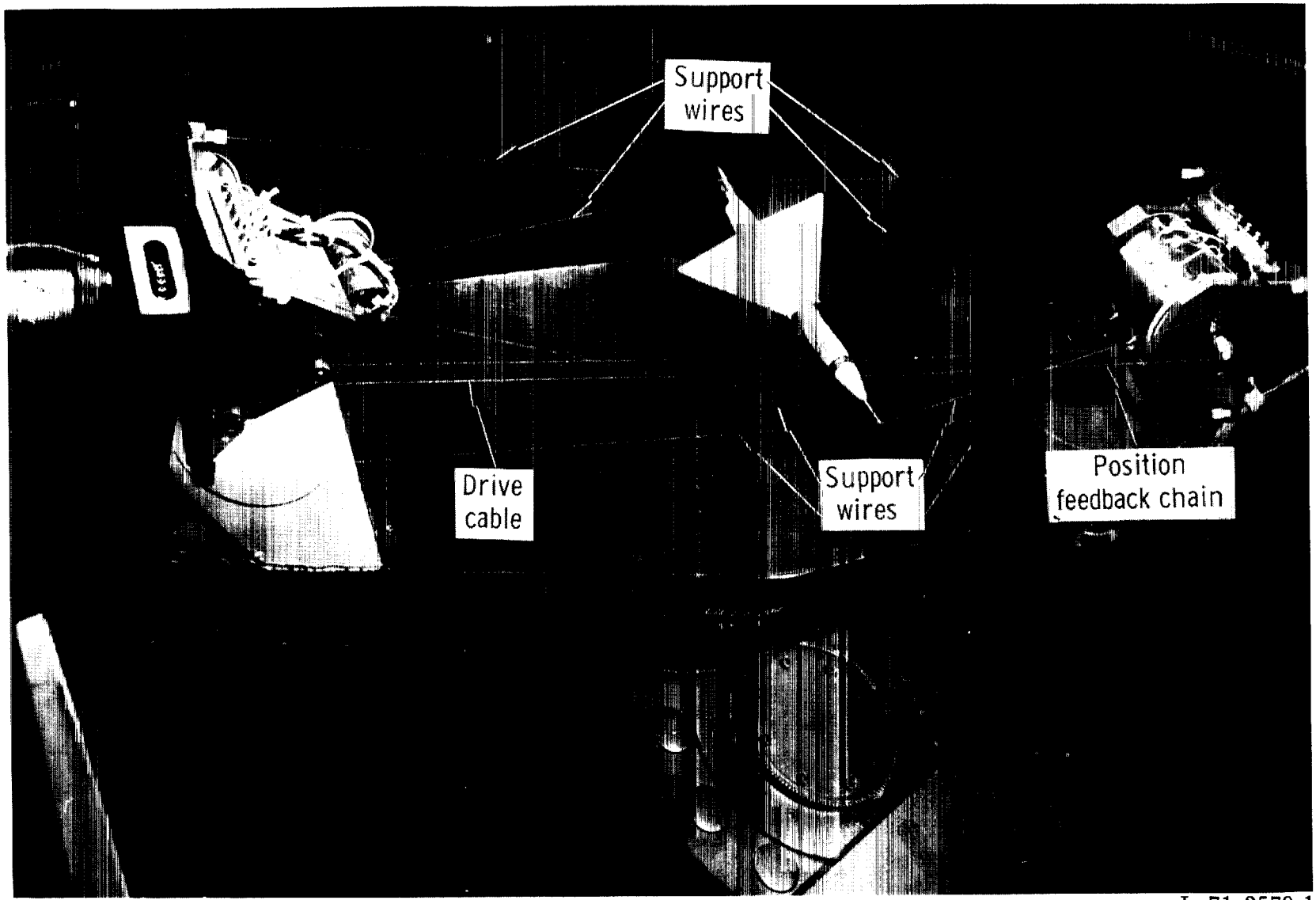


L-71-2579.1

Figure 8.- Target model.

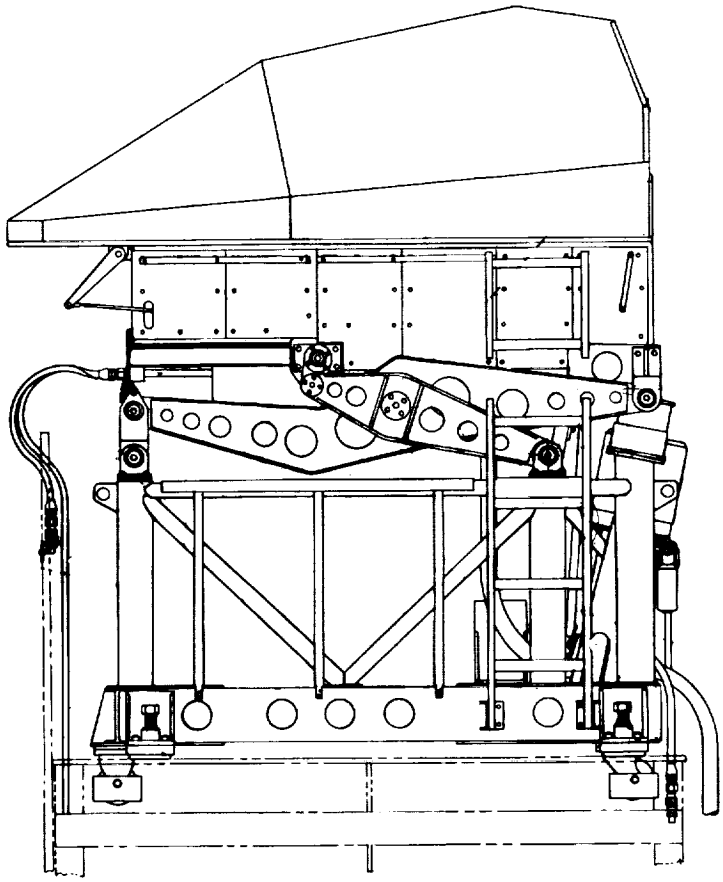

Figure 9.- Cockpit subsystem.

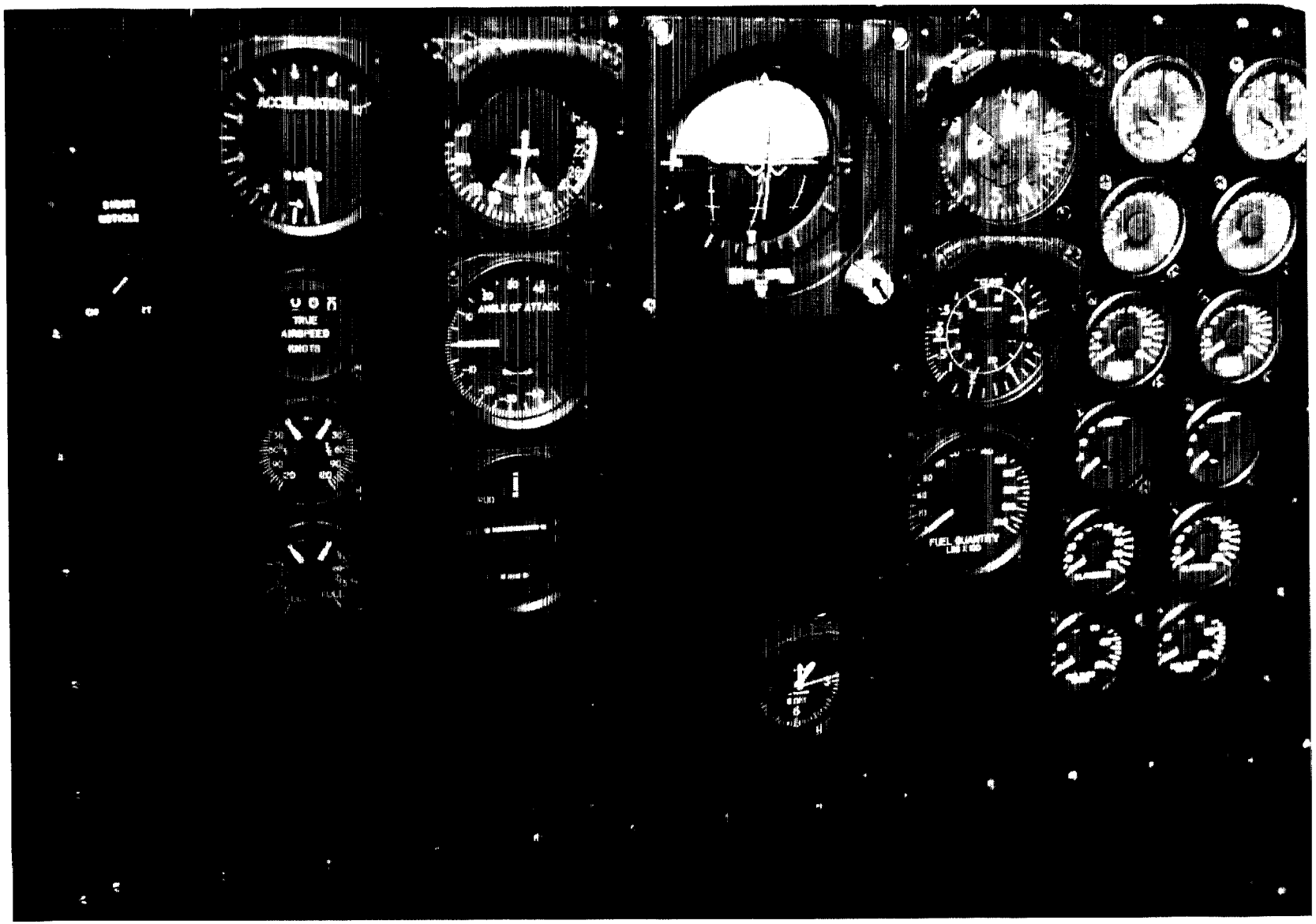


L-71-2573

Figure 10.- Cockpit instrument panel.

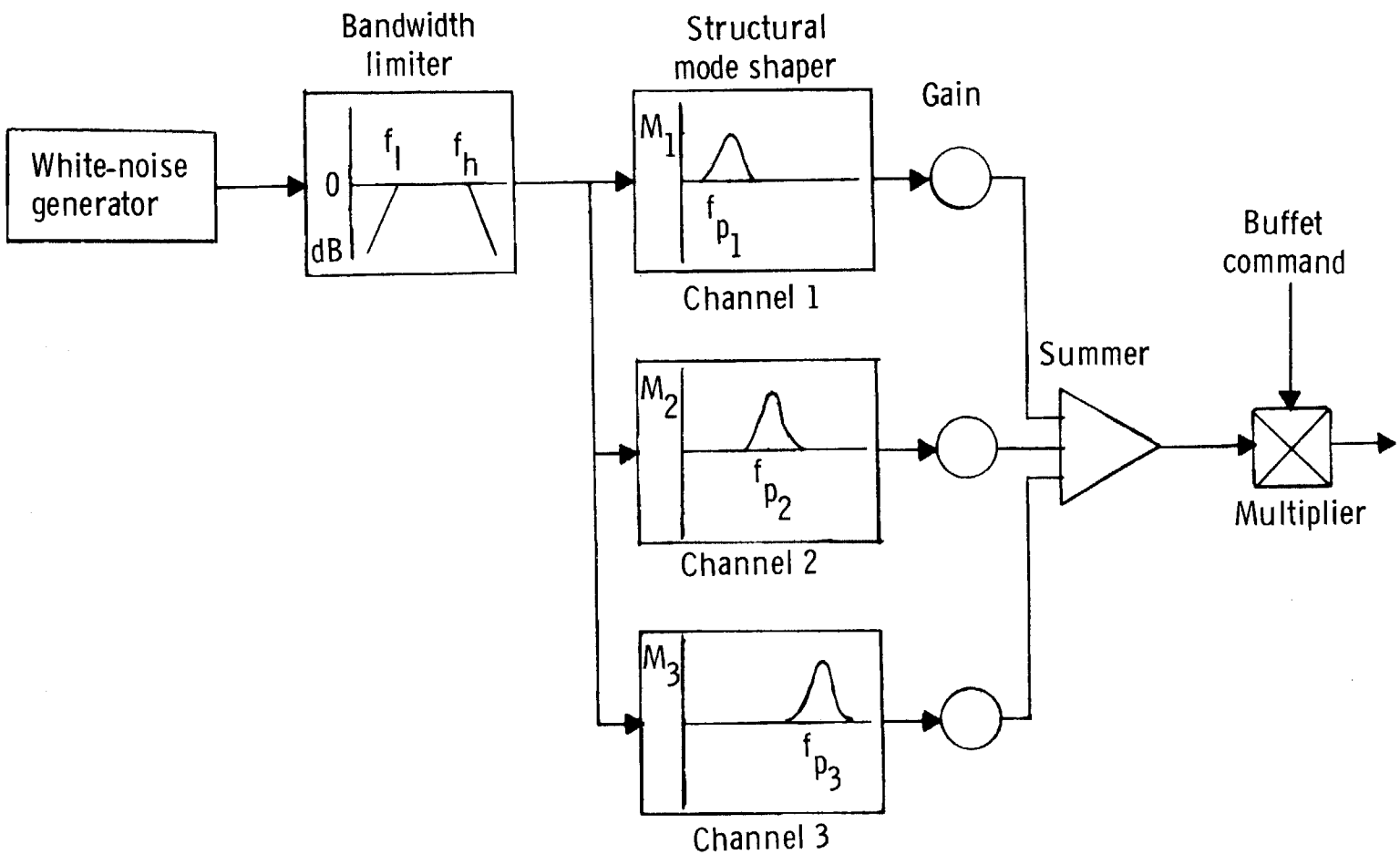


Figure 11.- Buffet-signal generation.

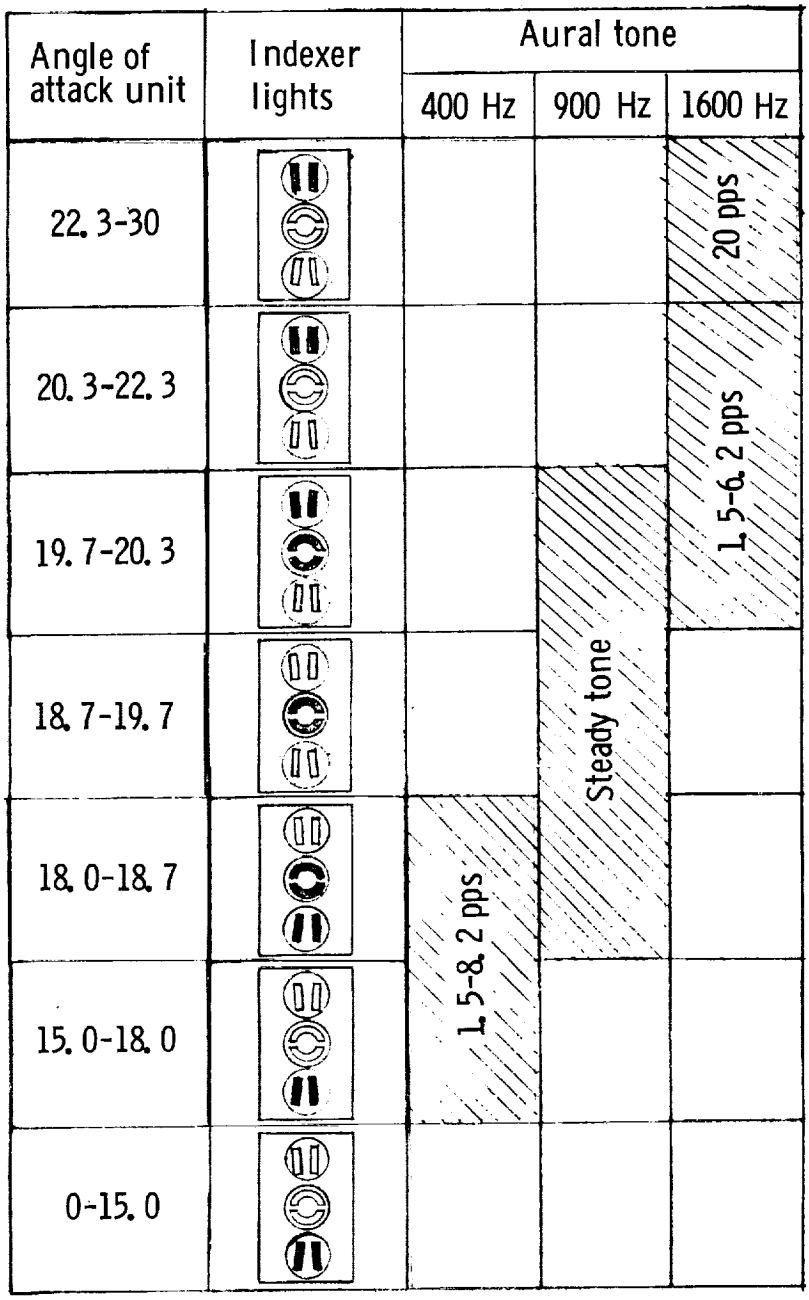


Figure 12.- Angle-of-attack indicators.

L-71-3049.1

Figure 13.- DMS control console.

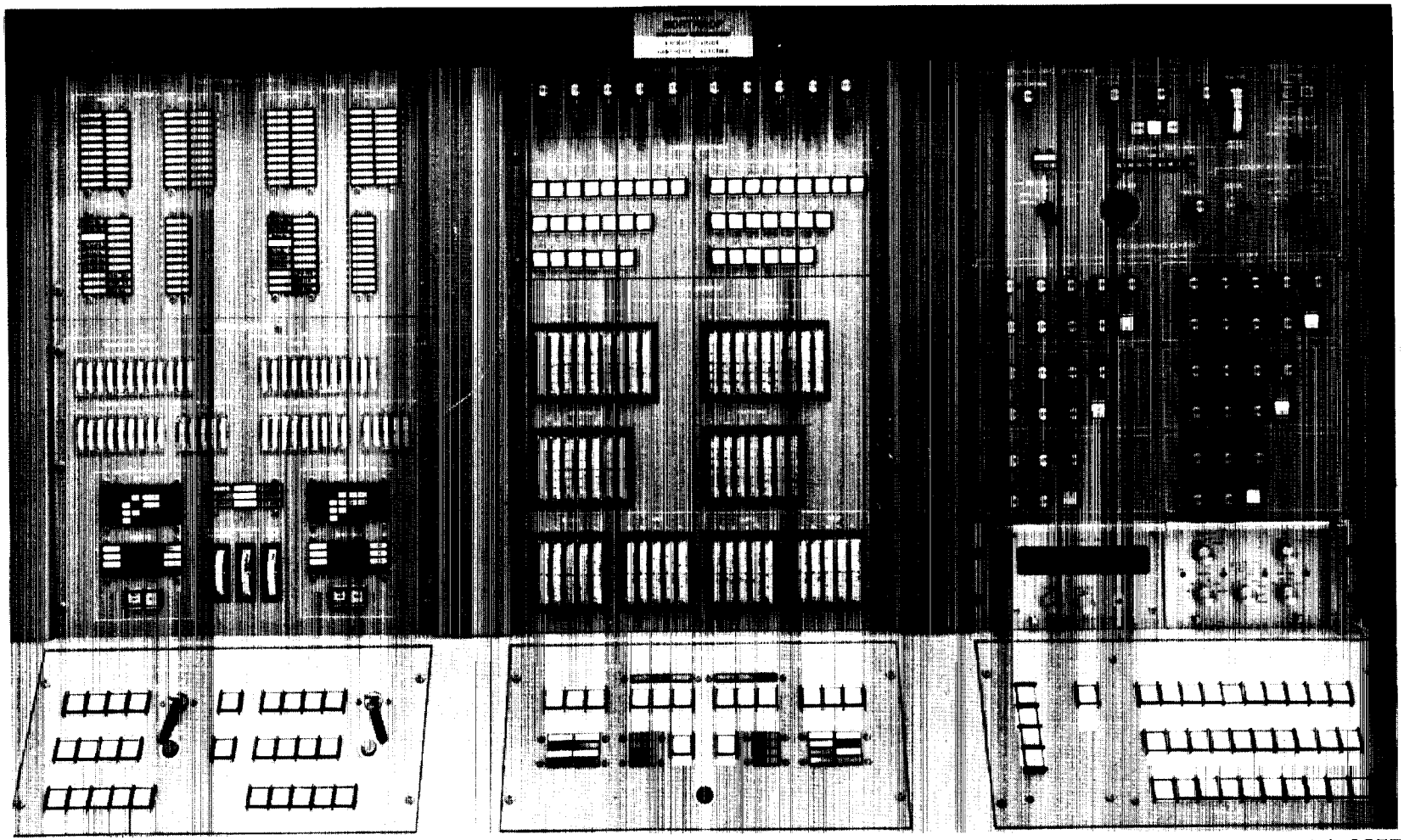

L-71-2577

Figure 14.- Control console section II.

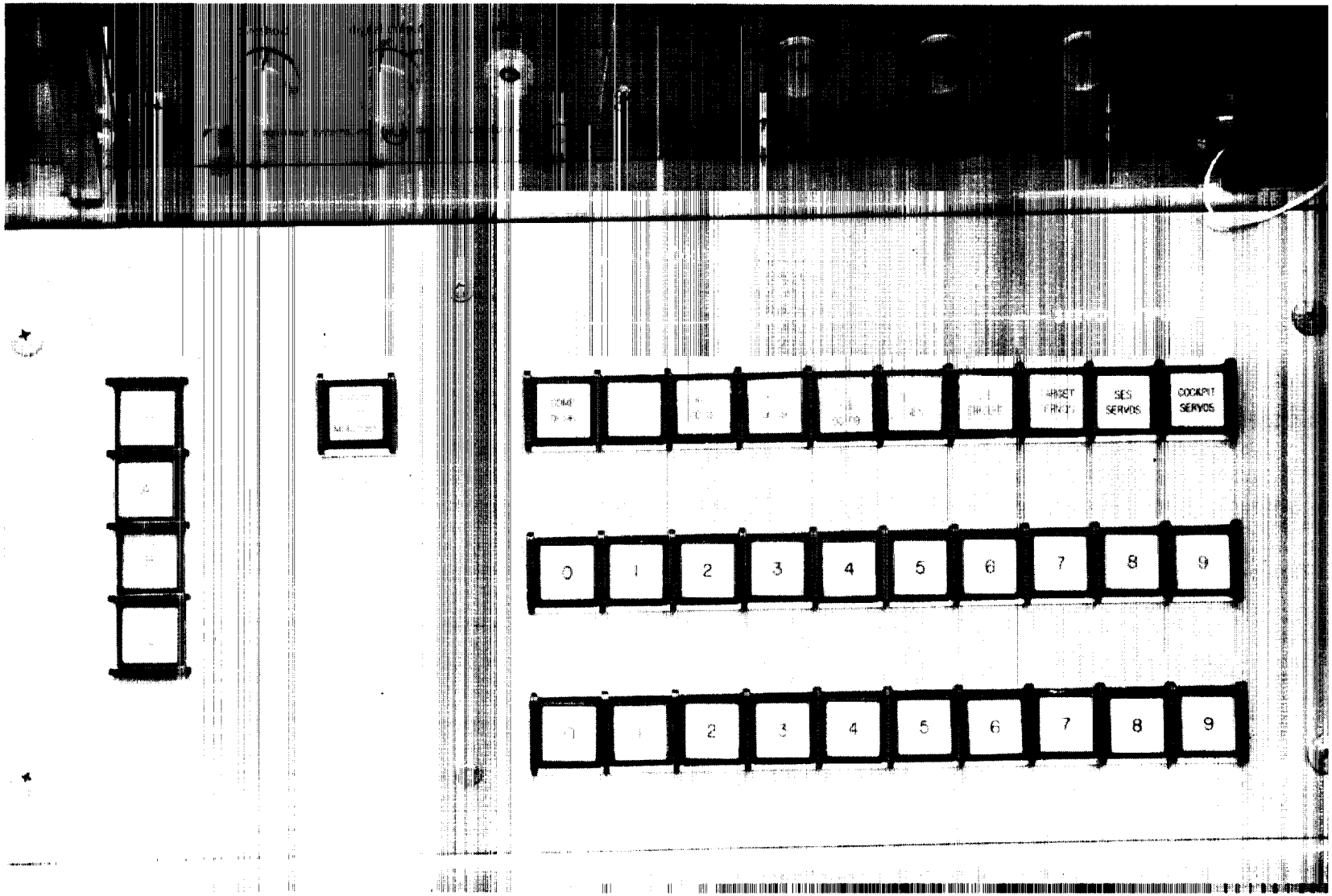


L-72-6219

Figure 15.- Voltage monitoring control panel.

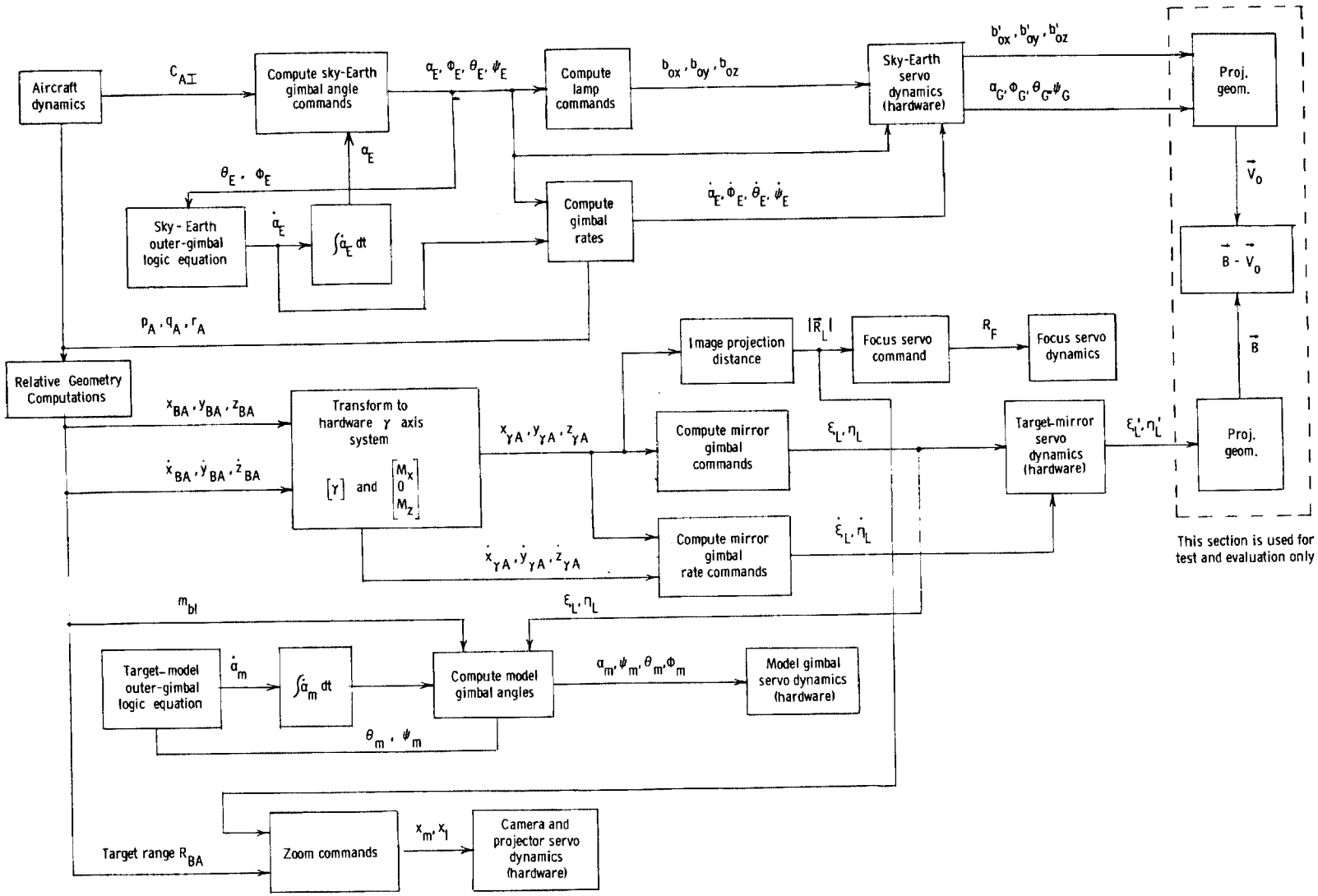


Figure 16.- Block diagram for interface computations used for each sphere.

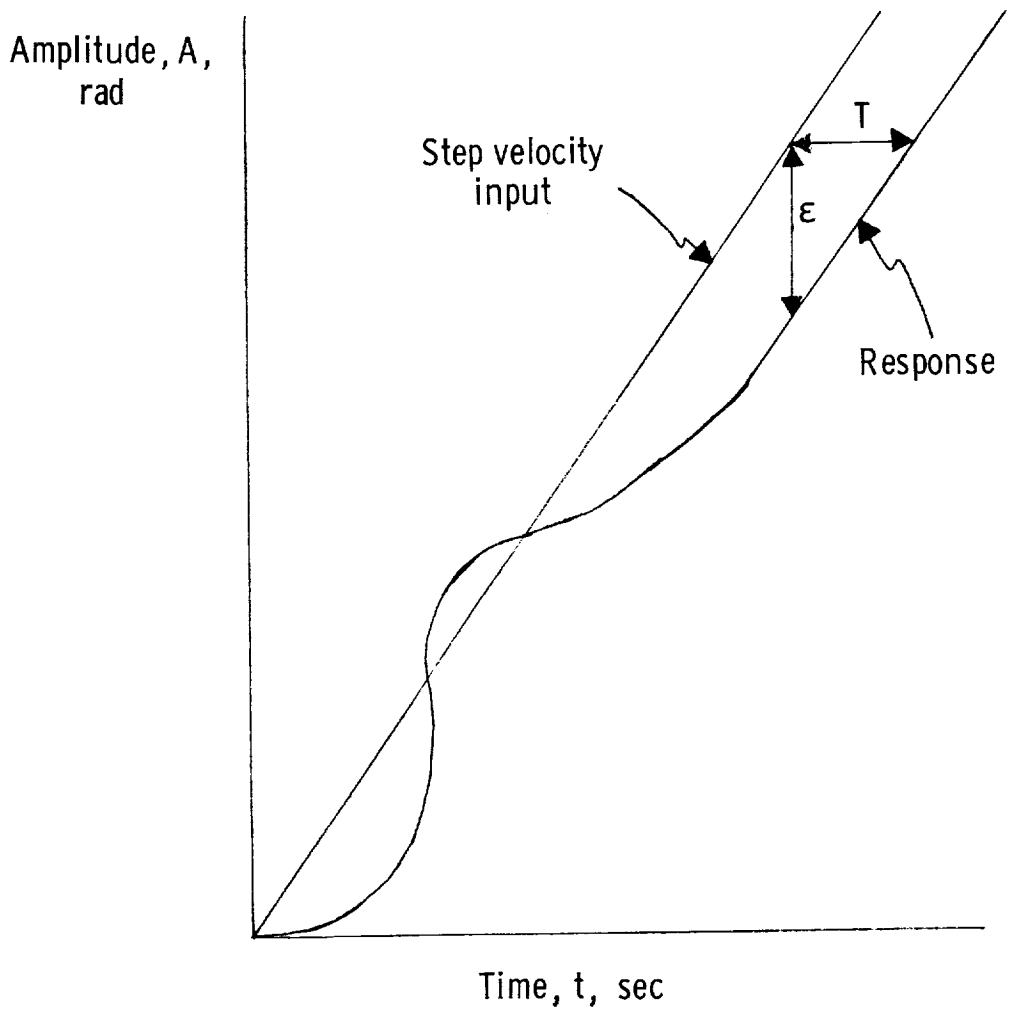


Figure 17.- Response of 0.707 damped, 25 rad/sec, second-order system.

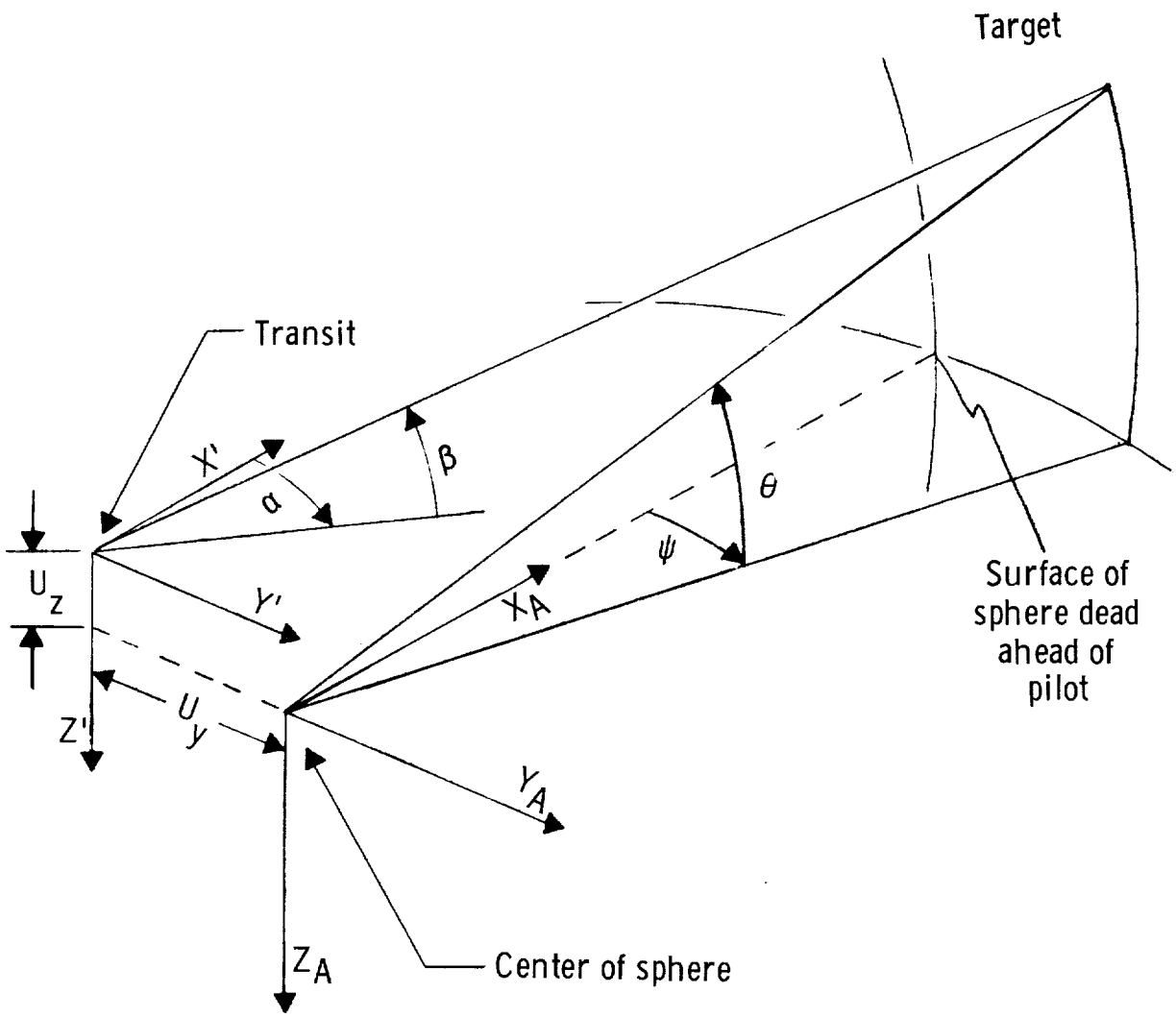


Figure 18.- Transit geometry for measurement of mirror pointing errors.

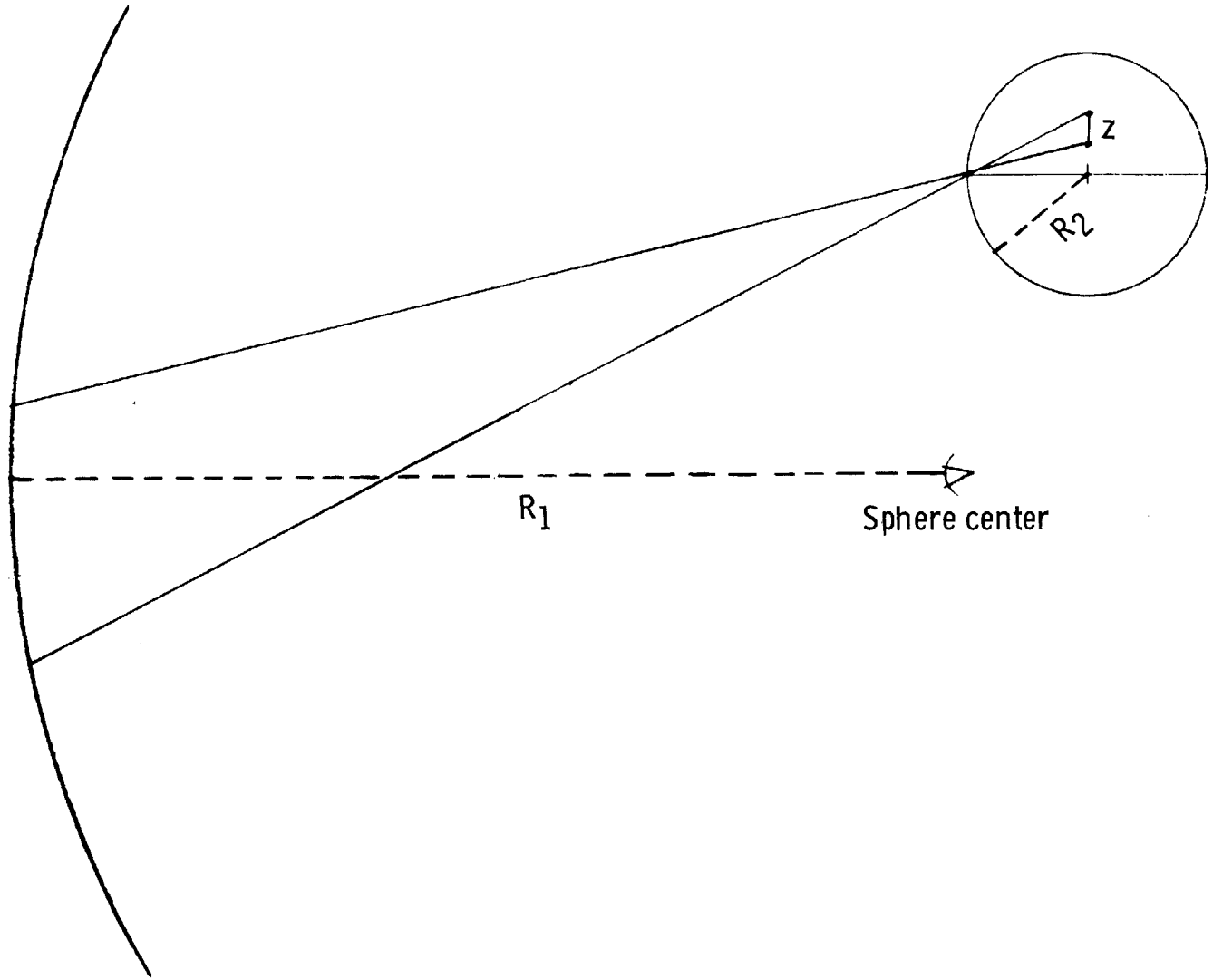


Figure 19.- Error in sky-Earth scene due to error in lamp position within the transparency.

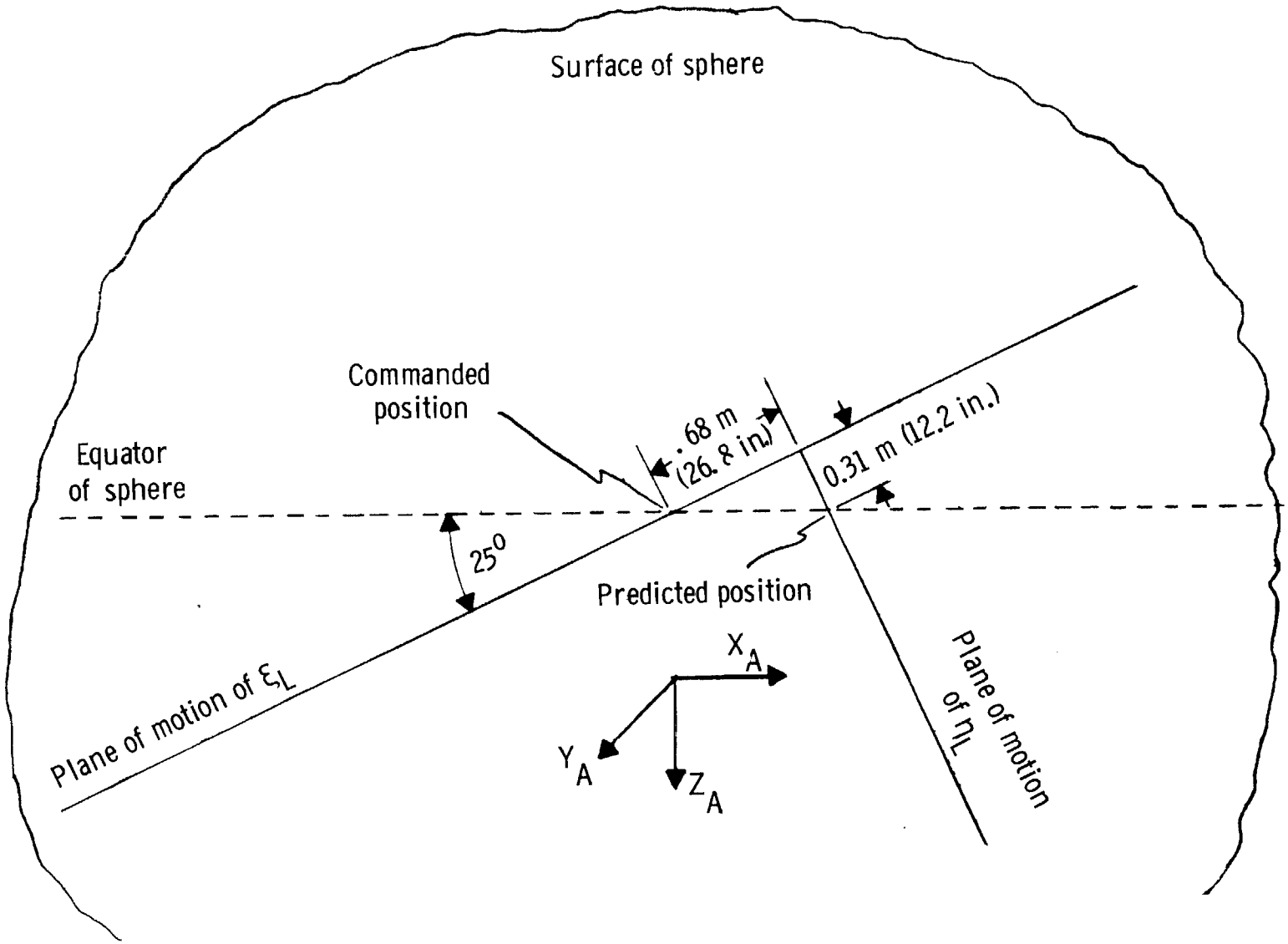


Figure 20.- Image projection for the case of matched servos (identical time lags).

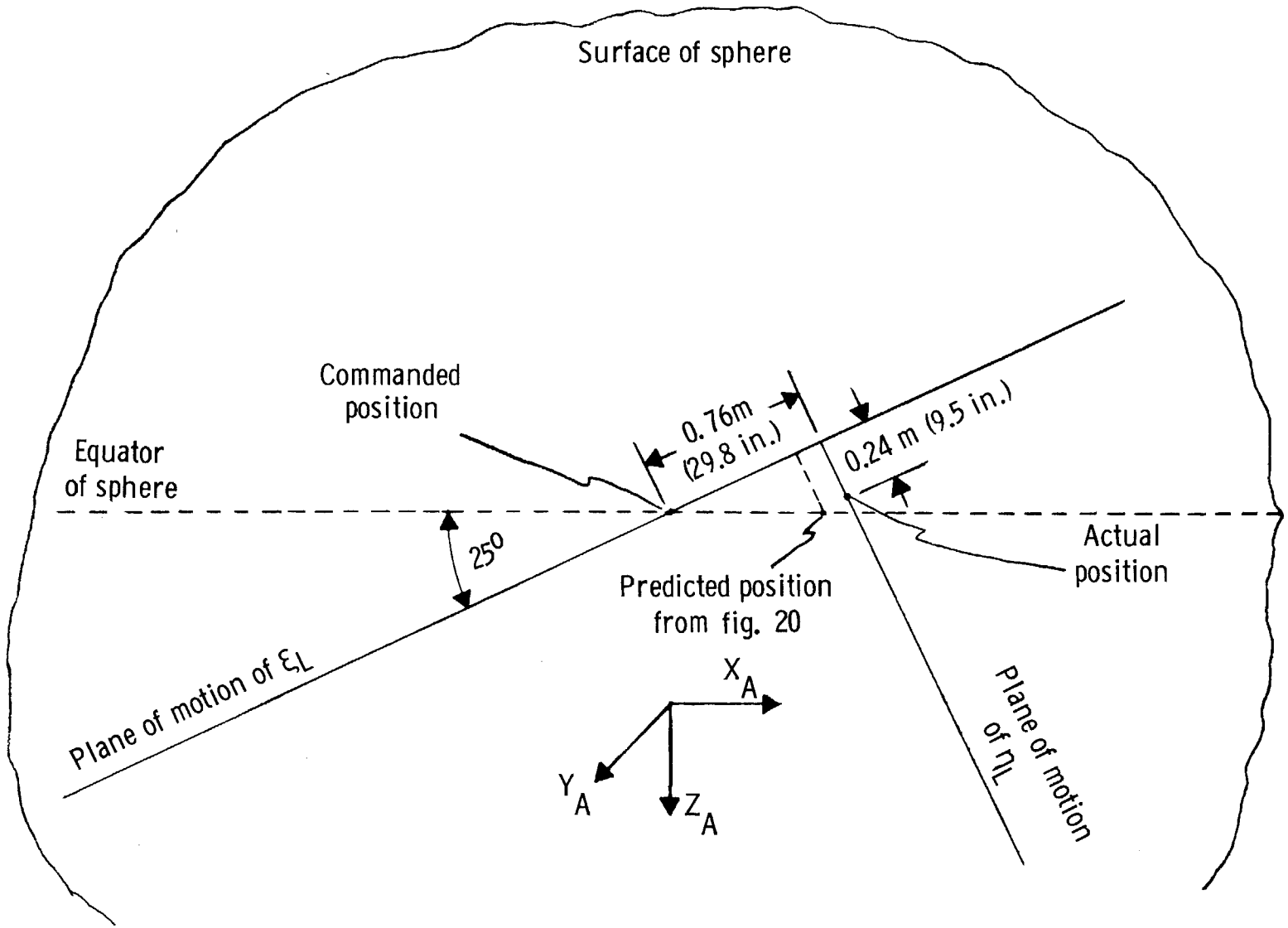


Figure 21.- Dynamic errors in image projection due to mismatched servo response.

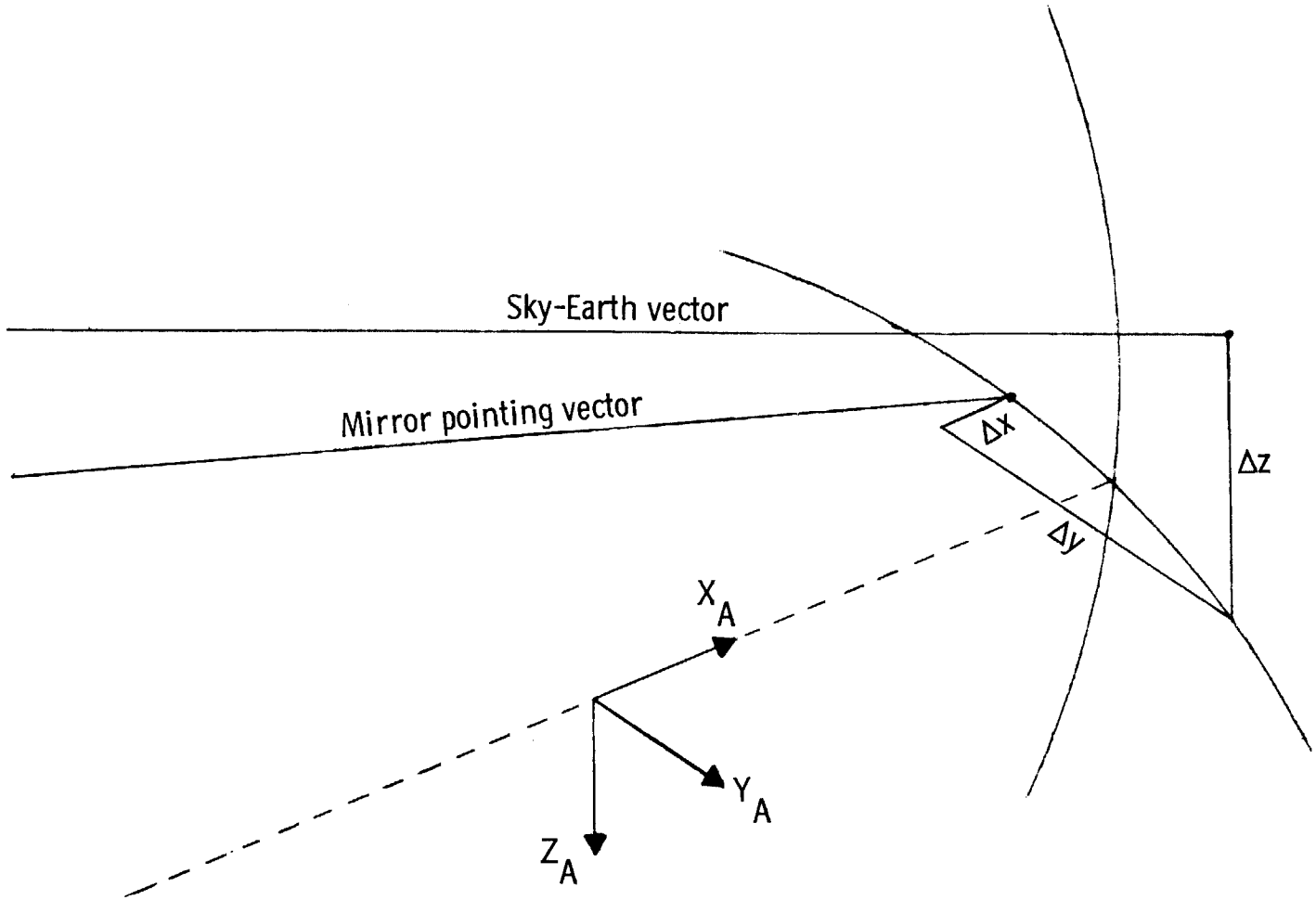


Figure 22.- Components of error between sky-Earth and target pointing vectors.

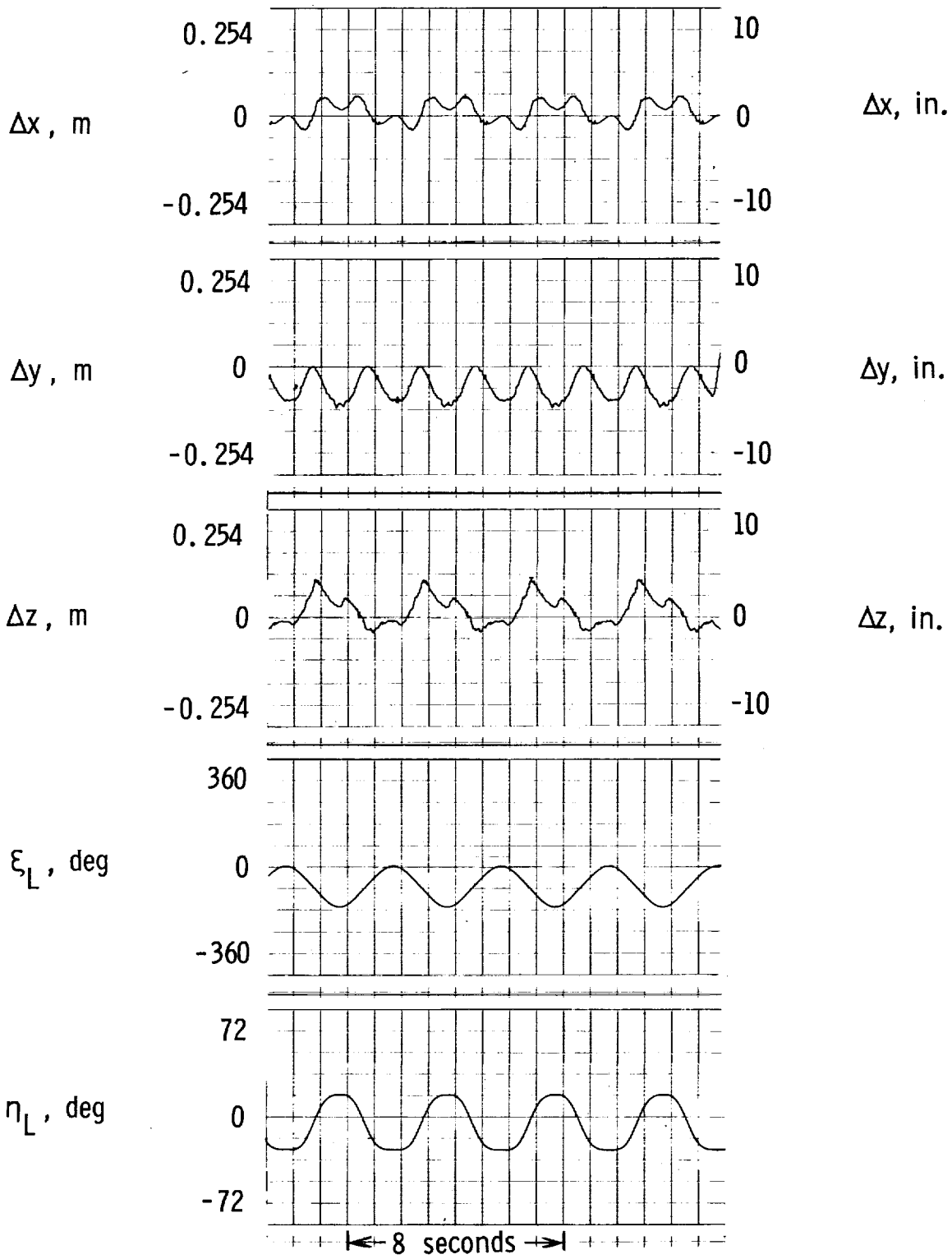


Figure 23.- Dynamic synchronization errors for pure-yaw maneuver.

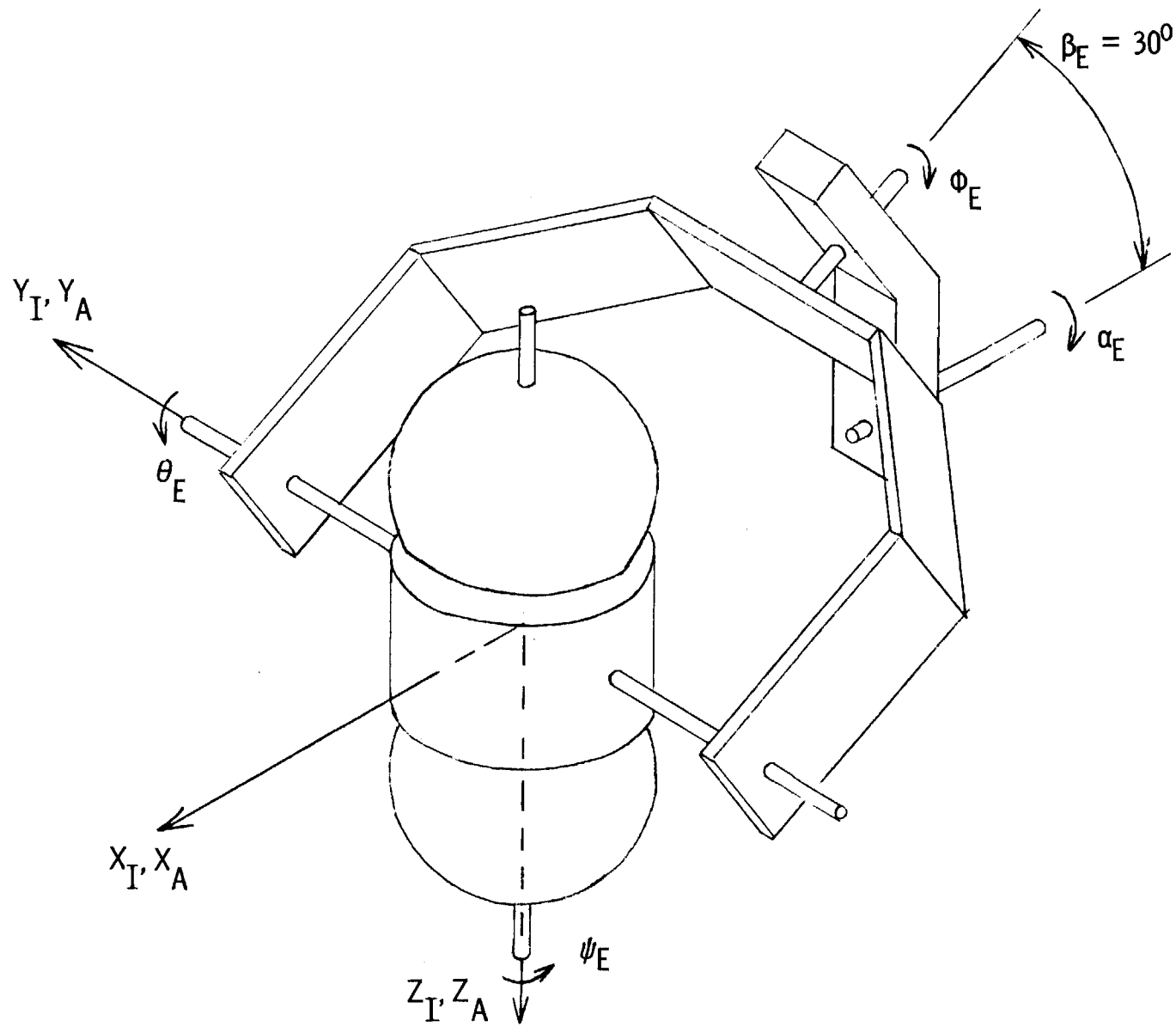


Figure 24.- Four-axis gimbal system with $\alpha_E = 0$ and aircraft in level flight.

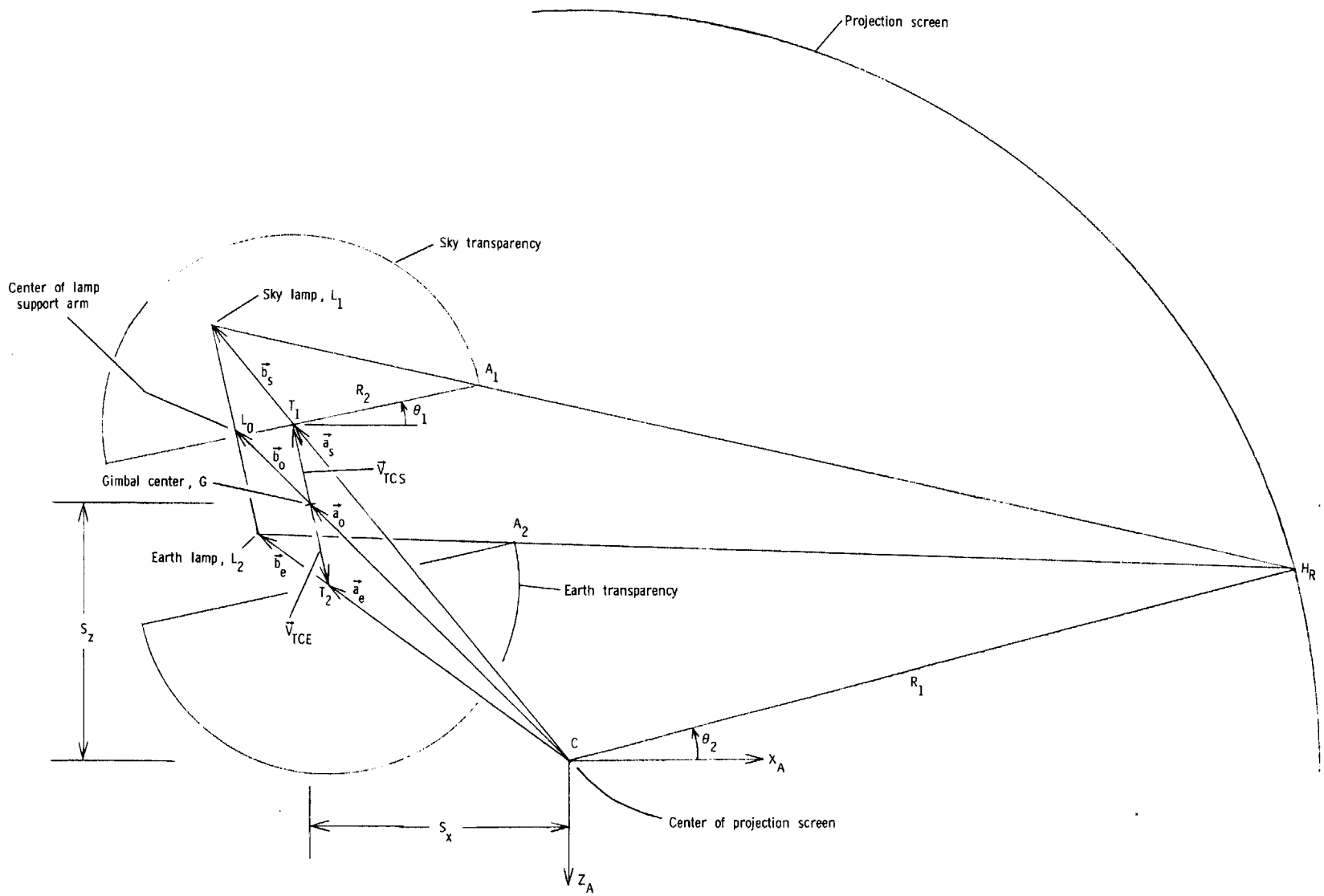


Figure 25.- Geometrical requirements for correct mapping of sky-Earth scene.

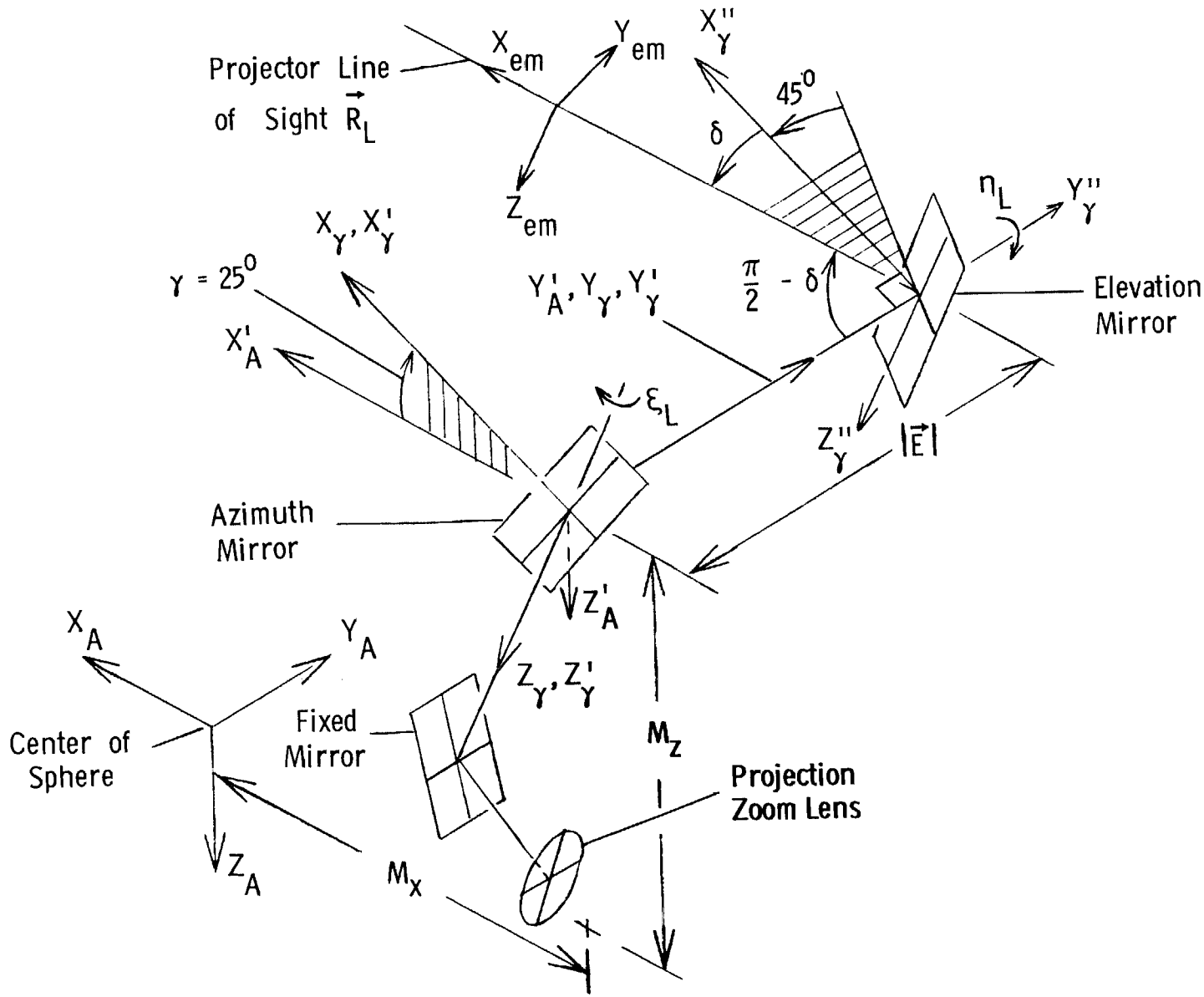


Figure 26.- Configuration of target-projection mirrors for condition of $\xi_L = \eta_L = 0$.

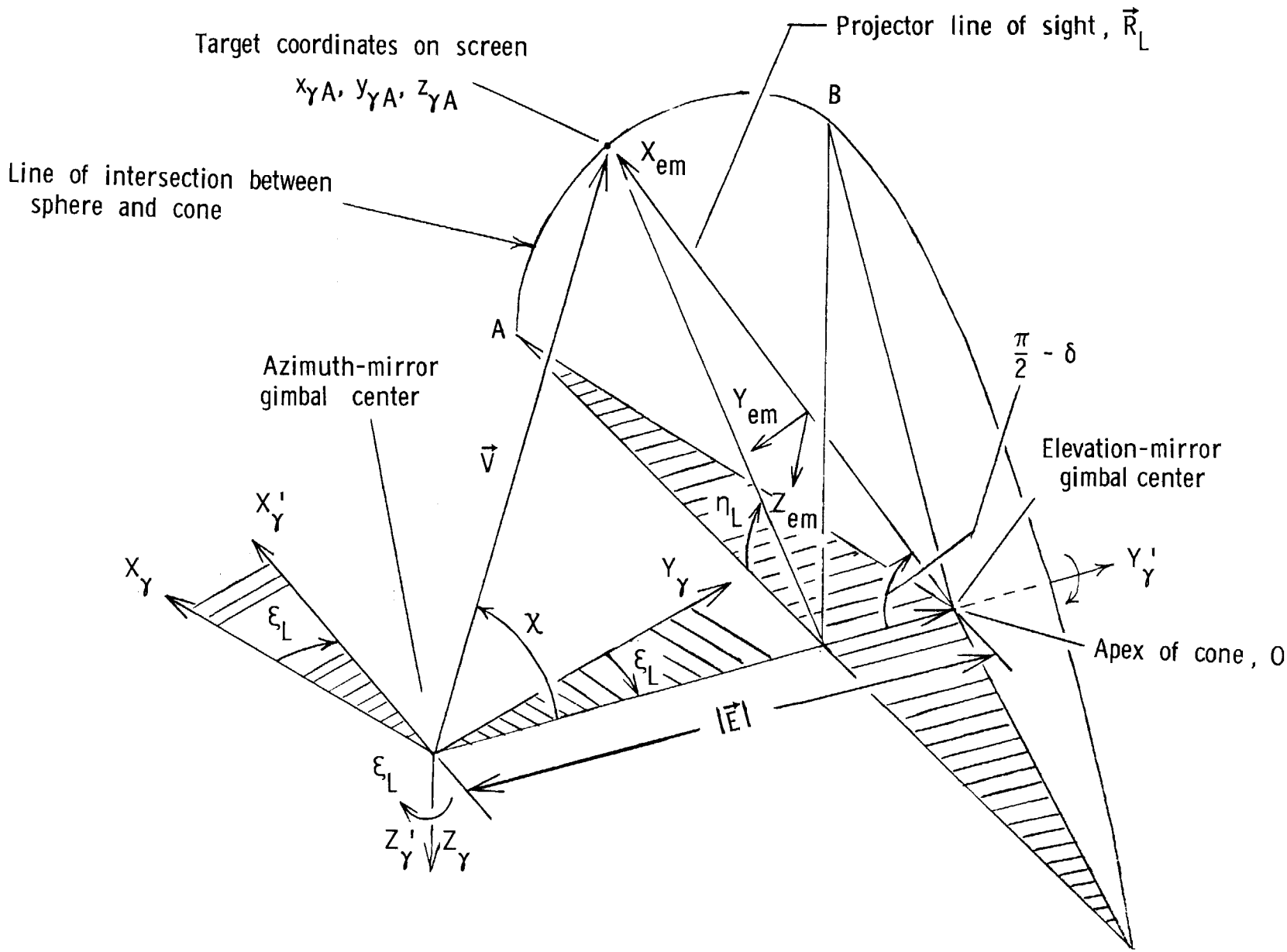


Figure 27.- Geometry for mirror drive equations.

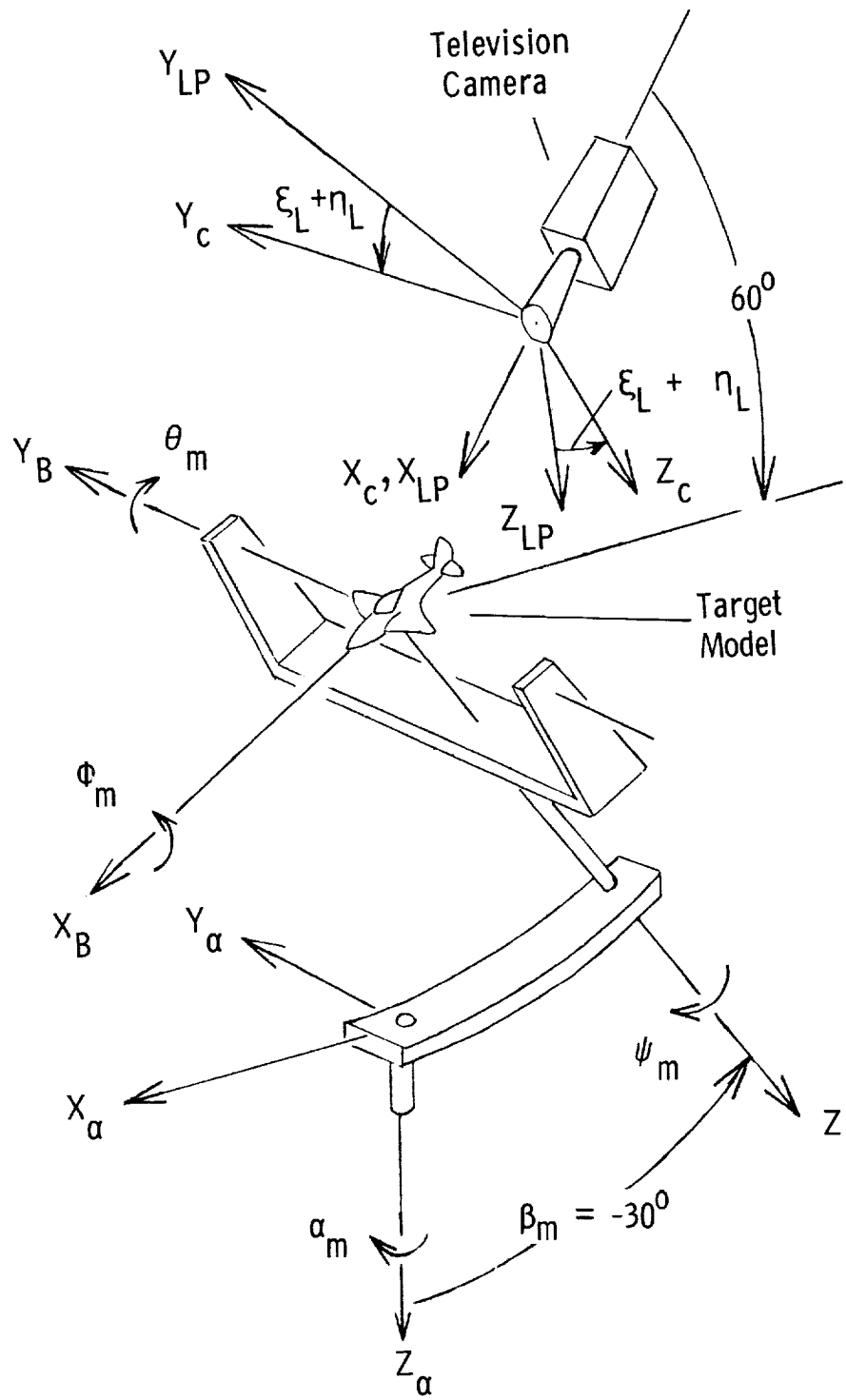


Figure 28.- Relative geometry between target model and camera.

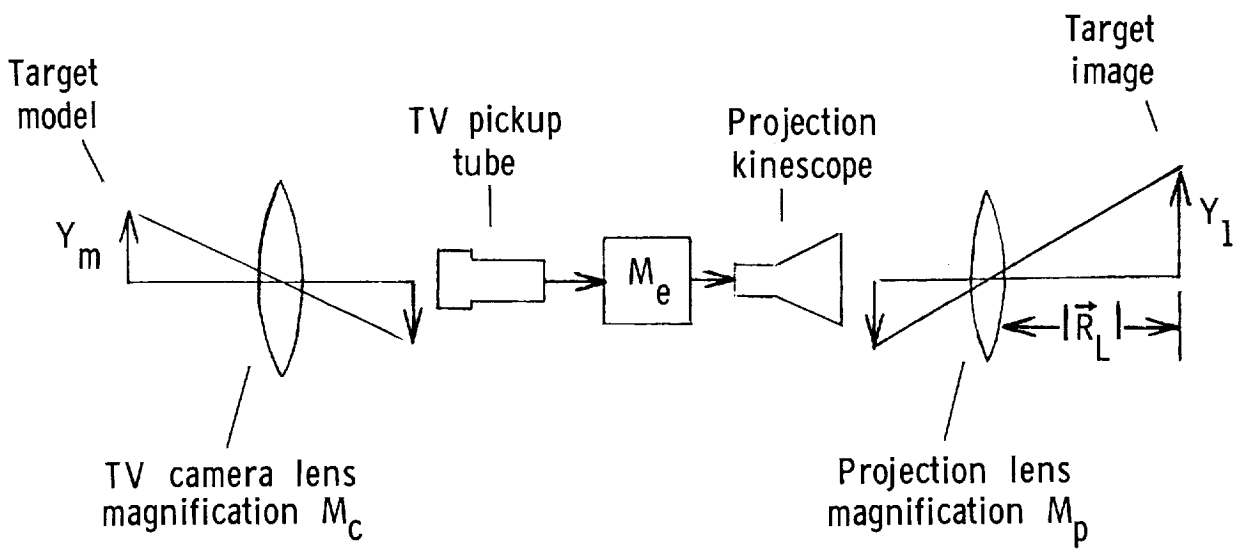


Figure 29.- System magnification relationships.

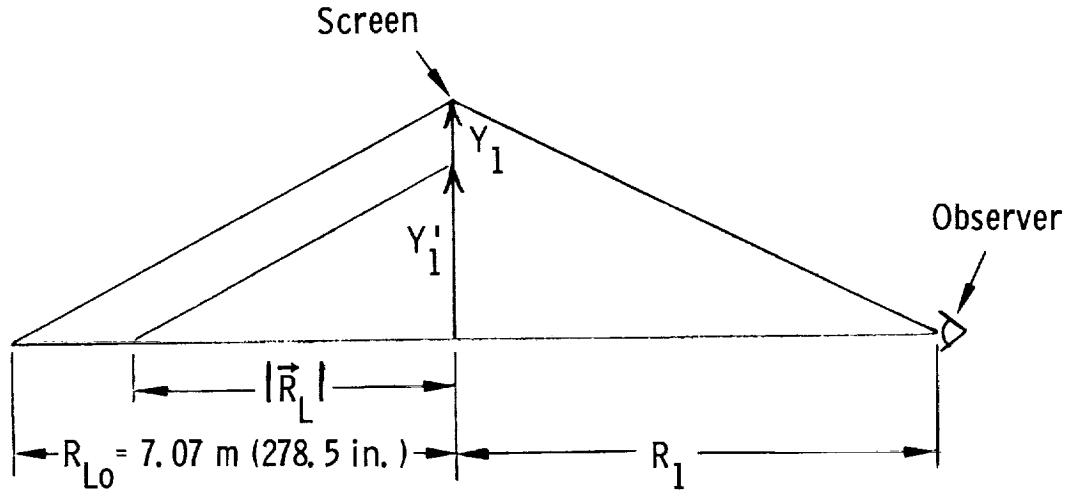


Figure 30.- Geometrical relationship between image size and image-projection distance.

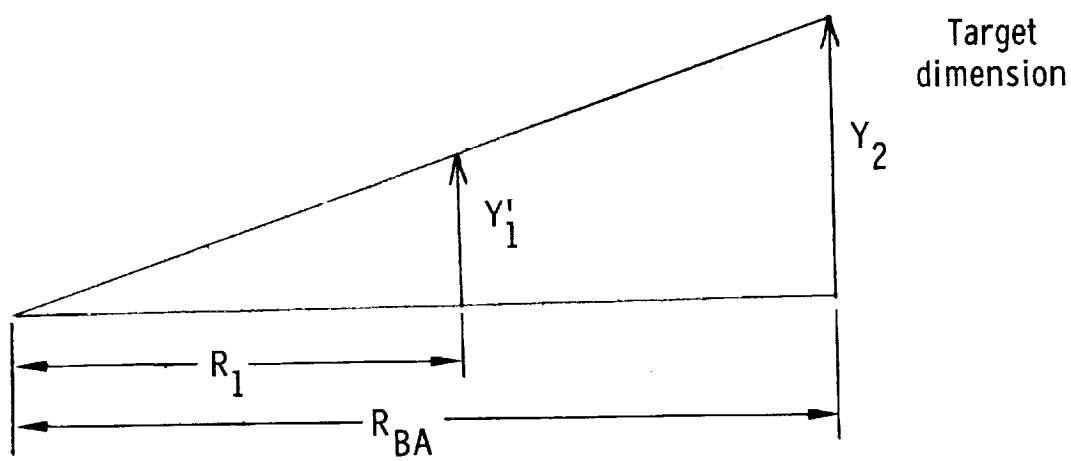


Figure 31.- Dimensional relationships between real world and simulator.

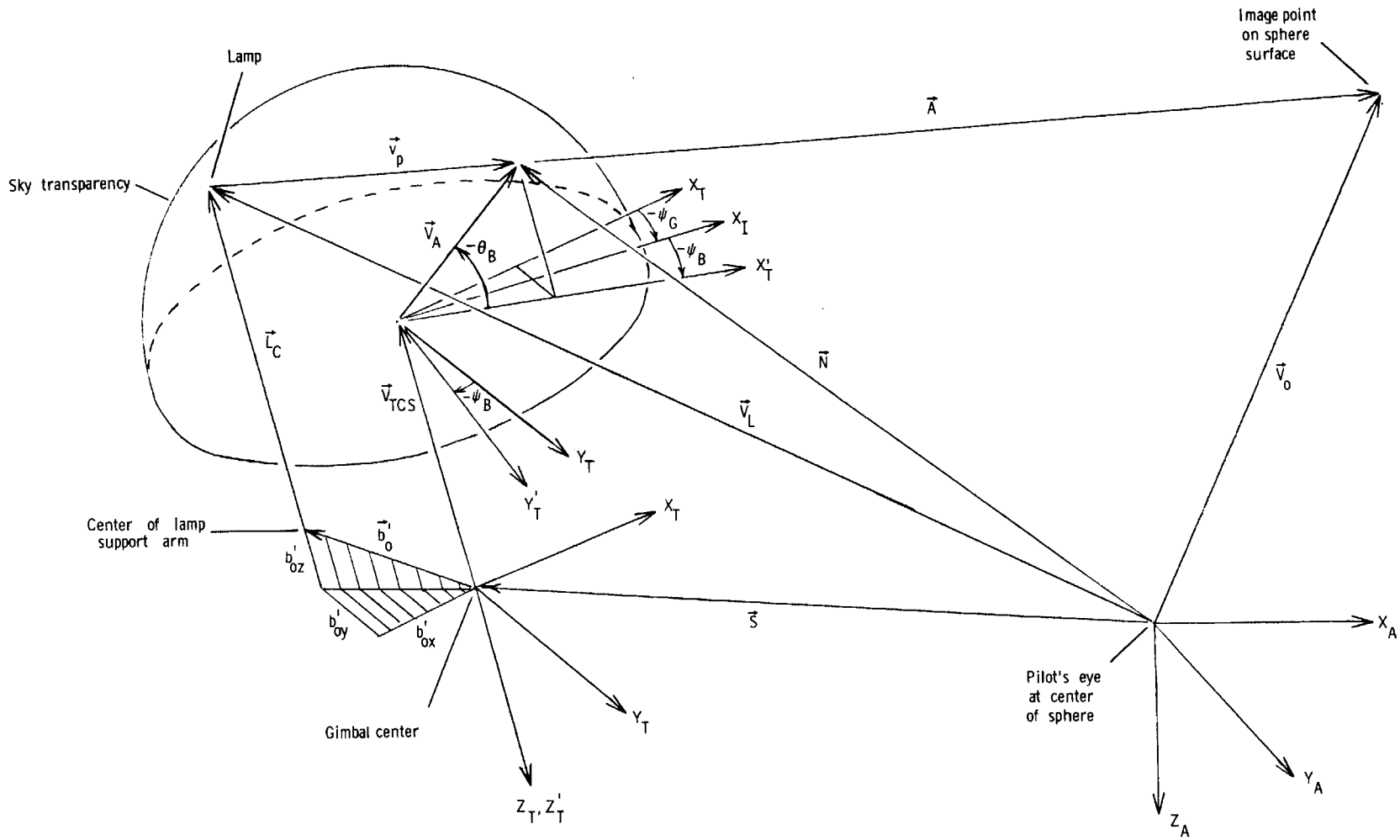


Figure 32.- Sky-projection geometry.

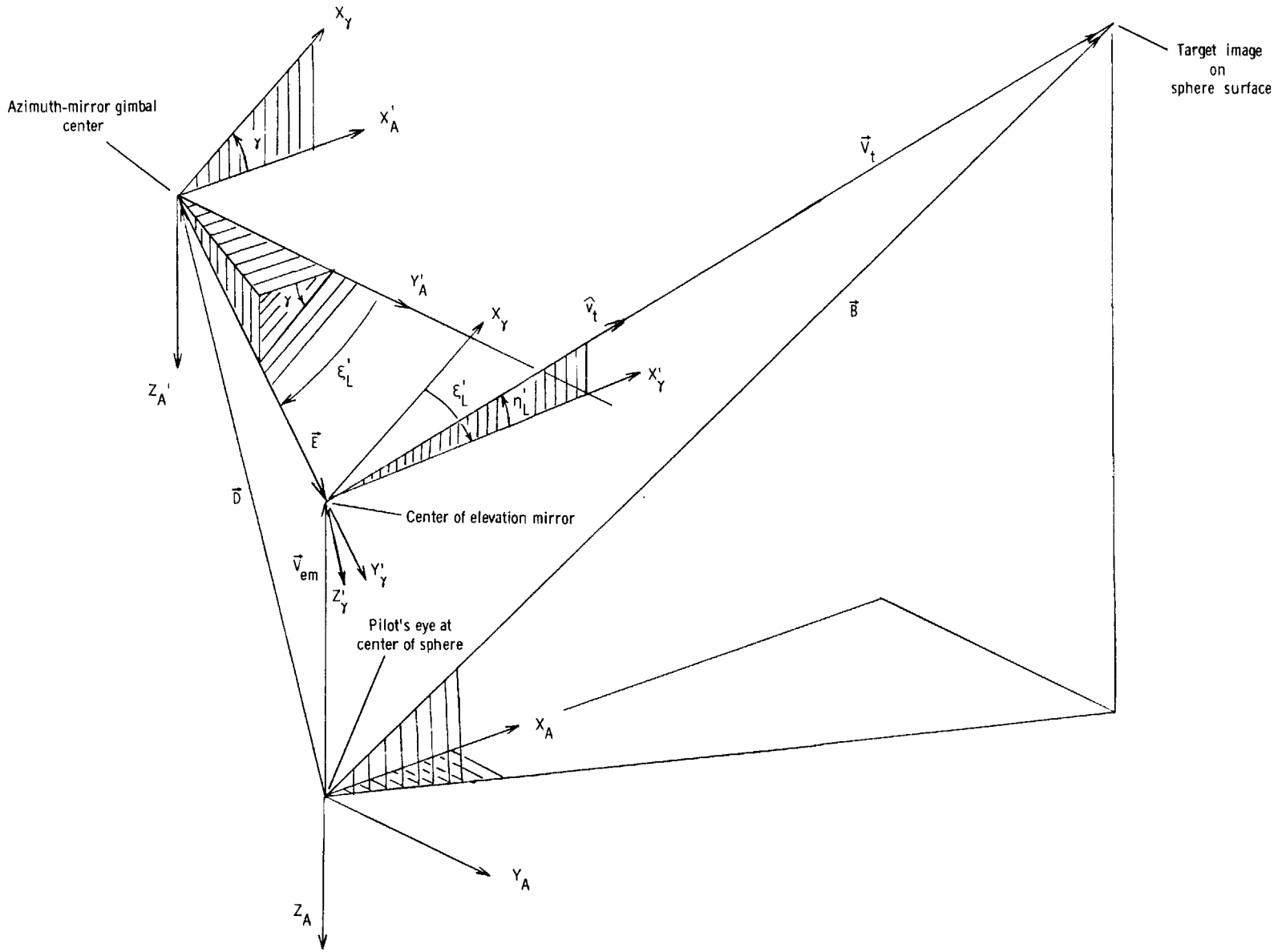


Figure 33.- Target-projection geometry.